Electrochemical Investigations of the Interactive Behavior of Nicotinamide Adenine Dinucleotide (NAD^+/NADH) with Electrode Surfaces: Towards Direct Electrochemical Regeneration of Enzymatically-active NADH

by

Irshad Ali

Department of Chemical Engineering
McGill University, Montreal, Canada
December 2012

A Thesis submitted to McGill University in partial fulfillment of the requirements of the degree of

Doctor of Philosophy

ABSTRACT

Nicotinamide adenine dinucleotide NAD(H) is a co-enzyme which participates in a large number of biochemical processes in which it acts as a hydrogen and electron carrier. Hence, NAD(H) is found in two redox forms: oxidized, NAD^+, and reduced, 1,4-NADH. Despite its high potential industrial use, due to its very high cost (especially that of 1,4-NADH) and the need to be added in a biochemical reactor in stoichiometric quantities, its current use is very limited. Hence, there is a need to develop *in-situ* 1,4-NADH regeneration methods. Electrochemical methods are of particular interest because of their potentially low cost and easy product isolation. However, the major problem in the electrochemical regeneration of enzymatically-active 1,4-NADH is the formation of an enzymatically-inactive dimer, NAD_2.

This PhD project focused on (i) the investigation of fundamental aspects of the interaction of NAD^+ with a glassy carbon (GC) electrode surface, in terms of the NAD^+ reduction kinetics and its adsorption, and on (ii) the development of electrodes for the *direct* (non-mediated) electrocatalytic regeneration of enzymatically-active 1,4-NADH.

Potentiodynamic polarization measurements showed that under the experimental conditions employed, the NAD^+ reduction reaction is under diffusion control, is irreversible (requires overpotential of more than -550 mV), and is of pseudo-first order with respect to NAD^+. The kinetics of reduction of NAD^+ on GC at a *formal* potential of the NAD^+/NADH couple (-0.885 V) was found to be rather slow, and only moderately temperature dependent.

It was determined that NAD^+ is adsorbed on a GC electrode surface. The kinetics of NAD^+ adsorption was found to be surface-charge dependent. The adsorption process was described by the Langmuir isotherm. The corresponding apparent Gibbs free energy of adsorption evidenced that the adsorption process is highly spontaneous.

The influence of electrode potential and electrode material on the purity of regenerated 1,4-NADH was then investigated. It was found that the regeneration of 1,4-NADH from NAD^+ in a batch electrochemical reactor employing non-modified electrodes (GC, Carbon Nanofibers /CNFs/, Ti, Ni, Co and Cd) is feasible. The purity

(recovery) of 1,4-NADH regenerated on these electrodes was found to be highly potential- and material-dependant. The origin of the material/potential dependency was related to the strength of the metal-hydrogen ($M\text{-}H_{ads}$) bond, and thus to the potential dependence of the H_{ads} electrode surface coverage and the kinetics of the subsequent NAD-radical protonation by H_{ads}. Among the above outlined non-modified electrodes, only GC and CNF electrodes were capable of producing the highest 1,4-NADH purity (99-100%), but at very high cathodic potentials (–2.3 V).

Therefore, to produce high-purity 1,4-NADH at lower cathodic potentials, a GC electrode surface was patterned with electrochemically-deposited platinum and nickel nano-particles (NPs). It was demonstrated that when the GC electrode was patterned with Pt NPs, a 100% pure 1,4-NADH product was achieved at –1.6 V, while the Ni nano-patterned GC surface gave 100% pure 1,4-NADH already at –1.5 V. The high purity of 1,4-NADH formed on the two nano-patterned electrodes was prescribed to the formation of $Pt\text{-}H_{ads}$ and $Ni\text{-}H_{ads}$ at significantly lower potentials than on bare GC and CNFs surfaces. It was found that purity of 1,4-NADH regenerated on the nano-patterned electrodes was dependent on the electrode potential, nano-particles size, and their surface coverage.

Considering the energy input, the cost of the electrode, and the percentage of recovery of 1,4-NADH (*i.e.* its purity), the GC-Ni electrode was suggested as the electrode of choice for 1,4-NADH regeneration among all investigated electrodes (GC, CNF, Ti, Co, Cd, Ni, GC-Pt and GC-Ni).

RÉSUMÉ

Nicotinamide-adénine-dinucléotide NAD(H) est une coenzyme qui participe à un grand nombre de processus biochimiques dans lesquels elle agit comme une transporteuse d'électrons et d'atomes d'hydrogène. Par conséquent, le NAD(H) se trouve en deux formes d'oxydo-réduction: en forme oxydée, comme NAD^+, et en forme réduite, comme 1,4-NADH. En dépit de sa forte utilisation potentielle dans l'industrie, son utilisation actuelle est très limitée à cause de son coût très élevé (en particulier celui du 1,4-NADH) et la nécessité d'être ajouté en quantités stœchiométriques dans les réacteurs biochimiques. Par conséquent, il est nécessaire de développer des méthodes de régénération *in-situ* du 1,4-NADH. Les méthodes électrochimiques sont d'un intérêt particulier en raison de leur coût potentiellement faible et l'isolement facile du produit. Cependant, le problème majeur dans la régénération électrochimique du 1,4-NADH est la formation d'un dimère enzymatiquement inactif, NAD_2.

Ce projet de doctorat est axé sur (i) l'étude des aspects fondamentaux de l'interaction du NAD^+ avec la surface d'un électrode en carbone vitreux (GC), en termes de la cinétique de réduction et l'adsorption du NAD^+ sur la surface du GC, et (ii) le développement d'électrodes pour la régénération électrocatalytique *directe* (non-médiatisée) du composé 1,4-NADH, active enzymatiquement actif.

Les mesures de polarisation potentiodynamique ont montré que dans les conditions expérimentales utilisées, la réaction de réduction du NAD^+ est contrôlée par la diffusion. Cette irréversible (nécessite une surtension de plus de -550 mV) et est de pseudo-premier ordre par rapport au NAD^+. La cinétique de réduction du NAD^+ sur GC, an *potentiel formel* du couple NAD^+/NADH (-0.885 V), est lente, et modérément dépendante de la température.

Le NAD^+ est adsorbé sur la surface de l'électrode en GC. La cinétique d'adsorption du NAD^+ s'est avérée dépendante de la charge surfacique. Le processus d'adsorption a été décrit par l'isotherme de Langmuir. L'énergie de Gibbs d'adsorption correspondante a montré que le processus d'adsorption est très spontané.

L'influence du potentiel et du matériel de l'électrode sur la pureté du 1,4-NADH régénéré, a ensuite été étudiée. Il a été constaté que la régénération de 1,4-NADH à partir

de NAD^+, dans un réacteur électrochimique discontinu, employant des électrodes non modifiés (GC, nanofibres de carbone /CNFS /, Ti, Ni, Co et Cd) est possible. La pureté (récupération) du 1,4-NADH régénéré sur ces électrodes a été jugée dépendante du potentiel et du matériel de l'électrode. L'origine de cette relationentre la nature elu nature ela matériel et le potentiel été liée à la force de liaison métal-hydrogène ($M\text{-}H_{ads}$), et donc à la couverture du H_{ads} sur la surface de l'électrode, que dépend du potentiel. Seuls les électrodes en GC et CNF ont été capables de produire la plus haute pureté du composé 1,4-NADH (99-100%), mais à des potentiels cathodiques le élevés (-2.3 V).

Donc, pour produire 1,4-NADH de haute pureté à faibles potentiels cathodiques, la surface d'une électrode en GC a été modifiée par des nanoparticules (NPs) de platine et nickel, déposées par voie électrochimique. Il a été démontré que lorsque l'électrode en GC a été modifiées avec des NPs de Pt, le produit 1,4-NADH, avec une pureté de 100%, a été obtenu à -1.6 V, tandis que l'électrode en GC modifiée avec les NPs de Ni a produit 1,4-NADH avec une pureté de 100% déjà à -1.5 V. La haute pureté du 1,4-NADH formée sur les deux électrodes nano- modifiée a été prescrite à la formation des liaisons $Pt\text{-}H_{ads}$ et $Ni\text{-}H_{ads}$ à un potentiel nettement inférieur à celui sur une surface nue en GC. Il a été constaté que la pureté du 1,4-NADH régénérée sur les électrodes nano-modelées est dépendante du potentiel d'électrode, de la taille des nanoparticules et de leur couverture de la surfacique.

Compte tenu de l'apport énergétique le coût de l'électrode, et le pourcentage de récupération du 1,4-NADH (*i.e.* sa pureté), l'électrode GC-Ni a été suggéré l'électrode de choix pour la régénération du 1,4-NADH parmi tous les électrodes étudiés (GC, CNF, Ti, Co, Cd, Ni, GC-Pt et GC-Ni).

AKNOWLEDGMENTS

I would like to express my sincere gratitude and deepest appreciation to my supervisor, Prof. Sasha Omanovic, for his excellent guidance, caring, patience, exceptional availability and providing me with an excellent atmosphere for doing research. I have learned to walk as a professional because of his broad knowledge, support, kind attitude, perceptive encouragement and unmatchable guidance, which has taught me modesty, confidence, patience, dynamism, fairness, and to be a better human being. This work would have never been possible without his support. Among all the people whom I have/will come across in life, he will always stand out for his kindness, support, understanding, character and dedication.

I am thankful to all members of Electrochemical Research Group at McGill (Hesam, Mehdi, Sajjad, Mario, Mark, Saloumeh, Nathan, Bebul, Tariq and Amardeep) for their help and support during the research. I am also thankful to all of my friends Farkhund, Sagheer, Laiq and Salman. I would like to express my sincere gratitude and hearty feelings to Saad Ghareba and Nehar Ullah for giving support in times of need. I would like to use this opportunity to thank Frank, Ranjan, Andrew, Gerald, Emily, Louise and Jo-Ann for all the help they provided during my research.

Words fail to express my appreciation of my wife Farhat Jabeen whose dedication, love, and persistent confidence in me has taken the load off my shoulder. I owe her for her unselfishness and allowing her intelligence, passions, and ambitions collide with mine.

I am also grateful to my parents, brothers, sisters and children (Manahil, Roman, Waleed, and Ayaan) and other family members for their prayers and moral support which have always motivated me to go the extra mile.

The University of Engineering and Technology Peshawar, Pakistan and NSERC are greatly acknowledged for funding my research.

TABLE OF CONTENTS

LIST OF FIGURES

LIST OF TABLES

LIST OF SCHEMES

NOMENCLATURE

A	absorption intensity
A	pre-exponential factor in the Arrhenius equation (A cm^3 mol^{-1})
ATR-FTIR	attenuated total reflectance-Fourier transform infrared spectroscopy
b	UV/Vis cavette length (cm)
B_{ads}	adsorption affinity constant (dm^3 mol^{-1})
[-]	concentration (mol cm^{-3} or mM or mol L^{-1})
C	capacitance (F cm^{-2})
C_{dl}	double-layer capacitance (F cm^{-2})
CNF	carbon nanofiber
CPE	constant phase element (Ω^{-1} s^n cm^{-2})
CV	cyclic voltmmetry
D	diffusion coefficient (cm^2 s^{-1})
DC	differential capacitance (A cm^{-2})
DL	double-layer
DPV	differential pulse voltammetry
E'	formal potential (V)
EDTA	ethylenediaminetetraacetic acid
EEC	electrical equivalent circuit
EIS	electrochemical impedance spectroscopy
E_p	peak potential (V)
ΔE	modulation amplitude (V)
F	Faraday constant (96,485 C mol^{-1})
FAD	flavin adenine dinucleotide
FEG-SEM	field-emission scanning electron microscope
ΔG_{act}	apparent Gibbs energy of activation (kJ mol^{-1})
$\Delta G_{act,LV}$	apparent Gibbs energy of activation determined at a LV peak potential (kJ mol^{-1})

$\Delta G_{act,DPV}$	apparent Gibbs energy of activation determined at a DPV peak potential (kJ mol^{-1})
ΔG_{ads}	Gibbs free energy of adsorption (kJ mol^{-1})
GC	glassy carbon
GC-Pt	glassy carbon-platinum
GC-Ni	glassy carbon-nickel
HER	hydrogen evolution reaction
HLADH	horse liver alcohol dehydrogenase
HPLC	high performance liquid chromatography
I_d	mass-transport-limited current (A)
I_e	electron-transfer current (A)
I_p	peak current (A)
j	current density (A cm^{-2})
k_a	adsorption kinetic constant (dm^3 mol^{-1} s^{-1})
k_d	desorption kinetic constant (sec^{-1})
k_f	transformation constant (sec^{-1})
k_{eff}	effective heterogeneous electron-transfer rate constant (A cm^3 mol^{-1})
k^f	apparent formal heterogeneous electron-transfer rate constant (cm s^{-1})
LV	linear voltammetry
LADH	liver alcohol dehydrogenase
LDH	lactate dehydrogenase
LiDH	lipoamide dehydrogenase
LDH-CLC	cross-linked lactate dehydrogenase crystals
MV	methyl viologen
MSE	mercury/mercurous sulphate electrode
MWCNs	multi-walled carbon nanotubes
n	number of electrons
n	exponent of a constant phase element
NPs	nano-particles
nPt	nano-particulate platinum
PABS	poly-aminobenzene sulfonic acid

PM-IRRAS	polarization modulation infrared reflection absorption spectroscopy
R	standard gas constant (8.314 J mol^{-1} K^{-1})
R	resistance (Ω cm^2)
R_{el}	electrolyte resistance
RVC	reticulated vitreous carbon
S	substrate
SEM	scanning electron microscope
SHE	standard hydrogen electrode
sr	scan rate (V s^{-1})
SS	stainless steel
t_m	modulation time (s)
T	temperature (K)
TGA	thermogravimetric Analysis
W	Warburg impedance element (Ω^{-1} $s^{1/2}$ cm^{-2})
$W_{1/2}$	width of a DPV peak (at half height) (V)
WE	working electrode
X	conversion (%)
Z	impedance (Ω cm^2)

Greek letters

α	transfer coefficient
η	overpotential (V)
τ	time constant (s)
θ	NAD^+ surface coverage
ν	kinematic viscosity (cm^2 s^{-1})
ω	radial frequency (rad s^{-1})

Further in the text, terms "purity" and "recovery" will refer to the percentage of enzymatically-active 1,4-NADH present in the <u>product</u> mixture, which might contain 1,4-NADH, and enzymatically-inactive NAD_2 and various NADH isomers, excluding the non-reacted initial reactant, NAD^+.

CHAPTER 1: INTRODUCTION

1. INTRODUCTION

In enzymatic catalysis, enzymatic cofactors are usually required along with specific enzymes. One of the cofactors used in redox enzymatic reactions is nicotinamide adenine dinucleotide NAD(H). NAD(H) is a dinucleotide (Fig. 1.1), containing two nucleotides joined through their phosphate groups with one nucleotide containing an adenosine ring, and the other containing electrochemically-active nicotinamide ring. Several hundred (about 700) enzymes are known to use NADH as a cofactor in various biochemical processes [1-10]. In all these processes, NAD(H) serves as a proton and electron transport molecule. Hence, NAD(H) can be found in two redox forms; in an oxidized, NAD^+, and in a reduced, NADH, form (the only enzymatically-active isomers of the latter is 1,4-NADH). In its reduced form, NADH, transfers two electrons and a hydrogen to a substrate (S), in the presence of suitable enzyme, forming the oxidized form, NAD^+:

$$1,4-NADH + S + H^+ \xleftrightarrow{enzyme} NAD^+ + SH_2 \qquad (1.1)$$

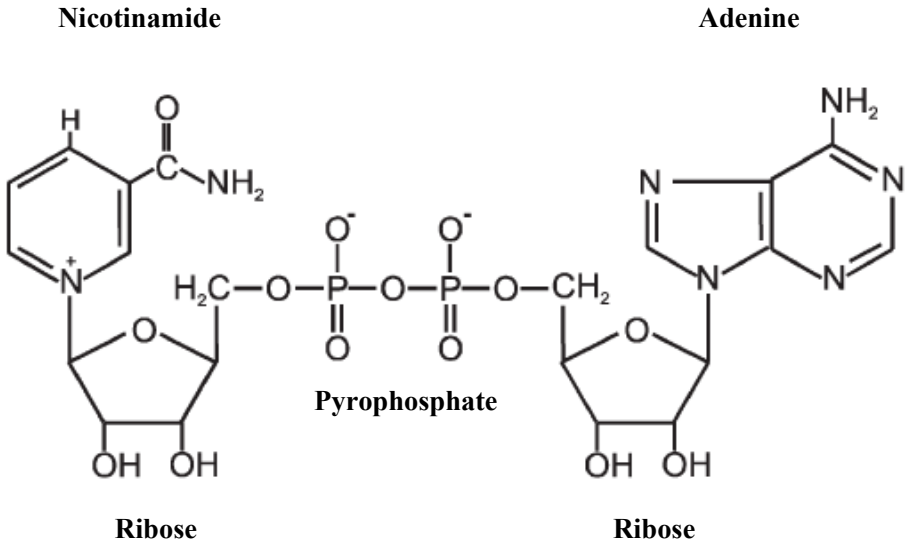

Figure 1.1: Nicotinamide adenine dinucleotide in its oxidized form (NAD^+).

NAD(H) is a cellular fuel for every living cell, therefore, in nature, it is found in all living cells and used during cellular respiration involving redox enzymes [1, 2, 6]. A

precursor for forming NADH in the human body is nicotinamide (vitamin B-3). Apart from its use in metabolic reactions, it also participates in aerobic biotransformation of toxic Cr(VI) to non-toxic Cr(III) [11].

In industry, it is of importance in the field of chiral compounds preparation [12]. It participates in enzymatic catalysis of industrially important synthetic reactions where conventional chemical catalysts fails [13]. NAD(H) is also used for posttranslational modifications, therapy of some certain medical conditions and diseases such as Alzheimer's and Parkinson, in pharmacology, biotechnology, biosensors, and the synthesis of new high-value-added compounds such as pharmaceuticals, food additives, perfumes, insecticides and pesticides [14-22]. Thus, the enzymes that are capable to make and use NAD^+ and NADH play a vital role in the current pharmacology and the research into future treatments for diseases [14]. Furthermore, the coenzyme is used in a number of redox enzymatic reactions that have promising applications in the biotechnology area. For example, it is employed in the synthesis of L-tert-lucine (developed by Degussa, now Evonik), which is used as a high-quality intermediate in the synthesis of medications to treat cancer and AIDS [21].

In all these enzymatic reactions, it is critical to provide NAD(H) at stoichiometric quantities (Eq. 1.1). However, due to an extremely high cost, especially that of the reduced form, 1,4-NADH, it is currently used in industry only in a limited number of processes for which the cost of the final product can justify the use of expensive cofactor 1,4-NADH. The cost of various forms of nicotinamide adenine dinucleotide is compared in Table 1.1.

Table 1.1: Cost of Nicotinamide cofactors [23] – note that the compound purity is not specified. For more detail on pricing consult Sigma Aldrich.

Cofactor	$ mol^{-1}
NAD^+	710
NADH	3,050
NADP	25,780
NADPH	216,100

Thus, there is a great interest to develop (preferably *in-situ*) 1,4-NADH regeneration methods, which would enable the re-use of 1,4-NADH initially introduced into a (bio)reactor to lower the production cost and therefore, the cost of the final product.

Generally, a good 1,4-NADH regeneration system should satisfy the following requirements [20]:

(a) The thermodynamics should be favorable ($\Delta G < 0$).
(b) The kinetics should be favorable (the regeneration should be fast and the regeneration reaction should be selective).
(c) The cofactor stability should be good (e.g. 1,4-NADH should not decompose during the regeneration).
(d) In addition, good 1,4-NADH regeneration system should enable formation of highly-pure enzymatically-active 1,4-NADH.

With respect to the regeneration of a reduced form of the cofactor, 1,4-NADH, several regeneration methods have so far been employed: enzymatic, electrochemical, chemical, photochemical and biological [23]. Enzyme-mediated electrochemical processes have been usually used to continuously regenerate the enzymatically-active 1,4-NADH. However, these systems are rather complex and expensive and lack long-term stability, mostly due to the denaturation of the enzyme, loss of the electron mediator and slow 1,4-NADH regeneration rate [24]. On the other hand, non-enzyme-mediated electrochemical methods are of particular interest due to their potentially low cost, a simple monitoring of the reaction progress, and there is no need to add a reducing agent, thus enabling relatively simple product isolation [23, 25-27].

The electrochemical regeneration of 1,4-NADH from NAD^+ is a two-step process (Scheme 1).

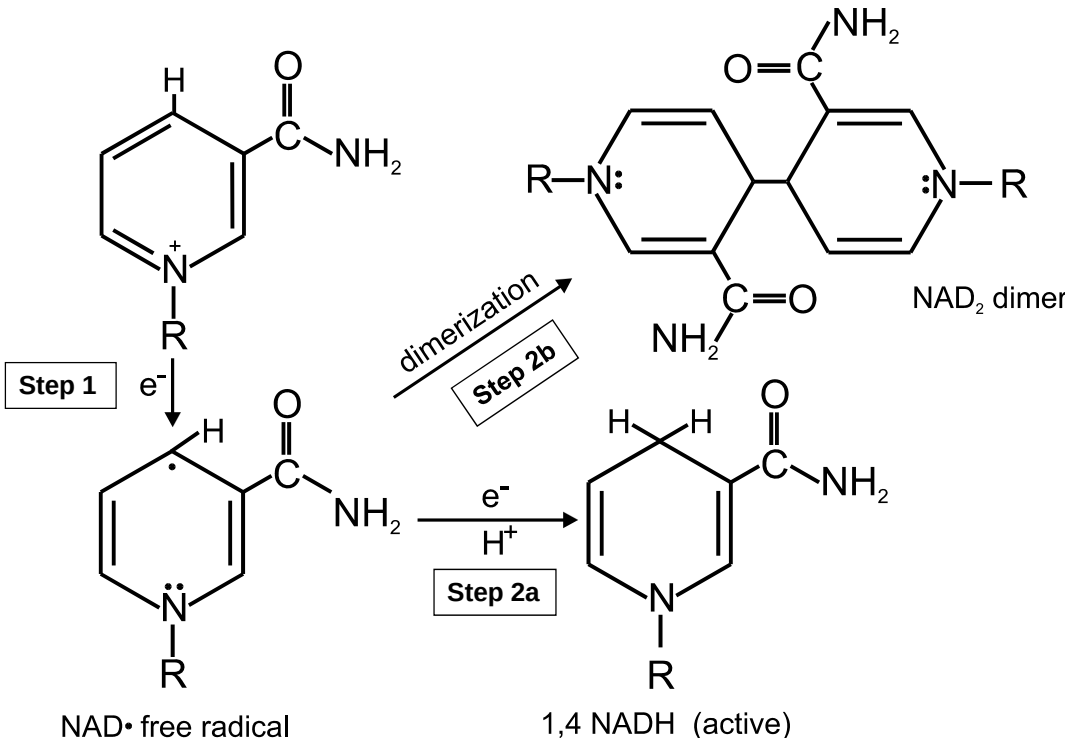

Scheme 1: Reduction of NAD^+ to NAD_2 and enzymatically-active 1,4-NADH. R = adenosine diphosphoribose.

In Step 1, NAD^+ is reduced to give a NAD-radical, which is further reduced and protonated in Step 2a to give 1,4-NADH. Step 2a is considered to be slow due to the slow protonation of the NAD-radical [24, 28-36]. This, in turn, can result in a very fast dimerization of two neighboring NAD-radicals to produce enzymatically-inactive dimer, NAD_2 (Step 2b).

Non-modified (bare) metal electrodes would be the best candidates for electrochemical regeneration of enzymatically-active 1,4-NADH. However, literature reports that on bare (non-modified) electrodes, the kinetics of Step 2b is significantly faster than that of Step 2a, and thus the major product of NAD^+ reduction on these electrodes is NAD_2. This formation of the dimer reduces the recovery of enzymatically-active 1,4-NADH that could be produced (regenerated). The literature reports that the amount of enzymatically-active 1,4-NADH regenerated on non-modified electrodes ranges from below 1% on a reticulated vitreous carbon [37] to 76% on Hg [34, 38-42].

To address the above mentioned problems, many research groups have been developing methods for 1,4-NADH regeneration [1, 43-47]. Although, they demonstrated success in developing electrodes that can give some appreciable (relative to NAD_2) amounts of 1,4-NADH (note that most of papers do not explicitly report this percentage), many of these electrodes are complex, expensive and/or not stable for a long-term use. Therefore, for industrial purposes, there is still a need to develop a stable and cheap electrode surface that would enable *direct* electrochemical regeneration of 1,4-NADH at high-purity [48, 49].

Highly-pure enzymatically-active 1,4-NADH could be obtained by the minimization of the dimer formation (Step 2b, Scheme 1) either by physical prevention of its formation at a molecular level, (e.g. using self-assembled-monolayers and nano-island) or by facilitating the rate of protonation and second electron transfer (Step 2a, Scheme 1). This could be done by the modification of a surface that offers high hydrogen overpotential (glassy carbon (GC), gold (Au)) with nano-islands of a metal that offers low hydrogen overpotential (Pt, Ru, Ir, Ni, Co) which can then result in a significant recovery of the enzymatically-active 1,4-NADH. The above two approaches have been proposed by the Omanovic laboratory, at McGill University.

In an attempt to bring technologies based on the use of 1,4-NADH closer to wide-spread commercialization, this PhD project is focused on the development of electrodes for the *direct* (non-mediated) electrocatalytic regeneration of enzymatically-active 1,4-NADH. GC was chosen as the base working electrode material. This is because it offers high hydrogen reduction overpotential, thus minimizing the interference of this reaction with the NAD^+ reduction reaction [50]. In addition, GC is a good candidate material for industrial applications, due to its relatively low cost and stability. Pt and Ni were selected as these are good hydrogen evolution catalyst. In addition, the influence of electrode potential on the activity of some selected non-modified metal electrodes in regenerating 1,4-NADH was investigated.

The PhD. project was divided into two major parts. The first part dealt with the fundamental aspects of NAD^+ interaction with GC electrode in terms of (i) the NAD^+ reduction kinetics, and (ii) NAD^+ adsorption. The purpose of the study was to get better

insight into fundamental electrochemical and physico-chemical processes that are involved in the reduction of NAD^+ at a GC surface. This served as a basis for further design of multicomponent nano-patterned catalysts for the regeneration of 1,4-NADH. The second part focused on the development and application of bi-functional (nano-patterned) electrodes for the *in-situ* regeneration of enzymatically-active 1,4-NADH in addition to some selected non-modified metallic electrodes and carbon nano fibers (CNFs). The electrochemical regeneration of enzymatically-active 1,4-NADH was investigated as a function of various parameters such as electrode potential, electrode material, nano-particle size, and its surface coverage.

The structure of this thesis is as follows:

- Chapter 1 focuses on the importance of cofactor NAD(H), and outlines the problem of the electrochemical 1,4-NADH regeneration.
- Chapter 2 presents the literature review of the 1,4-NADH regeneration approaches that have so far been employed.
- Chapter 3 is dedicated to the major and specific objectives of the presented research. It also outlines main approaches examined in this PhD project.
- Chapter 4 represents the experimental methodology and methods/instrumentation used in the research.
- Chapter 5 is divided into two major parts. The first part discusses results on the fundamental aspects of the interaction of NAD^+ with a GC electrode surface, such as the NAD^+ reduction kinetics and adsorption. In the second part, the results on the development and application of bi-functional (nano-patterned) electrode surfaces, such as GC-Pt and GC-Ni, for the electrocatalytic regeneration of enzymatically-active 1,4-NADH are presented. In addition, the use of some selected non-modified electrode surfaces (bare metals) and CNFs for the electrochemical regeneration of 1,4-NADH is presented.
- Chapter 6 outlines the main conclusions obtained from the presented results.
- Chapters 7 and 8 outline the original contributions and suggestions for future work, respectively.

CHAPTER 2: BACKGROUND AND LITERATURE REVIEW

2. BACKGROUND AND LITERATURE REVIEW

Because of a very high price of enzymatically-active 1,4-NADH (Table 1.1), and the fact that it needs to be used in stoichiometric quantities in the enzymatic reactions, its current use in industry is limited. Thus, it would be of great importance to regenerate 1,4-NADH *in-situ* in a biochemical reactor, or on a biosensor's surface, or in a biofuel cell. A number of approaches have been employed in an effort to regenerate 1,4-NADH [23]. Regeneration reactions can be divided in several categories: uncatalyzed, chemically catalyzed, electrochemically (catalyzed), enzymatically catalyzed, or "catalyzed" by living cells [20].

Electrochemistry offers one of the best approaches for 1,4-NADH regeneration because of its greater flexibility, simplicity and potentially low cost. Many different approaches such as (i) bare (non-modified) electrodes, (ii) chemically-modified electrodes and (iii) enzyme-modified (mediated) electrodes have been used in designing electrode systems for *in-situ* electrochemical regeneration of enzymatically-active 1,4-NADH.

In this section an overview of different approaches/systems employed for the regeneration of enzymatically-active 1,4-NADH, and thus for the reduction of NAD^+, is presented.

2.1 Electrochemical regeneration of 1,4-NADH / electrochemical reduction of NAD^+ on bare (non-modified) electrodes

In order to understand the NAD^+ reduction kinetics better and try to control the 1,4-NADH regeneration reaction, many research groups have studied fundamental aspects of the mechanisms and kinetics of NAD^+ reduction and 1,4-NADH oxidation using mostly bare (non-modified) metallic electrodes such as mercury [31, 32, 35, 40, 42, 51-55] and a variety of carbon materials [56, 57]. In many of these cases the goal was to develop methods for the reduction of NAD^+ to enzymatically-active NADH isomer, 1,4-NADH, *i.e.* for the *in-situ* regeneration of 1,4-NADH.

However, the major problem that arises in the *direct* reduction of NAD^+ to 1,4-NADH on bare (non-modified) electrodes is the predominant formation of an enzymatically-inactive NAD_2 dimer (Step 2b, Scheme 1), due to the slow kinetics of the second electron transfer and hydrogenation (Step 2a, Scheme 1).

Thus, on a Hg electrode, NAD^+ is first reduced to give a NAD-radical at a very high negative overpotential, followed by very fast dimerization of two neighboring NAD-radicals to produce enzymatically-inactive dimer, NAD_2, (Step 2b, Scheme 1) [31, 32, 35, 54]. Indeed, a very large negative overpotential is needed to *partially* reduced the formed radical to both the enzymatically-active 1,4-NADH and enzymatically-inactive 1,6-NADH. Consequently, the main product of NAD^+ reduction on these electrodes is enzymatically-inactive dimer NAD_2 rather than enzymatically-active 1,4-NADH. A very similar scenario occurs on other non-modified electrodes, as described in the literature. Consequently, due to the dimer formation the amount of enzymatically-active 1,4-NADH regenerated on non-modified electrodes ranges from below 1% on a reticulated vitreous carbon [37] to 76% on Hg [34, 38-42].

Therefore, it appears that there is a need to modify bare metallic electrode surfaces in order to regenerate 1,4-NADH at a (significantly) higher recovery (purity).

2.2 Electrochemical regeneration of 1,4-NADH / electrochemical reduction of NAD^+ on chemically-modified electrodes

Due to the problem of NAD_2 formation on bare metallic electrodes, chemically *modified* electrodes have been used in the NAD^+ reduction process in an attempt to obtain high-purity enzymatically-active 1,4-NADH. For this purpose, different mediators are used to facilitate electron transfer between the electrode surface and NAD^+. For example, Long and Chen [46] attached L-histidine to a silver electrode by a covalent bond. The electrode was capable of producing 82% of enzymatically-active 1,4-NADH. Similarly, Baik *et al*. [45] used an unmodified gold-amalgam electrode and obtained a very low amount of enzymatically-active 1,4-NADH (ca. 10%). With a bare platinum electrode, it increased to 50%, but when the cholesterol modified gold amalgam electrode was used, the amount increased to almost 75%. Although the authors did not discuss the origin of

the increased amount, the Omanovic laboratory speculated that this increase was due to the presence of the cholesterol layer that served as a *physical barrier* to the formation of inactive dimer NAD_2, *i.e.* as the physical fence between the two neighboring active radicals.

In another study, Eulalia *et al*. [44] used conductive vanadia-silica xerogels for the *direct* electrochemical regeneration of enzymatically-active 1,4-NADH. It was shown that the electrochemical regeneration of 1,4-NADH was favorably performed through the coupled reaction of α-ketoglutarate to L-glutamate in the presence of enzyme glutamate dehydrogenases, GDH (GDH was encapsulated in vanadia-silica matrices). In a control experiment, the reaction conversion (not the 1,4-NADH recovery) was only 30%. However, using an unmodified platinum electrode in the presence of vanadia-silica xerogels, they showed that the proposed system resulted a significant improvement in the reaction conversion from 30% to 100%, but the authors did not report the recovery of enzymatically-active 1,4-NADH obtained.

Shimizu *et al*. [58] immobilized Rh^{3+} ions into a polymeric anion doped-polypyrrol (PA/PPy) membrane coated on the graphite electrode in order to regenerate enzymatically-active 1,4-NADH. The amount of 1,4-NADH obtained ranged from 26% to 51.7% depending on the polymeric anion (PA) and polymer matrix used, with the highest NAD^+ to (both active and inactive) NADH conversion degree of ca. 50% with Rh^{3+} immobilized in a poly styrenesulfonate ion doped polyaniline ($Rh^{3+}/PSS^-/PAn$) electrode.

Similarly, Beley and Collin [37] used Rh(III)-bis-terpyridine pyrrole complex for the electrochemical reduction of NAD^+ to 1,4-NADH, which involved electro-polymerization process on a reticulated vitreous carbon electrode in order to create a stable polymeric film. It was shown that the electrocatalytic regeneration of 1,4-NADH using such a *modified* electrode was favorably performed through the coupled reduction of cyclohexanone to cyclohexanol, in the presence of enzyme lipoamide dehydrogenase, LADH, as shown in Fig. 2.1. However, the Fig. 2.1 demonstrates that this approach is rather complex and can suffer from a number of problems (leakage of chemicals out of the film, deactivation of the enzyme, electron-mediator mass-transport

problems, etc.). Depending on the applied electrode potential, the conversion of NAD^+ to 1,4-NADH obtained ranged from 6.6% (–1.15 V) to 30% (–1.25 V).

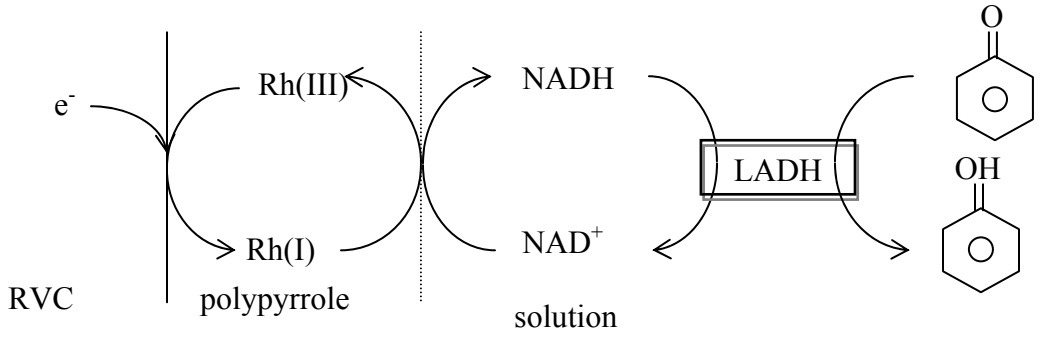

Figure 2.1: Electrocatalytic regeneration of 1,4-NADH using a Rh(III)-bis-terpyridine pyrrole complex and cyclohexanone as substrate and liver alcohol dehydrogenase (LADH) as enzyme [37].

Vuorileho *et al*. [59] reduced NAD^+ and $NADP^+$ in the presence of (pentamethylcyclopentadienyl-2,2'-bipyridine aqua) rhodium (III) as mediator. They observed that the mediator was stable and strongly adsorbed on the carbon surface. The proposed system was able to reduced 99% of the $NAD(P)^+$ to NAD(P)H.

Wang and Tang *et al*. [60] designed a biosensor based on the integration of room-temperature ionic liquids (1-butyl-3-methylimidazolium tetrafluoroborate, BMIM.BF4) and multi-walled carbon nanotubes (MWNTs) with polymeric matrix (chitosan, CHIT). The authors proved that the proposed system has good 1,4-NADH regeneration efficiency and fouling resistant. However, the work was concerned with a biosensor development, not a bioreactor electrode development.

Further, Abdollah *et al*. [43] modified a GC electrode with carbon nanotubes and ruthenium (III) complexes. They concluded that the developed electrode showed a response to acetaldehyde in the presence of alcohol dehydrogenase. Hence, the system was able to reduce NAD^+ into NADH. However, the work was of a more fundamental nature and the authors did not report the recovery of 1,4-NADH on this electrode.

Ashok Kumar *et al*. [61] used a new composite polymer based material that was synthesized electrochemically by using poly-aminobenzene sulfonic acid (PABS) and flavins on GC electrodes. They observed that the system is suitable for both the electrocatalytic oxidation of NADH, and reduction of NAD^+. However, no mention on

the recovery of enzymatically-active 1,4-NADH on this electrode was made. In addition, the work was concerned with electrochemical sensors development, not a bioreactor electrode development.

In another study, Hyun-Kon Song *et al.* [62] used nano-particulate platinum (nPt) in the presence of primary organometallic mediator (Pentamethylcyclopentadienyl-2, 2-bipyridinechloro) rhodium (III) for 1,4-NADH regeneration. The nano-particulate platinum (nPt) performed two functions; first, it worked as a homogeneous catalyst and second as a secondary mediator. In the presence of both nPt and primary organometallic mediator the amount of regenerated 1,4-NADH was up to 20% on platinum disk electrodes. This increased was attributed to the catalytic power of nPt. The authors completely rejected the idea that the increased surface area, after the adsorption of nPt on the working electrodes, was responsible for the higher amount of 1,4-NADH, because they showed that the same amount of 1,4-NADH was obtained by using bare and nPt-adsorbed GC electrodes. However, no recovery of enzymatically-active 1,4-NADH was reported.

Using the concept of electron mediators, Warriner *et al*. [63] modified a platinum electrode with a poly (3-methyl thiophene): poly (phenol red) film. This film performed the function of electron mediator in the NAD^+ reduction reaction (1,4-NADH regeneration) at low overpotential, compared to a bare electrode. The authors successfully demonstrated that a certain amount of 1,4-NADH was regenerated by the system (which was developed as a biosensor), but the actual recovery was not reported.

Karyakin *et al*. [64] developed an electrocatalyst for 1,4-NADH regeneration in a biosensor. A GC electrode modified with poly (neutral red)/NAD^+ /alcoholdehydrogenase /Nafion was used for this purpose. Using the developed electrodes system, it was shown that it can easily detect acetaldehyde. Hence, regeneration of enzymatically-active 1,4-NADH was successful but the recovery was not quoted.

Suss-Fink *et al*. [65] studied five water-soluble rhodium, iridium and ruthenium complexes containing 1,10-phenanthroline $[(C_5Me_5)Rh(phenanthroline)Cl]^+$ to regenerate enzymatically-active 1,4-NADH from NAD^+ in the presence of format as a hydrogen source. The system was able to regenerate a certain amount of 1,4-NADH, as the

reduction of ketone to corresponding alcohol, catalyzed by enzyme alcohol dehydrogenase from *Rhodococcus sp.* (S-ADH) or horse liver alcohol dehydrogenase (HLADH), was possible. Thus, the authors concluded that the proposed five cationic complexes in the presence of sodium format were able to promote the reduction of NAD^+ to 1,4-NADH, but the recovery of enzymatically-active 1,4-NADH was not reported.

In conclusion, it is clear from the literature overview presented above that chemically *modified* electrodes are capable, up to certain extent, to minimize the dimer formation (Step 2b, Scheme 1) and increase the kinetics of NAD-radical protonation (Step 2a, Scheme 1). However, there are problems associated with the use of these chemically *modified* electrodes such as low selectivity, lack of long-term stability and durability due to the loss of the electron mediator under the applied reaction conditions and complexity of the system.

2.3 Electrochemical regeneration of 1,4-NADH / electrochemical reduction of NAD^+ on enzymatically-modified electrodes

Due to the above mentioned problems of chemically *modified* electrodes, enzyme-based electrodes for 1,4-NADH regeneration from NAD^+ have attracted a considerable scientific attention. Fry *et al*. [66-68] immobilized methyl viologen (MV) and enzyme lipoamide dehydrogenase (LiDH) on GC and vitreous carbon electrode surfaces under a Nafion film to prevent the loss of both enzyme and mediator. They showed that this electrode could catalyze the reduction of NAD^+ to 1,4-NADH but the recovery of 1,4-NADH was not reported. The NADH regeneration process was tested by coupling the MV/LiDH system with lactate dehydrogenase (LDH) to convert pyruvate to lactate (Fig. 2.2) [66]. It was summarized that cross-linked lactate dehydrogenase crystals (LDH-CLC) have high stability and retain their enzymatic activity as biocatalysts during electroenzymatic electrolysis for long times. Thus, they concluded that this new form of LDH will be an attractive component in schemes for recycling redox cofactor during electroenzymatic synthesis reactions. However, Omanovic and co-workers have shown that reduction of MV induces a very rapid deactivation of LiDH, even though, some minor amount of enzymatically-active 1,4-NADH was also observed [69]. The suspicion

is, therefore, that the system used by the Fry group actually did not act as an enzyme-mediated 1,4-NADH-regeneration system, but rather as the *direct* regeneration system, capable of producing a small recovery of enzymatically-active 1,4-NADH.

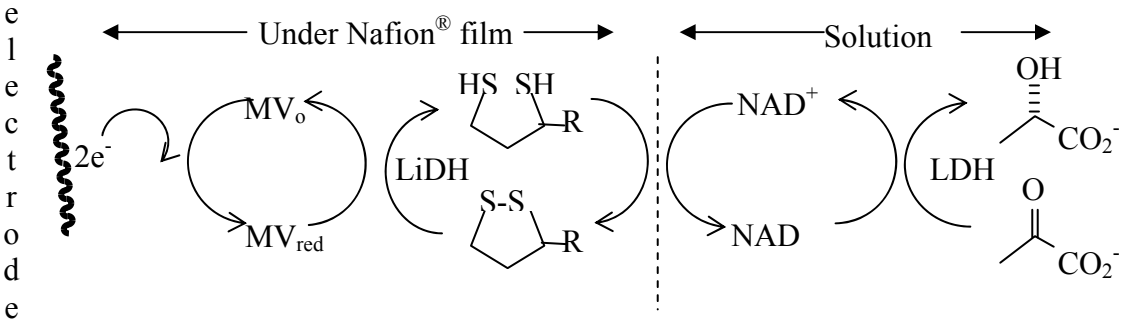

Figure 2.2: Schematic of the system used by the Fry group. Immobilized methyl viologen (MV) and enzyme lipoamide dehydrogenase (LiDH) on GC and vitreous carbon electrode surfaces under a Nafion film and lactate dehydrogenese (LDH), NAD^+, and pyruvate in solution [66].

Further, Lin and Chen [70] used flavin adenine dinucleotide (FAD) modified zinc oxide films electrodes and investigated their electrocatalytic properties in NAD^+ reduction. Similar studies have been reported in the literature on electrocatalytic properties of some other *modified* electrodes using various electrochemical techniques [71-73]. These modified electrodes showed some electrocatalytic activity for redox NAD^+/NADH reactions. However, all these studies are concerned with fundamental aspects of NAD^+ reduction reaction not bioreactor development for 1,4-NADH regeneration.

Chen *et al*. [74] studied *in-situ* electroenzymatic regeneration of cofactor 1,4-NADH in packed-bed membrane reactors through the coupled reaction of pyruvate to lactate. In order to increase the efficiency of the system to regenerate 1,4-NADH, a mediator, methyl viologen, and an enzyme, lipoamide dehydrogenase, were used (they directly immobilized LiDH and MV on a porous graphite electrode, and the electrodes were then coated with a Nafion film). The conversion of pyruvate to lactate was successful. It was shown that about 70% lactate in 24 hours was obtained in a flow-by packed-bed reactor while it took 200 hours to get 50% lactate in a batch reactor.

However, in the paper the actual recovery of enzymatically-active 1,4-NADH was not reported.

Kim *et al.* [75, 76] studied the electrocatalytic reduction of NAD^+ to enzymatically-active 1,4-NADH in the presence of an electron mediator. They used methyl viologen as a mediator between the immobilized diaphorase enzyme and the gold-amalgam electrode surface. They observed that this electrode was able to reduce certain amount of NAD^+ to 1,4-NADH, but the actual recovery was not reported.

Matsue *et al*. [77] also used a LiDH immobilized electrode coupled with viologen as a mediator to catalyze the reduction of NAD^+ to 1,4-NADH. The dimer formation was minimized to a minimum level at the LiDH-HLADH (lipoamide dehydrogenase-horse liver alcohol dehydrogenase) co-immobilized electrode. The product conversion (cyclohexanone to cyclohexanol) efficiency of 70% was achieved.

Similarly, Delecouls-Servat *et al*.[18], designed two-membrane electrochemical reactors in which they carried out the reduction of cyclohexanone to cyclohexanol in the presence of HLADH. In these reactors methyl viologen or rhodium complexes were used as an electron mediator for the electrochemical regeneration of 1,4-NADH. To catalyze the reaction between MV^{o+} and NAD^+, methyl viologen needs the enzyme lipoamide dehydrogenase. On the other hand, no enzyme is required when NADH regeneration is carried out with the rhodium complexes. To ensure the contact of enzyme with the electrode surface, a semi permeable membrane was installed in the filter-press electrochemical reactor. The authors found that under the best applied conditions in the reactor, viologen converted from 0 to 65% of cyclohexanone to cyclohexanol. Finally, a 100% conversion was achieved in the recycling mode when a rhodium complex was used as electron mediator. However, it should be noted that the recovery of enzymatically-active 1,4-NADH regenerated was not reported in this work.

Kane Cheikhou *et al*. [78] developed an electrochemical filter-press microreactor by electroerosion, to perform chiral enzymatic syntheses by converting pyruvate to L-lactate in the presence of L-LDH as an enzyme and flavin adenine dinucleotide ($FAD/FADH_2$) as a redox mediator. In addition, formate dehydrogenase was used as an enzyme to reduce NAD^+ to 1,4-NADH. In order to get high specific area of the cathode,

semicylindircal channels were created, which were then separated by Nafion membrane. The cathode was able to continuously regenerate certain amount of 1,4-NADH. However, the actual recovery of enzymatically-active 1,4-NADH regenerated was not reported.

2.4 Electrochemical regeneration of 1,4-NADH / electrochemical reduction of NAD^+ on metal-nano-island-modified electrodes

From the above discussion, it is clear that enzymatic modification of an electrode surface is a promising method to prevent the formation of inactive dimer (Step 2b, Scheme 1) and thus increase the recovery of active 1,4-NADH. However, these systems are very complex and expensive and lack long-term stability, mostly due to the denaturation of the enzyme, loss of the electron mediator and slow NADH regeneration rate.

Therefore, for industrial purposes, there is still a need to develop a stable and cheap electrode surface that would enable *direct* electrochemical regeneration of enzymatically-active 1,4-NADH at high recovery (purity).

An important contribution in this field was made by Azem *et al.* [24] who modified a GC electrode with a sub-monolayer of ruthenium, which has resulted in a very high recovery (ca. 98%) of enzymatically-active 1,4-NADH regenerated in a batch electrochemical reactor operated at different electrode potentials. In another study [28], they used both bare (Au and Cu) and *modified* (Au-Pt) metallic electrodes to *directly* regenerate enzymatically-active 1,4-NADH in a batch electrochemical reactor. They concluded that the recovery of enzymatically-active 1,4-NADH strongly depends on the electrode potential and type of the working electrode used in the reactor. Furthermore, the authors proved that an increase in the recovery of 1,4-NADH can be achieved by modifying a bare metal electrode that offers high hydrogen evolution overpotential (e.g. GC or Au) with a sub-monolayer of good hydrogen evolution catalyst (e.g. Ru or Pt). Table 2.1 shows a summary of various electrodes on which Omanovic *et al*. regenerated the enzymatically-active 1,4-NADH, together with the corresponding recovery.

Table 2.1. Efficiency comparison of various methods/systems in regeneration of enzymatically-active 1,4-NADH at industrially relevant 1,4-NADH regeneration potentials (-1.5 V / -1.6 V_{MSE}).

Electrode	GC-Ru	Au-Pt	e-Enz*	Cu	Au
Recovery of active NADH / %	98	64	54	54	28

* LiDH/MV/GC electrode system

The above values can be compared with literature (highest efficiency at optimum conditions):

- Au-Hg: 10% [45]
- Pt (non-modified): 50% (expensive) [45]
- Au-Hg/cholesterol: 75% (not stable) [45]
- Pt/anion_charged_memb: 65% (poor long-term stability) [79]
- Hg: 50% (toxic – cannot be used) [34]
- Rh^{3+}_PPY/C: 52% (poor long-term stability) [58]

From the literature survey presented above, the following conclusions can be drawn:

- The amount of enzymatically-active 1,4-NADH regenerated on *non-modified* electrodes is highly potential dependant and a very low recovery of enzymatically-active 1,4-NADH is obtained.
- The *enzymatic* regeneration method is complex, expensive and unstable.
- The *direct* electrochemical 1,4-NADH regeneration method is of low cost, product isolation is easy and no stoichiometric reactant is required. However, in this approach enzymatically-inactive NAD_2 is formed due to the fast dimerization reaction in addition to the slow protonation and electrons transfer reaction.

As proposed by the Omanovic laboratory, one of the promising solutions to above mentioned problems is to modify an electrode surface with metal nano-islands to avoid

formation of NAD_2. As previously demonstrated, this method could increase the amount of enzymatically-active 1,4-NADH regenerated. However, more fundamental research is needed to deduce the influence of various factors on the mechanisms and kinetics of NADH regeneration and the recovery of 1,4-NADH on these surface *modified* electrodes, in order to design a robust electrode system capable of performing satisfactorily during a longer time period in a real biochemical reactor. In addition, the literature lacks information on the influence of electrode potential on the 1,4-NADH regeneration, particularly in terms of the purity of enzymatically-active 1,4-NADH that could be recovered from NAD^+. Further, the 1,4-NADH regeneration reaction is a heterogeneous reaction, involving several basic steps: mass-transport of NAD^+ from the bulk solution to the electrode surface, adsorption of NAD^+ at the electrode surface, its reduction (Scheme 1), and finally the desorption of the products (NADH, NAD_2) and their mass-transport into the bulk electrolyte. However, the data on these processes is very scarce, especially that on the NAD^+ adsorption. Therefore, this thesis project also involved research on some fundamental aspects of the NAD^+ reduction reaction, with the goal of better understanding the reaction mechanisms and kinetics, to build the knowledge required for the design of better 1,4-NADH regeneration electrodes.

Consequently, main objectives of the current thesis are further outlined in the next chapter.

CHAPTER 3: OBJECTIVES

3. OBJECTIVES

Bare (non-modified) metal electrodes would be best candidates for electrochemical regeneration of enzymatically-active 1,4-NADH, but unfortunately the major problem in the electrochemical regeneration of 1,4-NADH on these electrodes is the formation of an enzymatically-inactive NAD_2 dimer (Step 2b, Scheme 1), due to the slow protonation of the NAD-radical (Step 2a, Scheme 1).

However, the hypothesis of the Omanovic laboratory is that the dimer formation can be minimized by providing 'active hydrogen' ($M\text{-}H_{ads}$) adjacent to the NAD-radical formation site, which will then increase the rate of NAD-radical protonation (Step 2a, Scheme 1) and predominantly enzymatically-active 1,4-NADH, rather than inactive NAD_2. This could be done using the following three approaches:

3.1 By manipulating the electrode potential

Highly-pure enzymatically-active 1,4-NADH on high-overpotential hydrogen electrodes (e.g. GC and CNFs) could be obtained by increasing the electrode potential to more negative (cathodic) values. This will increase the electron-transfer rate as well as the amount of H_{ads} adsorbed on the electrode surface. As the NAD-radical protonation is a strong function of surface concentration of H_{ads}, both of these effects should contribute to an increase in 1,4-NADH production rate from NAD-radical, and thus to the increased recovery of enzymatically-active 1,4-NADH. This was the first approach studied in this PhD project.

3.2 By selecting a proper electrode material

In addition to the effect of electrode potential (above), selecting a proper electrode material could also result in a high recovery of enzymatically-active 1,4-NADH. It was hypothesized by the author of this thesis that the recovery of 1,4-NADH from NAD^+ is dependent not only on the electrode potential, but also on the *strength* of the metal electrode - hydrogen bond ($M\text{-}H_{ads}$). Namely, a metal that binds hydrogen more strongly

(e.g. Ti) will attain a higher hydrogen surface coverage at less negative cathodic potentials (lower NAD^+ reduction overpotentials). Consequently, the higher the hydrogen surface coverage, the faster the kinetics of Step 2a (Scheme 1), and higher the recovery of 1,4-NADH from NAD^+. In an attempt to prove the hypothesis, several selected bare (non-modified) metal electrodes (Ti, Ni, Co and Cd) were investigated in a batch electrochemical reactor operated at different electrode potentials, in addition to GC and CNFs electrodes.

3.3 By modification of electrode surface with nano-islands

Further, to address the problem of fast dimer formation, 'surface-modified' electrodes have been developed in this PhD project. It is important to mention that the Electrochemical Research Group at McGill (the Omanovic Laboratory) has pioneered the development of bi-functional metal nano-patterned electrode surface for 1,4-NADH regeneration [24, 28, 30, 80]. The design of these surfaces has been based on the hypothesis that providing active hydrogen ($M\text{-}H_{ads}$) at the electrode site adjacent to the site of NAD-radical formation, the kinetics of Step 2a (Scheme 1) would significantly increase, and the ratio of the production of active 1,4-NADH over inactive NAD_2 would increase. To provide high surface coverage of hydrogen at the NAD-radical reduction/hydrogenation surface reaction site, good hydrogen evolution catalysts (e.g. Pt, Ru, Rh, Ir, Re, Ni) can be used to form nano-islands (*i.e.* nano-particles, NPs) on a high-overpotential (*i.e.* poor hydrogen catalyst) electrode surface, such as GC or Au [24, 28, 30, 80]. As illustrated in Scheme 2, the role of NPs is to adsorb hydrogen ($M\text{-}H_{ads}$) in the potential region of NAD^+ reduction, and this 'activated' hydrogen would then readily react with a NAD-radical adsorbed on the adjacent GC site, thus minimizing the probability of the dimer formation. Secondly, NPs could also act as a physical boundary for the two neighboring free NAD-radicals to combine with each other, thus high-purity of enzymatically-active 1,4-NADH could be obtained.

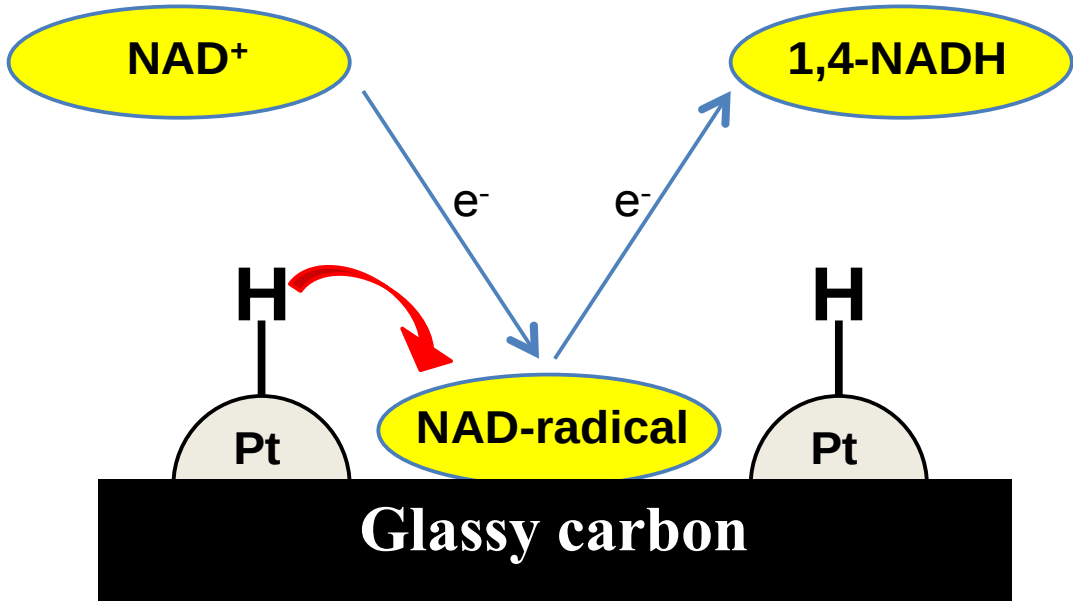

Scheme 2: Representation of the bifunctional character of GC-Pt electrode used for 1,4-NADH regeneration in this project. The purpose of Pt nano-particles is to provide 'active' adsorbed hydrogen (Pt-H_{ads}) at the site of NAD-radical formation. This increases the radical protonation kinetics, and hence minimizes the probability of dimerization of two neighboring radicals, leading to the preferential formation of enzymatically-active 1,4-NADH (Scheme 1).

In this PhD project bi-functional GC-Pt and GC-Ni electrodes for electrocatalytic regeneration of enzymatically-active 1,4-NADH were developed.

3.4 Main objective

The main objective of this PhD project was to develop electrodes and optimize experimental conditions for the *direct* electrochemical regeneration of highly-pure enzymatically-active 1,4-NADH.

3.5 Specific objectives

In order to achieve the main objective of the project, the following specific objectives were defined:

- To investigate the fundamental aspects of the mechanisms and kinetics of the NAD^+ reduction reaction and NAD^+ adsorption on a bare GC electrode.
- To investigate the influence of electrode potential and electrode material (GC, CNFs, Ti, Cd, Co and Ni - all bare, non-modified surfaces) on the purity of 1,4-NADH that could be obtained by the reduction of NAD^+ in a batch electrochemical reactor.
- To modify a GC electrode with nano-islands (nano-particles) of metals that offer low hydrogen overpotential such as Pt and Ni, in order to achieve the *direct* regeneration of the enzymatically-active, high-purity 1,4-NADH.

CHAPTER 4: EXPERIMENTAL METHODS AND MATERIALS

4. EXPERIMENTAL METHODS AND MATERIALS

4.1 Chemicals and solutions

Fundamental aspects of the NAD^+ electrochemical reduction kinetics and adsorption were studied in 0.1 M $NaClO_4$ (HPLC grade, Fisher Scientific S490, pH = 5.8) using a glassy carbon (SPI 4169GC-AB) electrode, at various temperatures (295 to 331 K), electrode potentials (–1.1 to –1.5 V) and NAD^+ concentrations (1 to 5 mM).

Electrochemical regeneration of enzymatically-active 1,4-NADH, from a 1 mM NAD^+ solution in 0.1 M phosphate buffer (pH = 5.8), was performed at 295 K under the potentiostatic conditions. The buffer was prepared by dissolving potassium phosphate monobasic anhydrous, KH_2PO_4 (ACS grade, BioShop PPM 302) in ultra-pure deionized water and adding 1 N NaOH (Caledon Laboratories 7861-6) to adjust pH.

NAD^+ solutions were prepared by dissolving a proper amount of β-NAD^+ (sodium salt, purity 98%, Sigma N0632) in supporting electrolytes.

High purity hydrogen hexachloroplatinate ($H_2PtCl_6 \times 6H_2O$, Fluka 00669) and nickel(II)nitrate hexahydrate ($Ni(NO_3)_2 \times 6H_2O$, Sigma 203874) were used for the formation of metal nano-islands (nano-particles) on the GC surface. All chemicals were used as received, without further purification. Aqueous solutions were prepared using deionized water of resistivity 18.2 MΩ cm.

4.2 Electrochemical cell and electrodes

A conventional two-compartment, three-electrode batch electrochemical reactor (cell) was used in this work. Fig. 4.1 illustrates the electrochemical setup configuration used in the research.

The counter electrode was a graphite rod (McMaster-Carr 9121K71), which was, prior to each use, sonicated for 30 min in ethanol (HistoPrep HC 1300-1GL), followed by thorough rinsing with water. During the measurements, the counter electrode was

separated from the working and reference electrode electrolyte compartment by a glass frit in order to prevent oxygen evolved on it to diffuse to the working electrode and get reduced, thus interfering with the NAD^+ reduction reaction.

A mercury/mercurous sulphate electrode (MSE; +0.642 V *vs.* SHE, Fisher Scientific) was used as a reference electrode, which was placed in the working electrode compartment, very close to the working electrode in order to minimize ohmic (electrolyte) contribution. All the potentials in this work are referred to MSE.

The following electrodes were used as working electrodes (WE):

- Pure (non-modified) electrodes: glassy carbon (GC), carbon non-fibers (CNFs), Ti, Cd, Co and Ni, and
- Nano-patterned GC electrodes: These included GC electrodes on which nano-particles (nano-islands) of Pt and Ni were formed.

In 1,4-NADH regeneration experiments, the total geometric WE area was 12.5 cm^2. All the WE electrodes were made by the thesis author, with the exception of the CNF electrode. The latter was produced by coating a 316 stainless steel mesh with CNFs in a plasma reactor, by Prof. Sylvain Coulombe's laboratory (see Section 4.5).

In NAD^+ reduction kinetics and adsorption measurement, a commercial GC electrode (a 5 mm rod sealed in epoxy resin to give a geometric surface area of 0.196 cm^2) was used. The true (electrochemically-active) surface area of this electrode was determined using $K_4Fe(CN)_6 \times 3H_2O$ (Sigma P9387) [81], which was calculated to be 0.206 cm^2 (see Figs. A.1 and A.2 in Appendix A). Therefore, in kinetics and adsorption studies, all the reported values are referred to the real surface area of the electrode, if not otherwise stated.

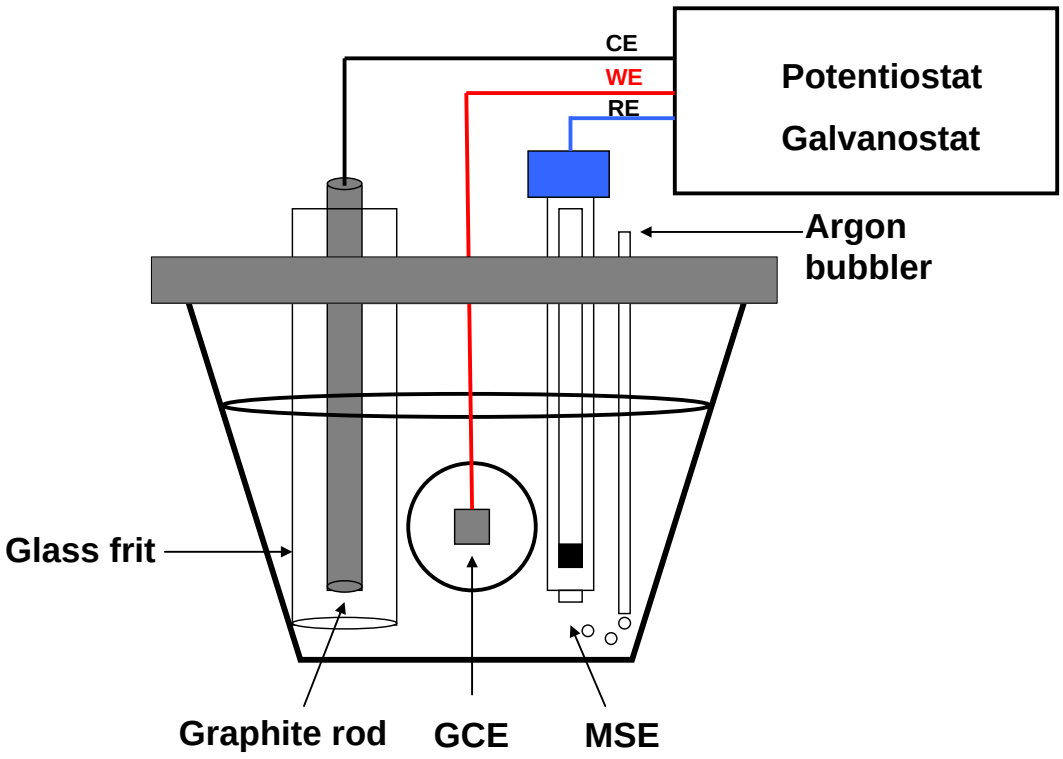

Figure 4.1: Two-compartment three-electrode batch electrochemical cell connected to a potentiostat/galvanostat/frequency response analyzer.

4.3 Equipment

Electrochemical measurements, such as linear polarization voltammetry (LV), cyclic voltammetry (CV), differential pulse voltammetry (DPV), electrochemical impedance spectroscopy (EIS), differential capacitance (DC) and controlled-potential electrolysis, were performed using an Ecochemie Autolab potentiostat/galvanostat/frequency response analyzer PGSTAT30/FRA2, controlled by the GPES/FRA v.4.9.5 software.

The surface morphology of the prepared nano-patterned GC-Pt and GC-Ni electrodes was analyzed by a field-emission scanning electron microscope (FEG-SEM Phillips XL30). For the surface image processing, open-source ImageJ software was

used. The progress of the NAD^+ reduction reaction and activity assay was monitored by a Varian UV-Vis double beam spectrophotometer. In adsorption studies, ATR-FTIR spectroscopy was employed using a Hyperion microscope and the corresponding ATR objective.

4.4 Electrode surface patterning

Formation of Pt and Ni nano-particles, NPs (nano-islands) on a GC electrode surface (*i.e.* electrode surface patterning) was performed by electrochemical deposition of Pt and Ni using the electrochemical cell in Fig. 4.1. Before each surface nano-patterning (electrode modification), the GC surface was carefully wet-polished with polishing paper (grid 1200/4000) until a mirror finish was obtained, followed by degreasing with ethanol and sonication for 5 min in ethanol in order to remove polishing residues. To ensure a clean GC surface, the electrochemical pretreatment of the GC surface was carried out in 0.5 M H_2SO_4 (Fisher Scientific 351293) by cyclic potentiodynamic polarization between –1.5 V and 1.1 V at a scan rate of 100 mV s^{-1}, for 50 cycles. Nano-islands of Pt were formed on such a freshly prepared GC surface by performing electrochemical cyclic voltammetry in a solution of 1 mM $H_2PtCl_6 \times 6H_2O$ in 0.5 M H_2SO_4, in the potential range from –0.6 V to 0.1 V, at a scan rate of 50 mV s^{-1}, for a specific number of cycles (specified for each electrode, later in the thesis). Similarly, nano-islands of Ni on GC were formed by performing cyclic voltammetry in 2 mM $Ni(NO_3)_2 \times 6H_2O$ in acetate buffer (Sigma S7670, pH = 4), in the potential range from -0.8 V to 0 V, at a scan rate of 50 mV s^{-1}, for 10 cycles [82]. The two electrodes are termed as GC-Pt and GC-Ni, respectively.

4.5 CNFs synthesis

A stainless steel 316, 400 series mesh (25 μm grid bar, 2.5 cm × 2.5 cm sample size; cleaned ultrasonically in acetone) was used as the CNF formation/growth catalyst and support material. The support was placed within a tubular chemical vapor deposition

furnace (55 mm-inner diameter quartz furnace tube), under argon (592 ± 5 cm^3 min^{-1}), and heated to 973 K. Acetylene was then injected into the furnace for 4 min at a constant flow rate of 100 ± 5 cm^3 min^{-1}. This was followed by an isothermal CNF growth period of 30 min at 973 K under Ar. The system was then allowed to cool to room temperature. This method of growth is based on the work by Baddour *et al.*[83], in which carbon nanotubes and CNFs were grown directly from stainless steel sheets. However, in the current work no pretreatment steps (acid etching) were required.

4.6 Electrochemical regeneration of 1,4-NADH

Electrochemical reduction of NAD^+, *i.e.* the electrochemical regeneration of 1,4-NADH, was performed in the electrochemical cell in Fig. 4.1. However, instead of one, two carbon rod counter electrodes were placed opposite of the two working electrode surfaces, to ensure the uniform electric field. The electrolyte volume was 80 mL and the initial NAD^+ concentration was 1 mM. Two types of electrode surfaces were investigated: (i) bare electrode surfaces; glassy carbon (GC), carbon nano-fibers (CNFs), titanium (Ti), cadmium (Cd), cobalt (Co) and nickel (Ni), and (ii) a GC surface patterned by either Pt or Ni nano-islands (GC-Pt and GC-Ni, respectively). These surfaces served as a working electrode in the batch electrochemical reactor.

In order to determine the actual bioenzymatic activity of the regenerated NADH, the NADH activity tests were made according to the procedure outlined in following section.

4.7 Experimental methodology

All measurements were performed in an oxygen-free electrolyte. In order to achieve this, argon (99.998% pure) was purged through the electrolyte prior and during electrochemical 1,4-NADH regeneration and NAD^+ adsorption measurements. This also ensured convective mass transport of electroactive species to/from the electrode surface. However, in NAD^+ reduction kinetics experiments, after initial oxygen removal, the bubbler was pulled above the electrolyte surface, but the oxygen-free electrolyte and the

inert atmosphere above the electrolyte were maintained by saturating the cell space above the electrolyte with argon.

For the concentration dependent experiments, the stock NAD^+ solution was prepared in a separate container using the supporting electrolyte (0.1 M $NaClO_4$). Before measurements in a NAD^+-containing solution, the background response of the electrode was recorded in 0.1 M $NaClO_4$. Aliquots of NAD^+ were then added to the electrochemical cell and the electrochemical measurements were repeated for each aliquot.

To determine the enzymatic activity of the regenerated 1,4-NADH, activity tests were made according to the regular Sigma Quality Control Test Procedure (EC 1.8.1.4) which was further modified for this purpose using lipoamide dehydrogenase (5.3 U/mg, Calzyme laboratories, Inc. 153A0025) as an enzyme and DL-6,8-thioctic acid amide (Fluka T5875) as a substrate.

First, a volume of 0.2 mL of substrate and 0.1 mL of EDTA (Sigma ED4S) were added into 2.6 mL of regenerated 1,4-NADH in a 4 mL cuvette. The absorbance of the solution at 340 nm was monitored using a UV-Vis spectrophotometer, until reaching a steady state value. Then, 0.1 mL of the enzyme was injected into the cuvette while the absorbance was recorded until reaching a final constant value, signifying that the entire active 1,4-NADH formed during the electrolysis was consumed by the enzymatic reaction (Fig. 4.2).

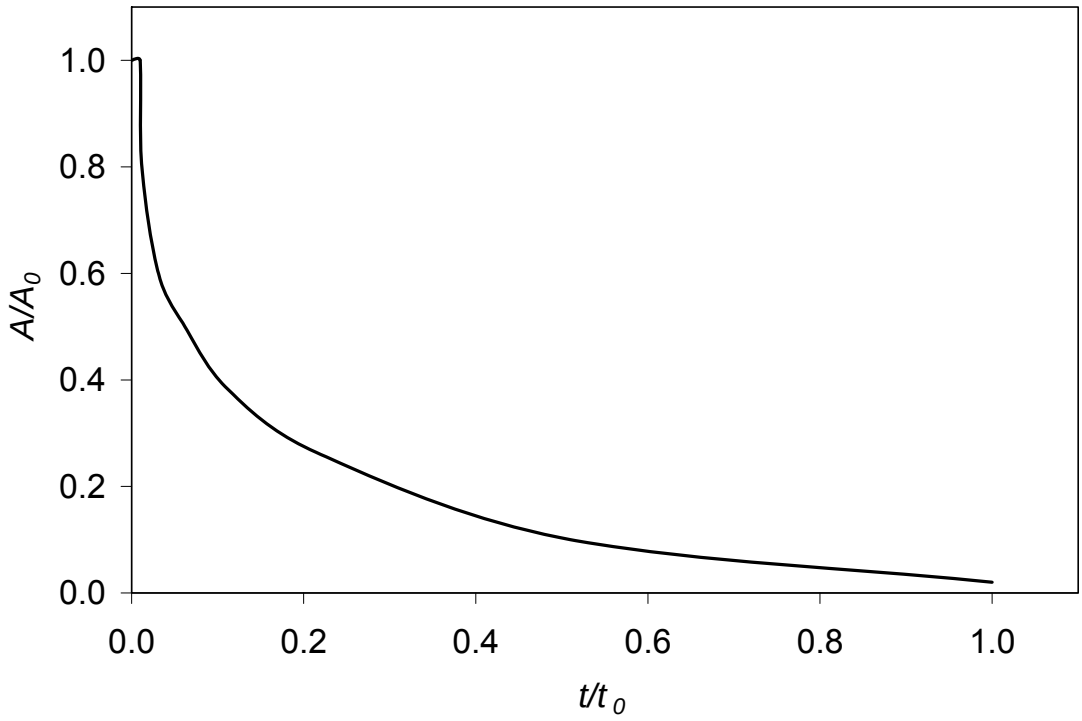

Figure 4.2: Time dependence of normalized absorbance (A/A_0) of 1,4-NADH produced by electrolysis of a 1 mM NAD^+ solution on a GC-Pt electrode at –1.6 V. A_0 is the absorbance value recorded before reaction (4.2) was initiated, while A is the absorbance recorded at any time after the initiation of reaction (4.2).

Finally, taking into account the initial and final absorbance at 340 nm, the purity of enzymatically-active 1,4-NADH produced by electrolysis was calculated (Eq. 4.1).

$$\text{Purity (recovery) of 1,4-NADH (\%)} = \frac{\left[100 - \left(A/A_o\right)\times 100\right]}{\text{initial } NAD^+ \text{ purity (\%)}} \times 100\% \qquad (4.1)$$

The procedure for the activity assay is described in detail below:

Principle:

$$1,4-\text{NADH} + \text{DL-lipoamide} \xrightarrow{\text{lipoamide dehydrogenase}} NAD^+ + \text{dihydrolipoamide} \qquad (4.2)$$

Conditions: T = 293 K, pH = 5.81, $A_{340\text{nm}}$, light path b = 1cm

Method: UV/Vis spectrophotometer

Reagents Preparation:

Reagent A: 0.1 M phosphate buffer, pH 5.8 at 293 K

Prepare 150 mL by dissolving 2.04 g of potassium phosphate monobasic, anhydrous in deionized water. Adjust the pH to 5.8 with 1 N NaOH.

Reagent B: 0.028 M DL-6,8-thioctic acid amide

Prepare 2.5 mL by dissolving 0.01437 g of DL-6,8-thioctic acid amide in 1.5 mL ethanol (nondenatured). Dilute this solution with 1 mL of reagent A. Prepare fresh.

Reagent C: 0.3 M ethylenediaminetetraacetic acid (EDTA) with 2.0 % Albumin solution, pH 5.8.

Prepare 2.5 mL in deionized water using 0.22 g of EDTA and 0.0044 g of albumin bovine (Sigma A0281). Adjust the pH to 5.8 with 1 N NaOH.

Reagent D: Nicotinamide adenine dinucleotide, reduced form (NADH) produced by electrolysis of a 1 mM solution of NAD^+ in phosphate buffer pH 5.8.

Reagent E: Lipoamide Dehydrogenase Enzyme Solution

Immediately before use, prepare a 10 mL solution of lipoamide dehydrogenase in cold reagent A by dissolving 0.0011 g.

Table: 4.1: Pipette (in mL) the following reagents into suitable cuvettes.

Reagent	Reference 1	Reference 2	Test
Reagent A	2.6	2.6	–
Reagent B	0.2	0.2	0.2
Reagent C	0.1	0.1	0.1
Reagent D	–	–	2.6
Reagent E	–	–	0.1

First, zero the absorbance at 340 nm with Reference 1 and Reference 2, and then remove Reference 2 and replace it with "Test" (Table 4.1). Record the change in absorbance at 340 nm with time, until it becomes constant. Then add reagent E and record the absorbance with time until reaching a constant value.

The assay was first calibrated using commercially available NADH that contains 98% of enzymatically-active 1,4-NADH (Sigma N8129).

In order to determine the conversion of NAD^+ to enzymatically-active 1,4-NADH, on different working electrodes, a UV/Vis calibration was curve developed as shown in Fig. 4.3.

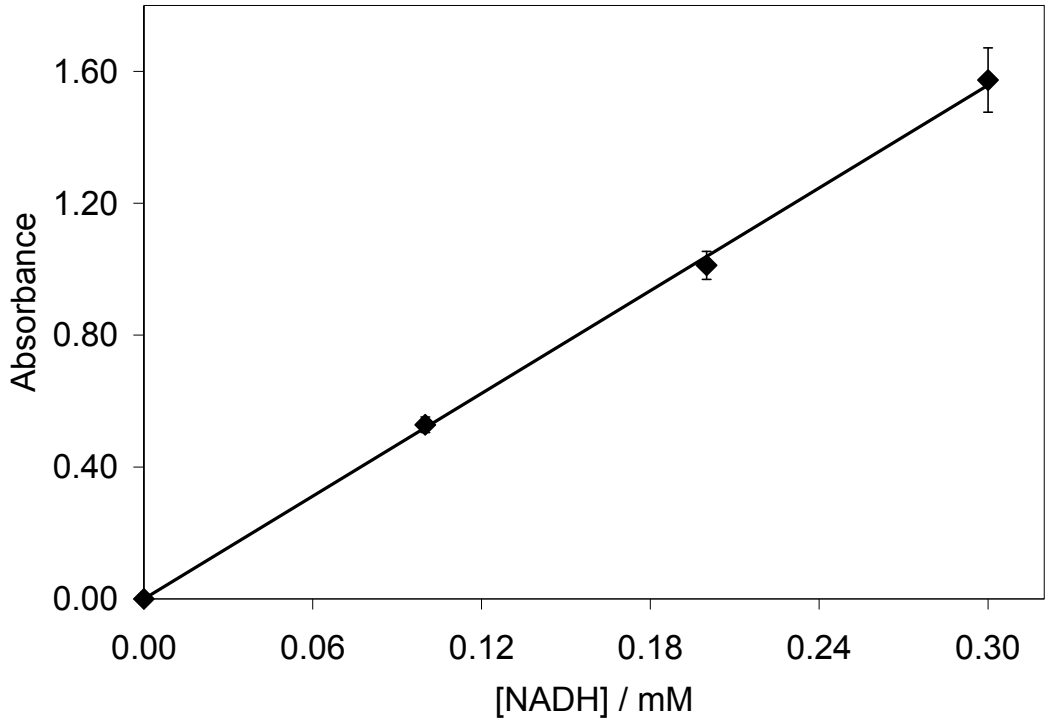

Figure 4.3: Calibration curve for UV/Vis spectrometer.

CHAPTER 5: RESULTS AND DISCUSSION

5. RESULTS AND DISCUSSION

Note: Results of Sections 5.1, 5.3.1.1, 5.3.1.2 and 5.3.2 have been published in the following papers:

1. **I. Ali** and S. Omanovic, *Kinetics of Electrochemical Reduction of NAD^+ on a Glassy Carbon Electrode,* Int. J. Electrochem. Sci., 8 (2013) 4283.
2. **I. Ali,** B. Soomro and S. Omanovic, *Electrochemical Regeneration NADH Employing on Glassy Carbon Electrode Surface: The Influence of Electrolysis Potential,* Electrochem. Comm., 13 (2011) 562.
3. **I. Ali,** M. McArthur, N. Hordy, S. Coulombe and S. Omanovic, *Electrochemical Regeneration of the Cofactor NADH Employing a Carbon Nanofibers Cathode,* Int. J. Electrochem. Sci., 7 (2012) 7675.
4. **I. Ali,** A. Gill and S. Omanovic, *Direct Electrochemical Regeneration of the Enzymatic Cofactor 1,4-NADH Employing Nano-patterned Glassy Carbon/Pt and Glassy Carbon/Ni Electrodes,* Chem. Eng. J., 188 (2012) 173.

This chapter is divided into two major parts. The first part presents the fundamental aspects of NAD^+ interaction with a GC electrode in terms of (i) the NAD^+ reduction kinetics (Section 5.1), and (ii) NAD^+ adsorption (Section 5.2). The purpose of the study was to get better insight into fundamental electrochemical and physico-chemical processes that are involved in the reduction of NAD^+ at a GC surface. The second part is of an applied nature, as it focuses on the actual *in-situ* regeneration of enzymatically-active 1,4-NADH in a batch electrochemical reactor, employing various electrodes. Section 5.3 is further divided into two sub-sections. The first sub-section (5.3.1) presents results on the 1,4-NADH regeneration using selected non-modified metallic electrodes and CNFs cathode while the second sub-section (Section 5.3.2) focuses on the development and application of modified electrodes for 1,4-NADH regeneration.

5.1 Kinetics of NAD^+ reduction on a GC electrode surface

In this section, results on the kinetics of NAD^+ reduction on a GC electrode surface are presented. The results were obtained using electrochemical techniques of

linear voltammetry (LV), differential pulse voltammetry (DPV) and electrochemical impedance spectroscopy (EIS).

5.1.1 Linear polarization voltammetry

LV measurements were first performed in order to obtain the information on the potential region of NAD^+ reduction and initial information on the NAD^+ reduction kinetics. Fig. 5.1 shows the LVs recorded in the absence (curve 1, control curve) and presence (curves 2-6) of NAD^+ in the electrolyte. The control curve shows a typical behavior of a GC electrode, characterized by a wide double layer region (positive of ca. -1.5 V) and the beginning of a hydrogen reduction region (negative of ca. –1.5 V).

However, the curves recorded in the NAD^+-containing electrolyte show a well-defined cathodic current peak at potentials negative of ca. –1.4 V. The peak is related to the NAD^+ reduction reaction, and its position, *i.e.* the potential is in agreement with the literature on NAD^+ reduction on various electrodes [1, 24, 29, 38, 45, 47, 56].

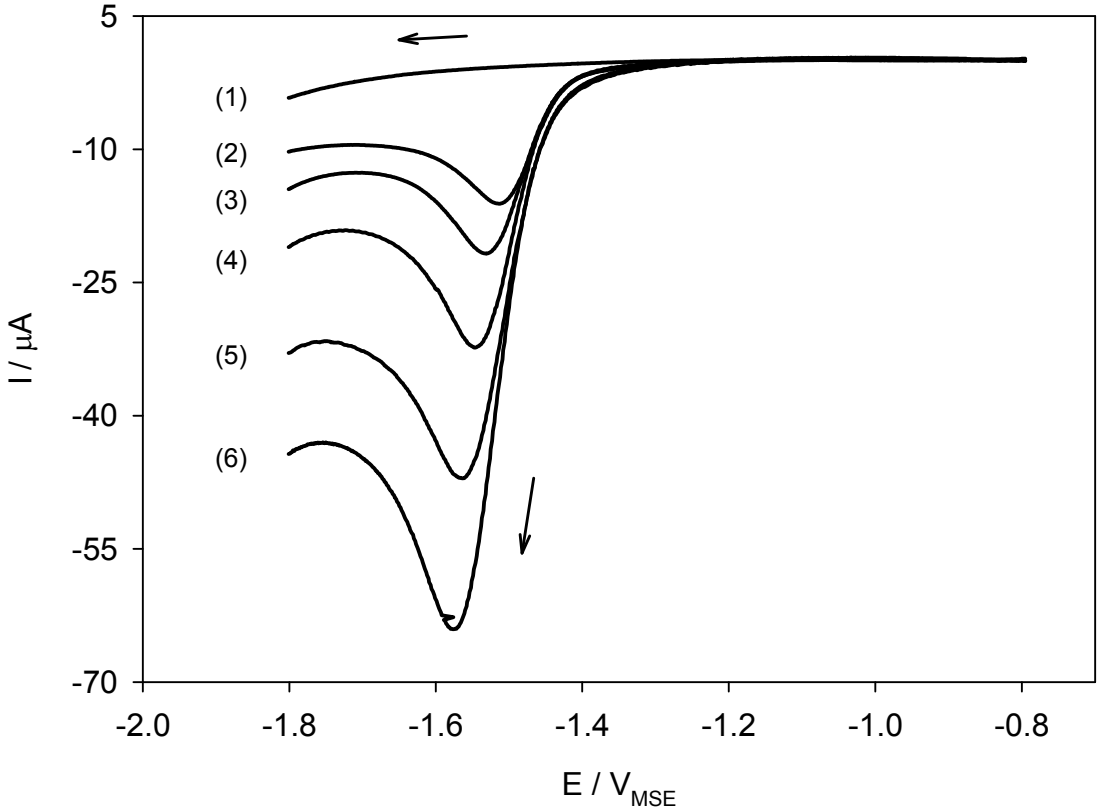

Figure 5.1: Linear voltammograms of NAD^+ reduction on GC electrode recorded in (1) the supporting electrolyte 0.1 M $NaClO_4$, and (2-6) in the supporting electrolyte containing 4 mM NAD^+. Scan rates: (1 and 2) 10, (3) 20, (4) 50, (5) 100 and (6) 200 mV s^{-1}. Temperature, $T = 295$ K.

Fig. 5.1 shows that the NAD^+ reduction reaction is irreversible in the potential region studied. Firstly, the potential difference between the first noticeable NAD^+ reduction current (around –1.3 V) and *formal potential* of the NAD^+/NADH couple, $E' = -0.885$ V (at pH 5.8) is rather high [24, 29, 30]. Secondly, no anodic peak in the returning (positive) cycle was observed even when the anodic limit was extended to 0 V. This high NAD^+ reduction overpotential is due to an unfavorable surface orientation of NAD^+ on the electrode surface [24, 28].

The peak position (potential) in Fig. 5.1 shifts towards more negative potentials with an increase in scan rate. This indicates that the NAD^+ reduction reaction is under mass-transport control. In order to verify this, the dependence between the peak current and square root of scan rate was plotted in Fig. 5.2. The graph shows a linear dependence, thus confirming that the reaction is indeed under mass-transport control under the experimental conditions applied [24, 29, 30, 84, 85].

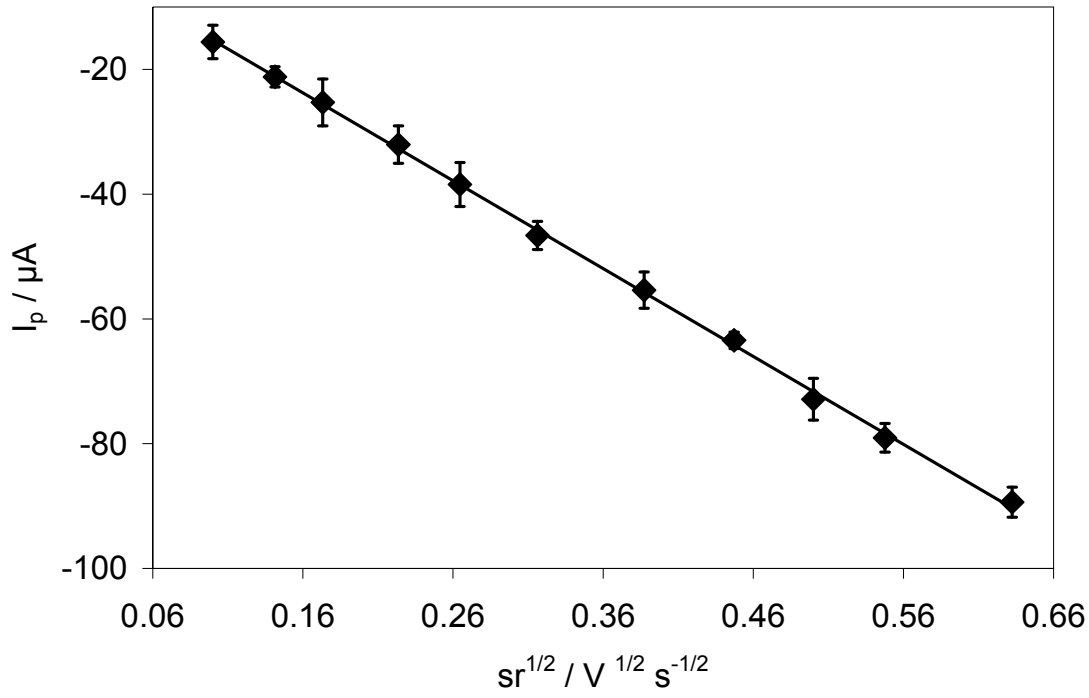

Figure 5.2: Dependence of NAD^+ reduction peak current on the applied scan rate obtained from the voltammograms presented in Fig. 5.1.

Next, a kinetic parameter related to the electron-transfer process was calculated, αn. In this product, α represents the fraction of applied potential used to lower the activation energy for NAD^+ reduction, while n represents a number of electrons exchanged in the NAD^+ reaction. In order to calculate the αn value from the data in Fig. 5.1, the peak potential (E_p) versus logarithm of scan rate (sr) dependence was plotted in Fig. 5.3.

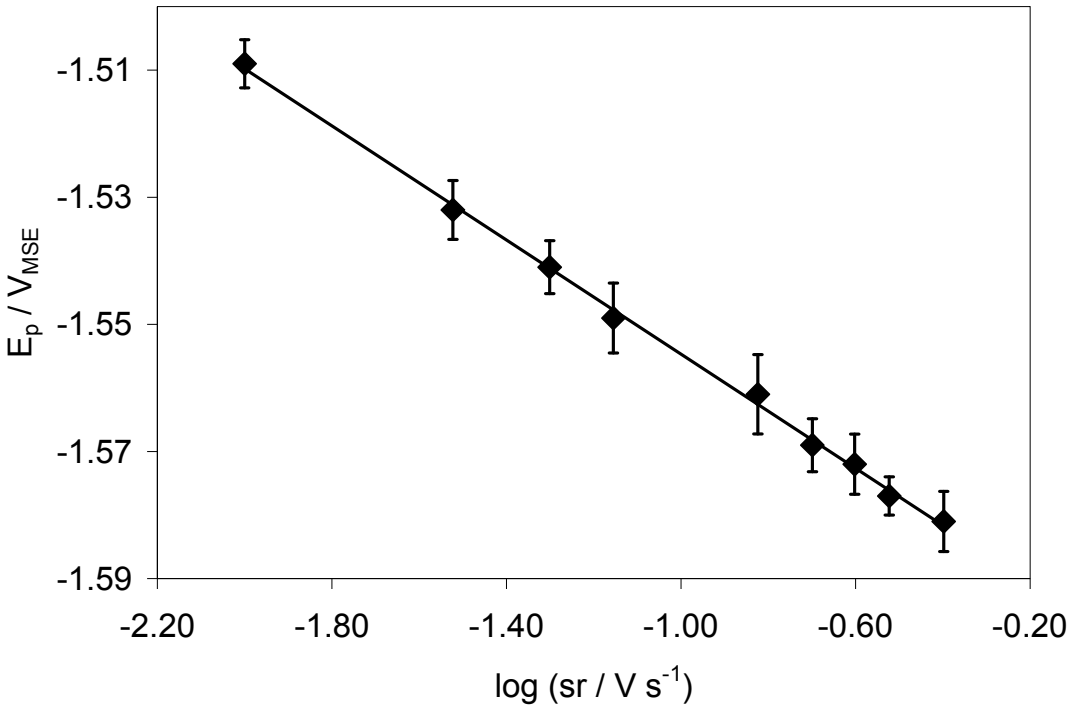

Figure 5.3: Dependence of NAD^+ reduction peak potential on the applied scan rate obtained from the voltammograms presented in Fig. 5.1.

Taking into account that the NAD^+ reduction reaction is irreversible, the following equation can be employed to evaluate the αn product [29, 30, 86-88]:

$$\frac{dE_p}{d\log(sr)} = \frac{-0.029}{\alpha n} \tag{5.1}$$

Where E_p is the peak potential (V) and sr is the scan rate (V s^{-1}). Thus, taking the value of the slope in Fig. 5.3, the product was calculated to be $\alpha n = 0.69$.

This value is consistent with previous studies on Hg, Au and Ru-GC electrodes [24, 29, 42].

It would now be interesting to calculate the actual number of electrons involved in the NAD^+ reduction reaction, since this could provide information on the relative amount of NAD_2 and NADH produced within the potential region of the LV peak in Fig. 5.1. This would provide information on the selectivity of the bare GC electrode in regenerating 1,4-NADH (as opposed to NAD_2). For this purpose, the slope in Fig. 5.2 and the following equation can be used [24, 30, 87, 89, 90]:

$$I_p = 2.99 \times 10^5 nA(\alpha n)^{1/2}[NAD^+]D^{1/2}sr^{1/2} \tag{5.2}$$

where n is the number of electrons participating in the redox reaction, $[NAD^+]$ is the concentration of NAD^+ in the bulk solution (mol cm^{-3}), A is the area of electrode (cm^2), D is the NAD^+ diffusion coefficient in the solution ($cm^2\ s^{-1}$) and sr is the potential scan rate ($V\ s^{-1}$). Taking that $\alpha n = 0.69$, a value of $n = 1.62$ was calculated, and that of apparent transfer coefficient, $\alpha = 0.43$. Now, taking that the NAD_2 formation requires one electron per one NAD^+ molecules, while the formation of 1,4-NADH requires the exchange of two electrons (Scheme 1), the number of electrons calculated from the LV curves in Fig. 5.1 (n = 1.62) indicates that 62% of 1,4-NADH was formed by the reduction of NAD^+ under potentiodynamic conditions in Fig. 5.1.

In order to verify the kinetic information obtained from Figs. 5.2 and 5.3, a set of LVs were recorded at a constant scan rate, but at varying NAD^+ concentrations, Fig. 5.4a.

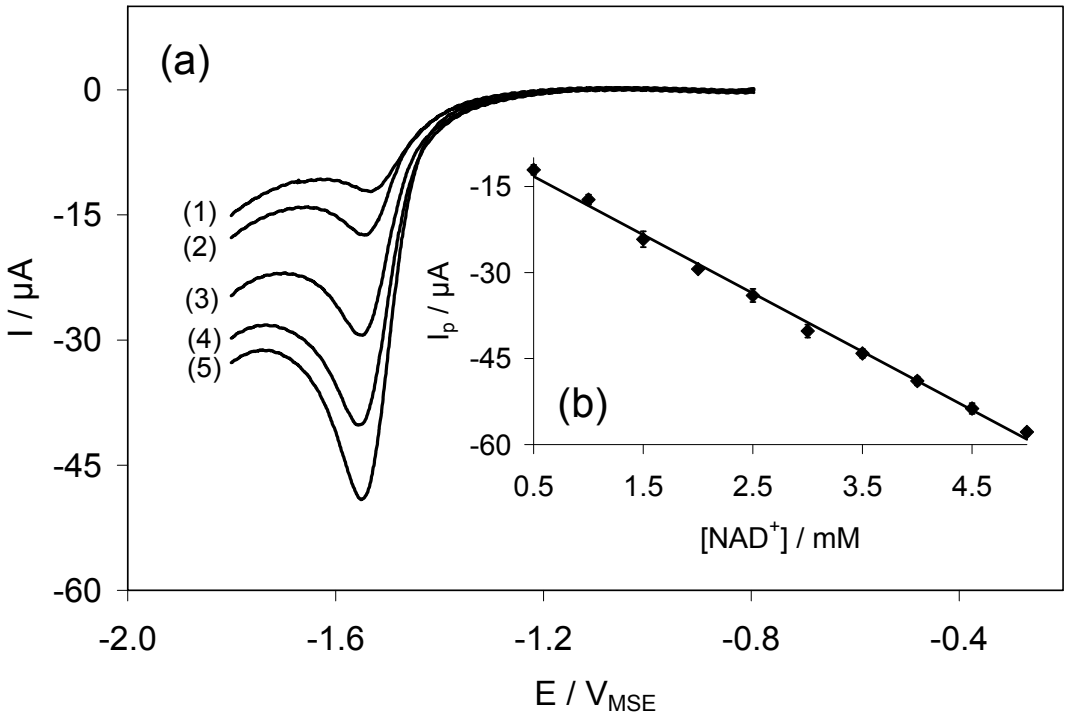

Figure 5.4: (a) Linear voltammograms of NAD^+ reduction on GC electrode recorded in 0.1 M $NaClO_4$ containing various concentrations of NAD^+: (1) 0.5 mM, (2) 1 mM, (3) 2 mM, (4) 3 mM and (5) 4 mM. Scan rate, sr = 100 mV s^{-1}; temperature, T = 295 K. (b) Dependence of the peak current on the NAD^+ concentration obtained from the data presented on the main plot (a).

The plot shows that with an increase in NAD^+ concentration in the solution, the NAD^+ reduction peak current also increases, which is in agreement with Eq. (5.2). Indeed, the inset (Fig. 5.4b) demonstrates that this dependence is linear, as predicted by Eq. (5.2). Thus, taking the previously calculated value of the product αn = 0.69, it was possible to calculate the number of electrons exchanged in the NAD^+ reduction reaction and the corresponding transfer coefficient, n = 1.66 of α = 0.42, respectively. These values are very close to those calculated from LVs in Fig. 5.1.

In addition, since the peak current is proportional to the NAD^+ reduction rate, $d[NAD^+]/dt$, the linear dependence between the NAD^+ reduction peak current and NAD^+ concentration in the bulk solution, Fig. 5.4b, indicates that the NAD^+ reduction reaction is of pseudo-first order with respect to NAD^+, under the experimental conditions performed.

5.1.2 Differential pulse voltammetry

DPV technique was chosen as an independent technique for the verification of the kinetic parameters calculated from LVs in Figs. 5.1 and 5.4, since it is more sensitive to concentration as compared to linear voltammetry.

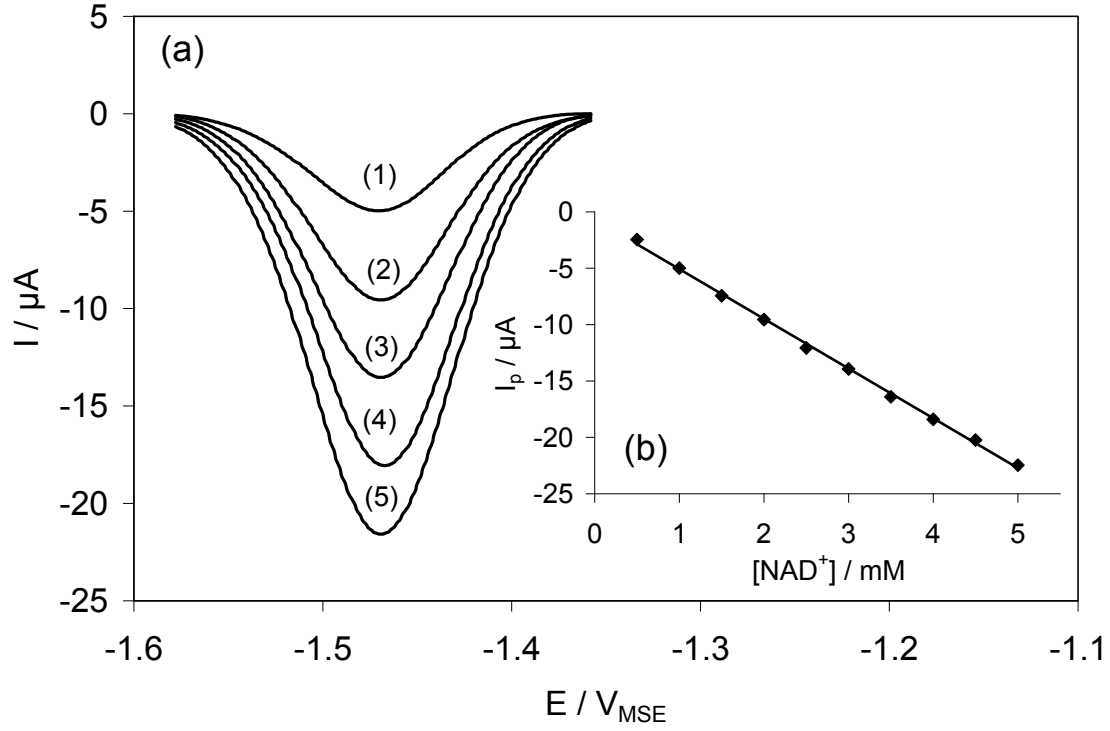

Figure 5.5: (a) Differential pulse voltammograms of NAD^+ reduction on GC electrode, recorded in 0.1 M $NaClO_4$ containing various concentrations of NAD^+: (1) 1 mM, (2) 2 mM, (3) 3 mM, (4) 4 mM and (5) 5 mM. Modulation time, 70 ms; modulation amplitude, 50 mV; interval time, 0.2 s; step potential, 1.5 mV; scan rate, sr = 7.5 mV s^{-1}; temperature, T = 295 K. (b) Dependence of the peak current on the NAD^+ concentration obtained from the data presented on the main plot (a).

Fig. 5.5a shows a set of DPVs recorded at various concentrations of NAD^+ in the supporting electrolyte. With an increase in NAD^+ concentration, the DPV peak current increases, and this behavior is linear, as demonstrated in the inset (Fig. 5.5b). The same as the corresponding behavior obtained in LV measurements presented in Fig. 5.4, the results in Fig. 5.5 also indicate that the NAD^+ reduction reaction on the bare GC electrode is of pseudo-first order with respect to NAD^+. Similar results were also obtained previously in our laboratory on Au [29], and ruthenium-modified GC electrodes [24].

The DPV results in Fig. 5.5 can also be used to calculate the product αn, by determining the width of the DPV peak at its half height, $W_{1/2}$ (V), at each NAD^+ concentration [30, 91]:

$$W_{1/2} = \frac{3.52RT}{\alpha nF} \tag{5.3}$$

where F is the Faraday constant (96485 C mol^{-1}), R is the standard gas constant (8.314 J mol^{-1} K^{-1}), and T is the temperature (295 K). A values αn = 0.97 was obtained. Now, using the following equation [30, 90]:

$$I_p = \frac{nAFD^{1/2}[NAD^+]}{\sqrt{\pi t_m}}\left(\frac{1-\sigma}{1+\sigma}\right) \tag{5.4}$$

where for an irreversible electrochemical reaction [30, 92]:

$$\sigma = \exp\left(\frac{\alpha nF\Delta E}{2RT}\right) \tag{5.5}$$

where t_m represents modulation time (s) and ΔE is the modulation amplitude (V), a number of electrons involved in the NAD^+ reduction reaction performed under the experimental conditions in Fig. 5.5 was calculated to be n = 1.54. This indicates that ca. 54% of 1,4-NADH was formed by the reduction of NAD^+. A slightly lower number of electrons exchanged (and hence the percentage of 1,4-NADH regenerated) in comparison to the LV measurements in Figs. 5.1 and 5.4 is due to the fact that the DPV peak is located at more positive potentials (ca. –1.47 V) in comparison to LV peaks (Fig. 5.3). Namely, as it was demonstrated by our previous work [36], the percentage of 1,4-NADH regenerated is potential dependent, and at –1.4 V it was 32% and at –1.5 V it was 64%. Employing linear interpolation, the percentage of 1,4-NADH regenerated at –1.47 V would be ca. 54%, which agrees well with the value obtained from Fig. 5.5. Table 5.1 summarizes kinetic values calculated from LV and DPV measurements. For comparison, the table also lists the corresponding values obtained from long-term NADH regeneration experiments performed in a batch electrochemical reactor employing a GC electrode [36].

As evidenced, the obtained values agree very well, thus verifying the accuracy of the LV and DPV values and the methods employed to obtain them.

Table 5.1: Kinetic parameters for NAD^+ reduction on a GC electrode obtained from different experimental electrochemical techniques.

Technique	Type	n_{exp}	α_{exp}
LV	Scan dependent	1.62	0.43
	Concentration dependent	1.66	0.42
DPV		1.54	0.63
Enzymatic assay (-1.47 V)		1.54*	
Enzymatic assay (-1.50 V)		1.64	
Average value		1.62	0.49
Standard deviation		0.05	0.12

* This value was calculated by the interpolation, as described in the text.

5.1.3 Electron transfer-rate constant and activation energy

To calculate a value of apparent *formal* heterogeneous electron-transfer rate constant, k^f, number of electrons, n, and the apparent transfer coefficient, α, LV and DPV voltammograms recorded at various scan rates and NAD^+ concentrations were fitted by a kinetic model for an irreversible electrochemical reaction (see Appendix B) using the Ecochemie General Purpose Electrochemical System software [93]. Fig. 5.6 demonstrates that an excellent agreement between the simulated (solid line) and experimental (symbols) voltammograms was obtained. The mean value of the apparent formal heterogeneous electron-transfer rate constant calculated from scan- and concentration-dependent LV measurements is $k^f = (6.1 \pm 2) \times 10^{-14}$ cm s^{-1}. A close value was also obtained from concentration-dependant DPV measurements $k^f = (2.5 \pm 1) \times 10^{-14}$ cm s^{-1}. Previous studies on the Au electrode also yields such low values [29]. These low values indicate very slow kinetics of the NAD^+ reduction reaction at the *formal potential* of the NAD^+/NADH couple (–0.885 V). This was expected considering the irreversibility / high overpotential of the NAD^+ reduction reaction on a GC electrode.

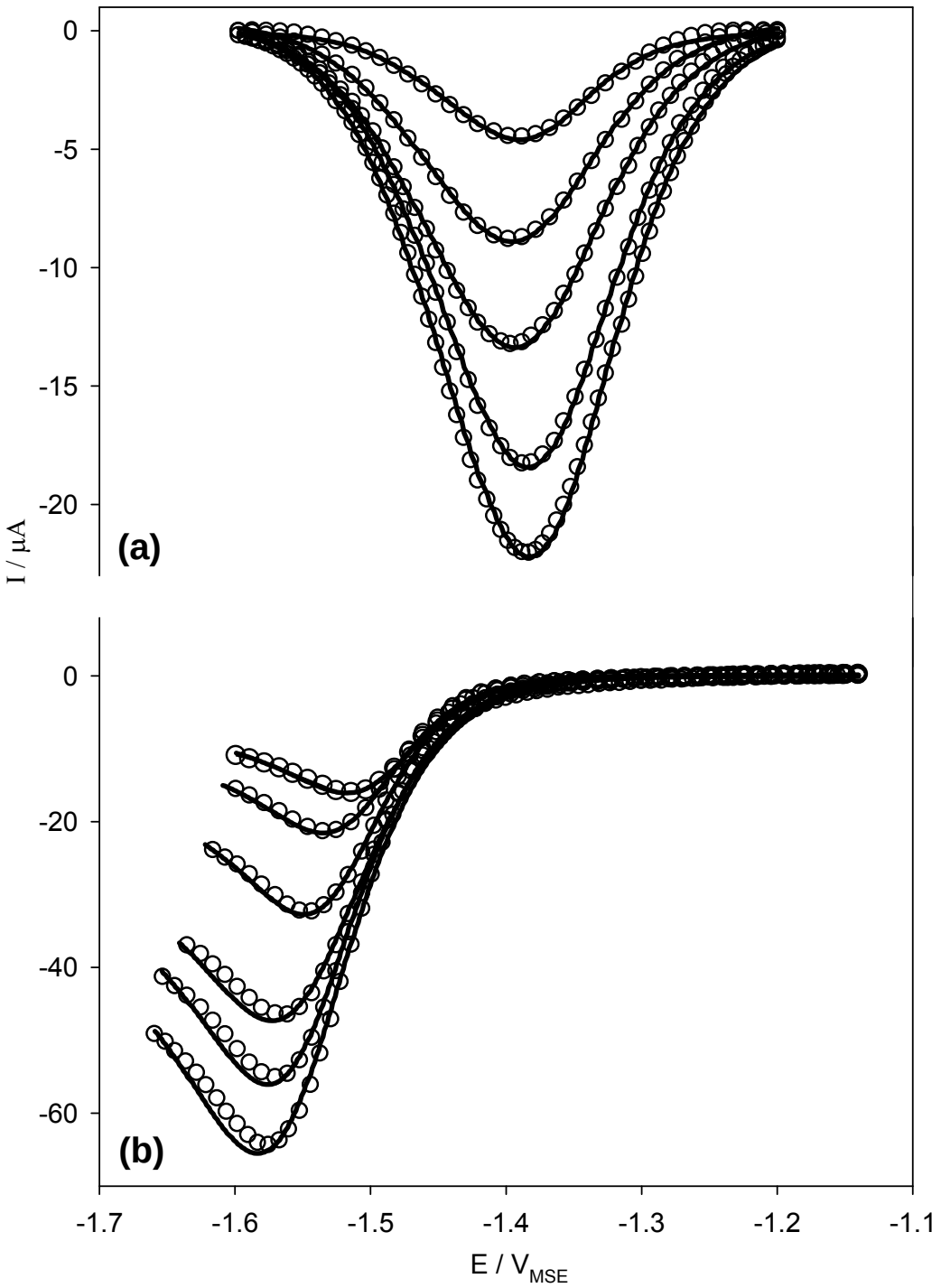

Figure 5.6: (a) Experimental (symbols) and simulated (line) DP voltammograms recorded in 0.1 M $NaClO_4$ containing various NAD^+ concentrations. The concentration increases in the direction of the peak increase as: 0.5, 1, 2, 3, and 4 mM. DPV experimental parameters are the same as those in Fig. 5.5. (b) Experimental (symbol) and simulated (line) LV voltammograms recorded at various scan rates in 0.1 M $NaClO_4$ + 4 mM NAD^+. The scan rate increases in the direction of the peak current increase as: 10, 20, 50, 100 and 200 mV s^{-1}. Temperature, T = 295 K.

The fitting of the LV and DPV curves (Fig. 5.6) also yielded an average value of the αn product, 0.79, which allowed for the calculation of the corresponding apparent transfer coefficient $\alpha = 0.5$ and number of electrons involved in the reaction, $n = 1.58$. These values are in a very good agreement with the experimental values obtained by analyzing the LV and DPV peaks (Table 5.1).

LV and DPV techniques were also utilized to investigate the effect of temperature on the NAD^+ reduction kinetics, *i.e.* to calculate the corresponding activation energy. Fig. 5.7 shows LVs (a) and DPVs (b) obtained at selected temperatures and at a constant NAD^+ concentration in the bulk solution.

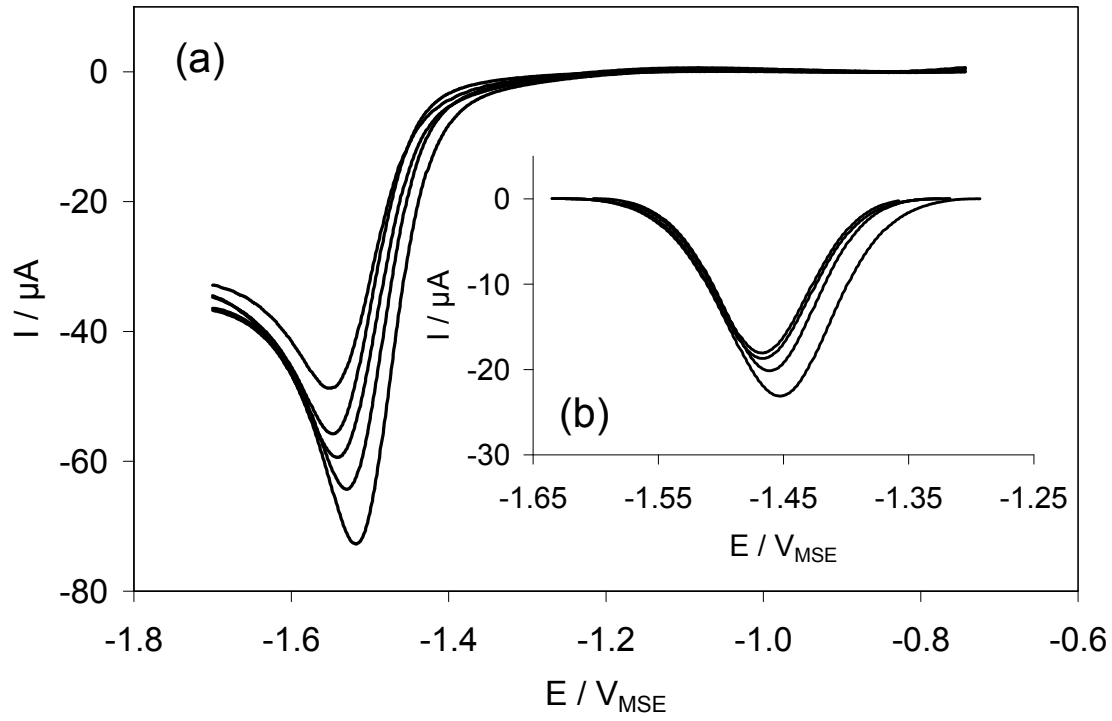

Figure 5.7: (a) LVs of GC electrode in 0.1 M $NaClO_4$ + 4 mM of NAD^+ solution recorded at various temperatures. The temperature increases in the direction of the peak increase as: 295, 304, 310, 315 and 325 K. Scan rate, 100 mV s^{-1}. (b) Differential pulse voltammograms of NAD^+ reduction on GC electrode recorded in 0.1 M $NaClO_4$ + 4 mM of NAD^+. The temperature increases in the direction of the peak increase as: 295, 304, 315 and 325 K. DPV experimental parameters are the same as those in Fig. 5.5.

The peak current increases with the increase in temperature, indicating that the kinetics of NAD^+ reduction also increases. To calculate the corresponding activation energy, a set of LVs and DPVs were recorded at a constant temperature and various NAD^+ concentrations (for example, see Figs. 5.4 and 5.5). Then, the dependence of peak current, I_p, on NAD^+ concentration was analyzed, as in Figs. 5.4 and 5.5. In all cases, a linear dependence was obtained, confirming that the NAD^+ reaction is of pseudo-first order with respect to NAD^+ in the temperature range investigated:

$$I_p = k_{eff}\left[NAD^+\right] \tag{5.6}$$

where k_{eff} is the effective NAD^+ reduction reaction rate constant (A cm^3 mol^{-1}). Given that the NAD^+ reduction reaction is mass-transport controlled and that it also involves adsorption of NAD^+ on the electrode surface and the subsequent electron transfer, the effective reduction reaction rate constant is thus composed of the contributions of mostly the mass-transfer constant, but also the adsorption kinetic constant and the electron transfer rate constant.

Now, the dependence of the effective rate constant on temperature is analyzed in accordance with the Arrhenius law:

$$k_{eff} = A\exp\left(\frac{-\Delta G_{act}}{RT}\right) \tag{5.7}$$

where A is pre-exponential factor (A cm^3 mol^{-1}), ΔG_{act} is the Gibbs energy of activation (kJ mol^{-1}), and the remaining quantities have already been defined previously. Fig. 5.8 shows the resulting behavior.

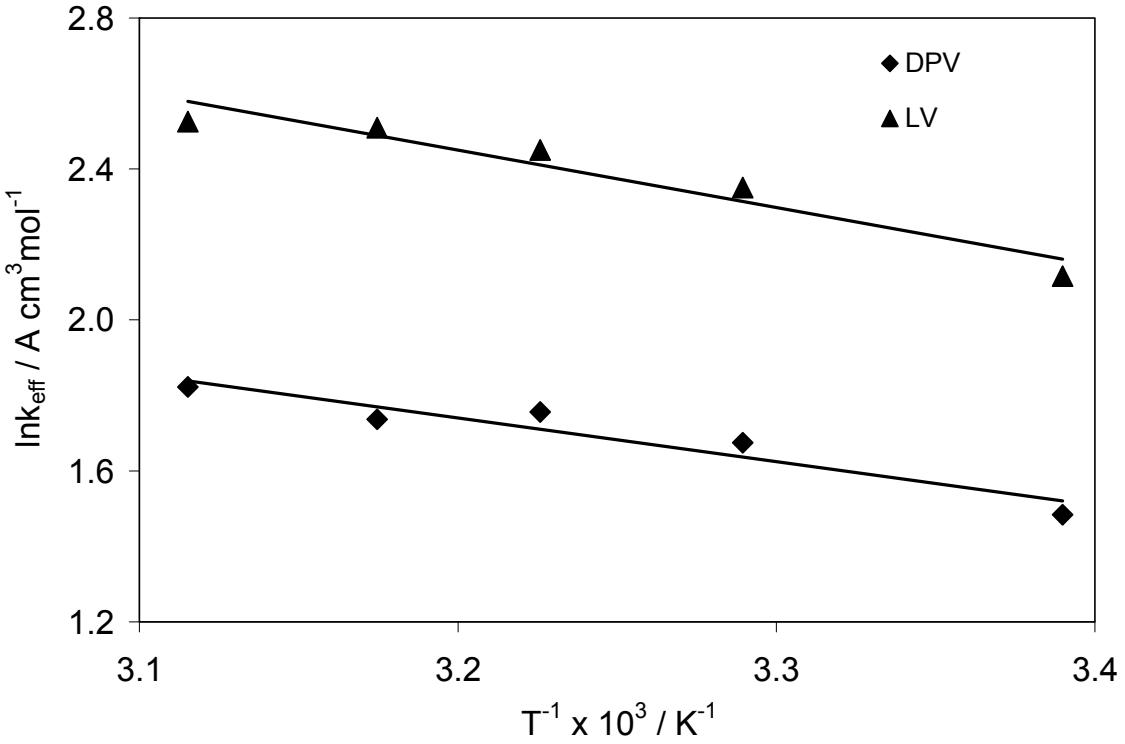

Figure 5.8: Dependence of effective rate constant on temperature obtained from LV and DPV measurements recorded on GC electrode in 0.1 M $NaClO_4$ containing various NAD^+ concentrations. (LV) scan rate, 100 mV s^{-1}. (DPV) modulation time, 70 ms; modulation amplitude, 50 mV; interval time, 0.2 s; step potential, 1.5 mV; scan rate, sr = 7.5 mV s^{-1}.

Fig. 5.8 shows the linear dependence, as expected from the Arrhenius law. From the slope of the lines, apparent Gibbs energy of activation values for the reduction of NAD^+ on the bare GC electrode were calculated for the reaction occurring in the potential region of LV and DPV peaks, $\Delta G_{act,LV}$ = 12.7 kJ mol^{-1} and $\Delta G_{act,DPV}$ = 12.1 kJ mol^{-1} respectively. However, it is more convenient to report ΔG_{act} at a *formal* potential because Gibbs energy of activation is potential dependent according to the following equation [29, 84]:

$$\Delta G_{act} = \Delta G_{act,p} - \alpha n F \eta \tag{5.8}$$

where η represents the overpotential (V). Taking the average value of the αn product (αn = 0.69), the apparent formal Gibbs energy of activation value at formal potential of the NAD^+/NADH redox couple was calculated to be $\Delta G_{act,LV}$ = 53.6 kJ mol^{-1}

(LV measurements) and $\Delta G_{act,DPV} = 53.1$ kJ mol^{-1} (DPV measurements). Therefore, the two different experimental techniques gave values that agree very well, thus confirming their reliability. Similar values were reported in the literature using Ru-GC [24] and Au electrodes [29]. Based on the apparent formal activation energy values obtained, it appears that the reduction of NAD^+ on GC is only a moderately temperature dependent reaction.

5.1.4 Electrochemical impedance spectroscopy

Impedance method delineates the kinetics of the electrode processes. The shape of the impedance diagram tells us about its mechanics [94]. The recently developed methods for analysis of the experimental data enable identification of the choice of adequate structural models of the interface [95]. EIS has grown tremendously over the past few years and is now being widely employed in a variety of scientific fields such as fuel cell testing, biomolecular interaction, and microstructural characterization. EIS may also reveal information about the reaction mechanism of an electrochemical process: different reaction steps will dominate at certain frequencies, and the frequency response as shown by EIS can help identify the rate limiting step. Therefore, EIS was implemented to get more information on the GC electrode/electrolyte interface in the presence of NAD^+. Electrochemical impedance studies were carried out with the same setup which was used also for potentiodynamic polarization studies. The applied *ac* perturbation signal was about ±10 mV within the frequency range 50 kHz to 20 mHz, to ensure complete characterization of the interface and surface processes.

5.1.4.1 Potential-dependent impedance measurements

EIS data of the GC electrode recorded at several potentials in the double-layer and NAD^+ reduction region are presented in Fig. 5.9, in a form of Nyquist plots.

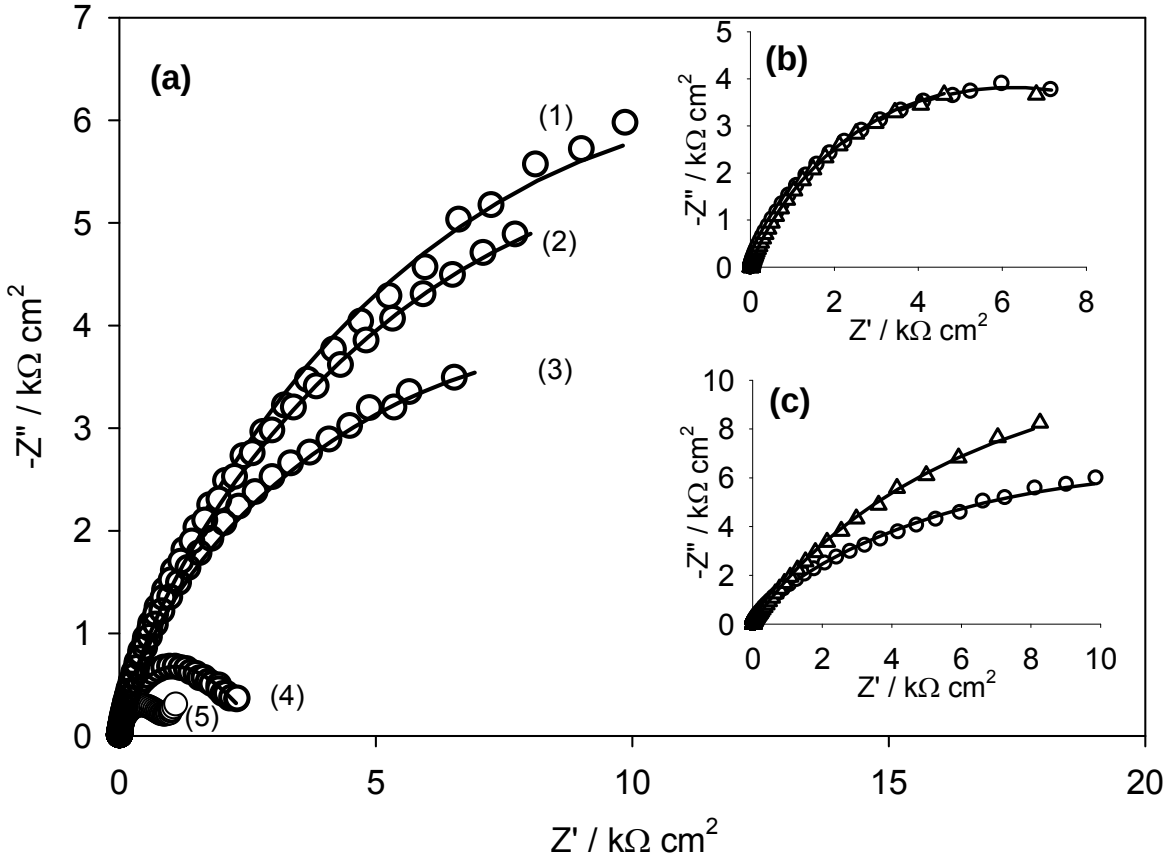

Figure 5.9: (a) Nyquist plot of a GC electrode recorded at various *dc* potentials (1) –1.1 V (2) –1.2 V (3) –1.3 V (4) –1.4 V and (5) –1.45 V in 0.1 M $NaClO_4$ + 4 mM NAD^+. (b) Nyquist plots of a GC electrode at (b) –0.9 V and (c) –1.1 V in (Δ) 0.1 M $NaClO_4$ and (O) 0.1 M $NaClO_4$ + 4 mM NAD^+. The solid lines represent the simulated spectra obtained using the equivalent electrical circuit model presented in Fig. 5.10. Temperature, T = 295 K.

The Nyquist plots in the Fig. 5.9 present a typical shape, with a semicircle in the high-frequency domain characteristic of an interfacial charge-transfer mechanism. As per theory of electrochemical reactions, in *ac* polarization experiments, the diameter of the semi-circle is inversely proportional to the kinetics of an electrochemical reaction [29].

Figs. 5.9b and 5.9c display the response of the GC electrode in the present (circles) and absence (triangles) of NAD^+ in the supporting electrolyte. At –0.9 V (Fig. 5.9b), which is in the potential region more positive of the NAD^+ reduction peak in

Fig. 5.1, the two spectra overlap, confirming that no NAD^+ reduction occurs at this potential. However, at –1.1 V (Fig. 5.9c) the spectrum recorded in the presence of NAD^+ (circles) displays a smaller-diameter quarter-circle than that in the absence of NAD^+ (triangles), indicating the occurrence of the NAD^+ reduction reaction. If we compare this to the results obtained using LV and DPV, we can see that the onset of NAD^+ reduction in these *dc* measurements can be noticed only at potentials negative of ca. –1.25 V. This confirms that EIS is more a sensitive technique for the detection of reactions kinetics than the two *dc* techniques.

Further, if the electrode potential is biased to values negative of –1.1 V, the diameter of the EIS semicircle further decreases (Fig. 5.9a), indicating an increase in the NAD^+ reduction kinetics. This is in accordance with the results obtained by LV and DPV measurements.

To quantify the EIS results, the experimental spectra in Fig. 5.9 were modeled using non-linear least-squares fit analysis (NLLS) software [96] and an electrical equivalent circuit (EEC) presented in Fig. 5.10. The modeled data are presented as solid lines in Fig. 5.9. It is evident that the agreement between the experimental data (symbols) and modeled data (lines) is very good, confirming the validity of the proposed EEC in describing the impedance behavior of the investigated system under the given experimental conditions. The EEC parameter values are listed in Tables C.1 and C.2 in Appendix C.

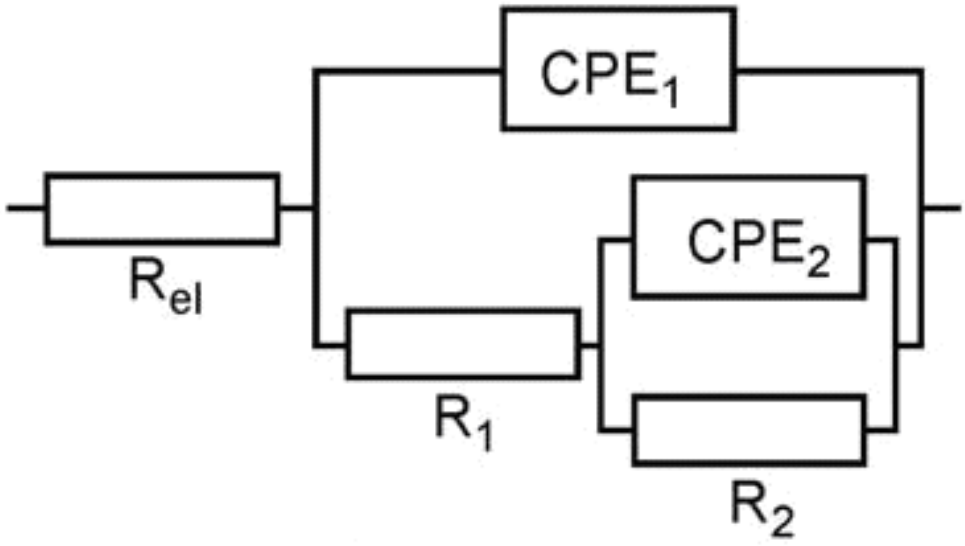

Figure 5.10: Electrical equivalent circuit used to model the EIS data.

The proposed EEC model is comprised of two time constants; the high-frequency (HF) time constant, τ_1 (τ_1=CPE$_1$$R_1$), and the low frequency (LF) time constant, τ_2 (τ_2=CPE$_2$$R_2$). This circuit models a response where polarization is due to a combination of kinetic and diffusion processes. Here R (Ω) stands for resistance and CPE (Ω^{-1} s^n) for *constant phase element*. The following equation represents impedance, Z (Ω) of CPE:

$$Z_{CPE} = \frac{1}{CPE(j\omega)^n} \tag{5.9}$$

where ω (rad s^{-1}) represents the radial frequency. If n = 1, Z_{CPE} behaves as a perfect capacitance. If n = 0, it has characteristics of a perfect resistance and if n = 0.5 it acts like a Warburg, (mass transport) impedance [97]. Values of n other than the ideal values mentioned above indicate the presence of inhomogeneties such as surface roughness, adsorbed species at the microscopic level of the oxide/electrolyte interface [98, 99].

The modeling of the EIS spectra in Fig. 5.9 resulted in a value of the constant-phase element (CPE_1) exponent $n_1 = 0.87 \pm 0.02$. Hence, CPE_1 represents a response of a capacitor, in this case a response of the electrochemical double-layer capacitance. The corresponding parallel resistance R_1 is the charge transfer resistance or polarization resistance.

The second EEC branch (Fig. 5.10) is composed of CPE_2 and R_2. CPE_2 is located in the LF domain of the spectrum, and the fitting of the spectra in Fig. 5.9 gave a mean value of its exponent $n_2 = 0.52 \pm 0.03$. As this value is close to 0.5, it indicates a response of a diffusion-controlled process. Hence this capacitance is related to the diffusive pseudo-capacitance (or Warburg impedance, W) and R_2 is the corresponding resistance to mass transfer. Besides the diffusive response related to mass transport of NAD^+ towards the electrode surface, traces of phenolic and carboxylic functional groups commonly found at the GC surface could also contribute to diffusive capacitance [100]. Further, in Fig. 5.10, R_{el} represents the electrolyte resistance between the working and reference electrode.

In the EEC in Fig. 5.10, the sum of charge transfer resistance (R_1) and mass-transport resistance (R_2) represents the total resistance (R_T) related to the kinetics of the parallel NAD^+ reduction and hydrogen evolution reaction. Its inverse value, R_T^{-1}, could thus be related to the total *dc* current measured under the potentiostatic conditions, $1/I$ [29]. The dependence of R_T^{-1} on the applied *dc* potential obtained from the EIS data recorded in the supporting electrolyte (triangles) and NAD^+-containing solution (circles) is shown in Fig. 5.11a.

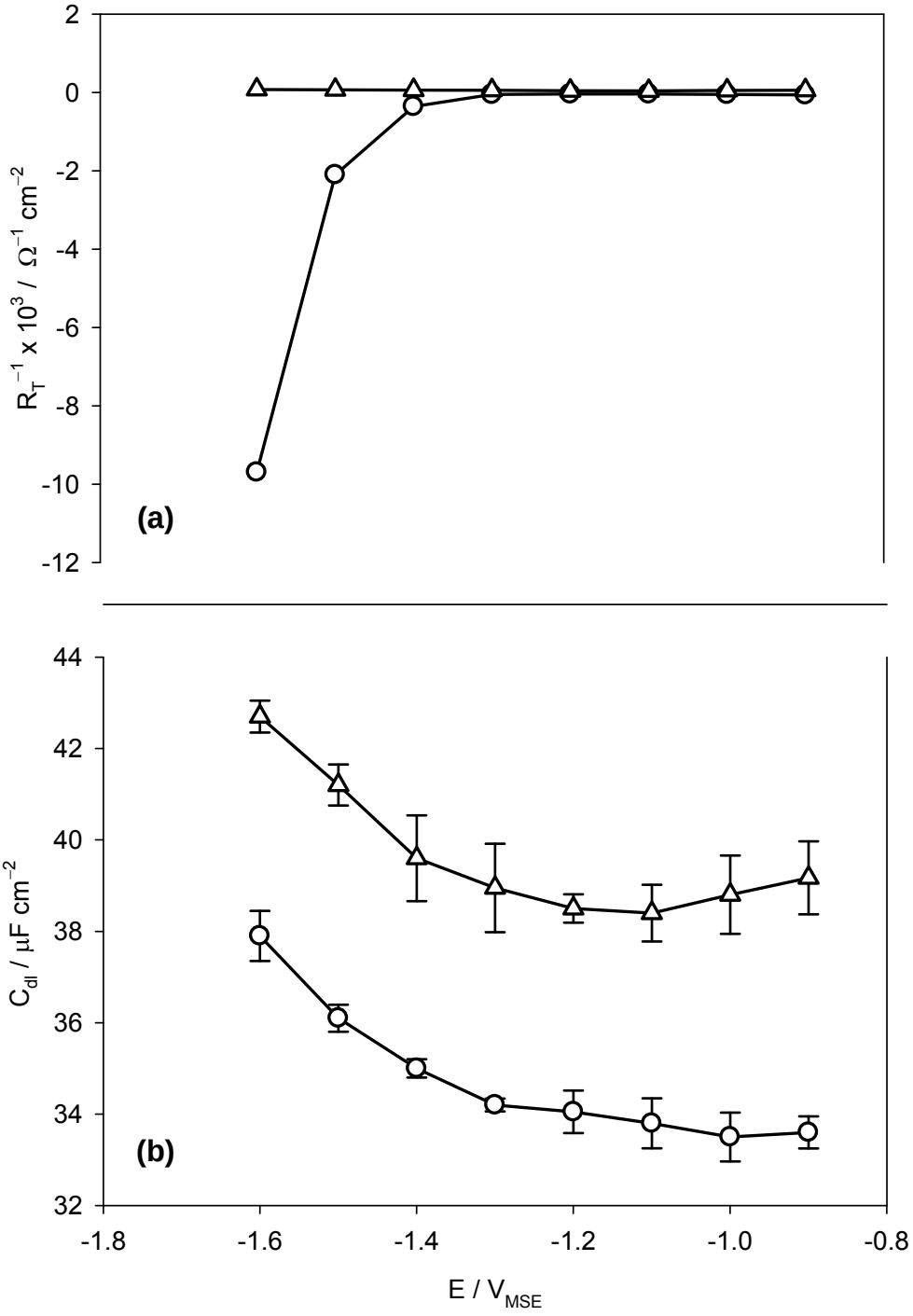

Figure 5.11: Dependence of the (a) inverse of total resistance and (b) double-layer capacitance on the applied *dc* potential obtained by fitting the EIS spectra in Fig. 5.9a. (Δ) 0.1 M $NaClO_4$ and (O) 0.1 M $NaClO_4$ + 4 mM NAD^+. In (a) negative sign of the ordinate is used only to emphasize the cathodic character of NAD^+ reduction reaction. Error bars in Fig. 5.11a are not visible since the largest error is 0.015×10^{-3} $\Omega^{-1}cm^{-2}$.

The data obtained in the absence of NAD^+ in the supporting electrolyte (triangles) is relatively constant, while in the presence of NAD^+ (circles) the $1/R_T$ value starts increasing at potentials negative of –1.2 V, which is due to the reduction of NAD^+ on the electrode surface (note that the EIS spectra in Fig. 5.9c shows that NAD^+ is being reduced already at –1.1 V, but the large scale of the ordinate in Fig. 5.11 prevents the visual distinction between the two responses at potentials positive of –1.2 V). In conclusion, the NAD^+ reduction EIS data (Fig. 5.11) is in agreement with the LV data (Fig. 5.1), thus validating the NAD^+ reduction behavior recorded and the experimental approaches used in investigating the kinetics of NAD^+ reduction on the GC electrode, under the experimental conditions applied.

It has already been shown that the NAD^+ reduction reaction might involve adsorption of either NAD^+ or the corresponding reduction reaction products, NADH and/or NAD_2, on the electrode surface [29] (this will also be investigated in more detail later in the thesis, Section 5.2). Thus, if the electrode surface gets covered by an adsorbed molecular (sub)layer formed during the NAD^+ reduction reaction, and if this layer is stable on the electrode surface, the EIS spectra should detect such a response. More particularly, if there is a blockage of the electrode surface by adsorbents that have a lower dielectric constant than water, then there should be a decrease in the electrochemical double-layer capacitance, according to the electrochemical double-layer theory [101]. To investigate this, the behavior of the electrochemical double-layer capacitance (CPE_1) obtained in EIS experiments presented in Fig. 5.9 was further analyzed. A true value of the double-layer capacitance was calculated using the equation proposed by Brug *et al.* [102]:

$$C_{dl} = [CPE_1(R_{el}^{-1} + R_1^{-1})^{n_1 - 1}]^{-n_1} \tag{5.10}$$

The results are plotted in Fig. 5.11b. The plot shows the potential-dependent behavior of the double-layer capacitance in the absence (triangles) and presence (circles) of NAD^+ in the solution. The double-layer capacitance of the NAD^+-containing solution is lower than that obtained in the absence of NAD^+, in the whole potential region studied. This confirms that NAD^+ indeed adsorbs on the GC surface in the potential region presented in the Fig. 5.11b, and this region covers both the region where NAD^+ is not

reduced (positive of –1.1 V, *i.e.* the electrochemical double-layer region) and the region where NAD^+ undergoes reduction (negative of –1.1 V). However, one cannot exclude a possible adsorption of NAD_2 and NADH formed in the NAD^+ reduction reaction at potentials negative of –1.1 V.

5.1.4.2 Concentration-dependent impedance measurements

Concentration-dependent EIS behavior was also studied in the potential region of NAD^+ reduction, and selected spectra are shown in Fig. 5.12.

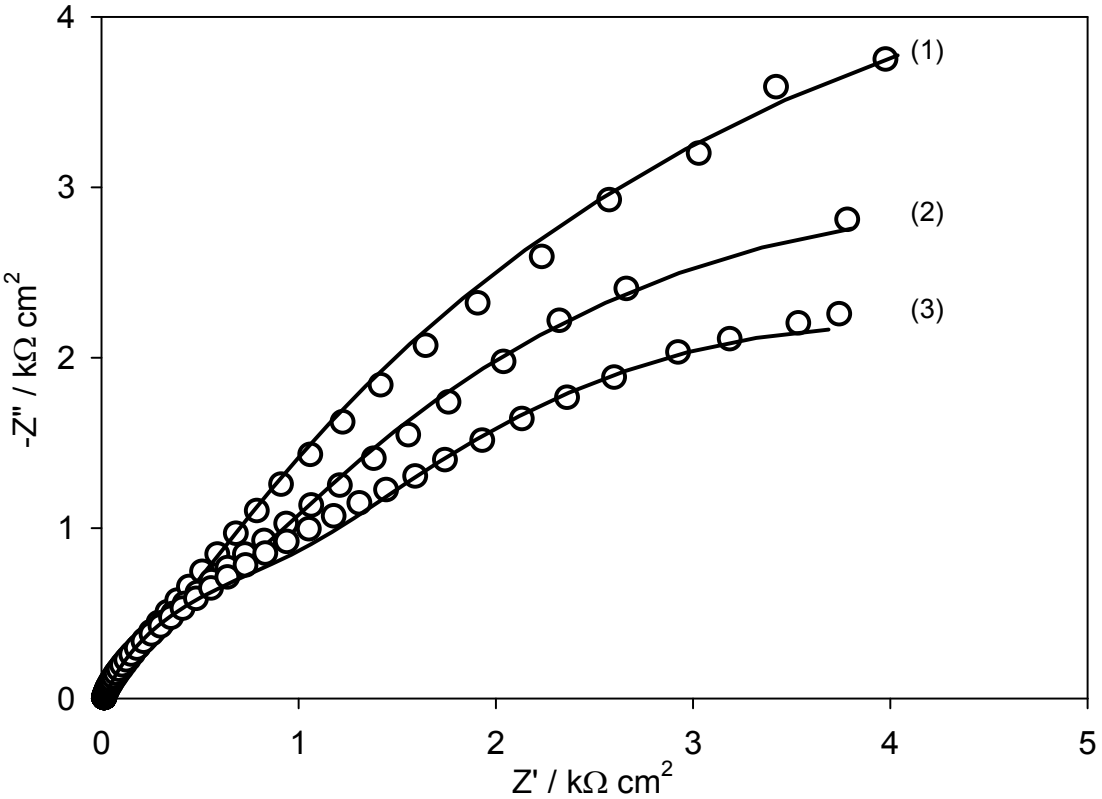

Figure 5.12: Nyquist plot of a GC electrode recorded at various concentrations of NAD^+ in 0.1 M $NaClO_4$: (1) 0.5 mM, (2) 2 mM, and (3) 3 mM. Applied *dc* potential, E_{dc} = -1.5 V_{MSE}; temperature, T = 295 K.

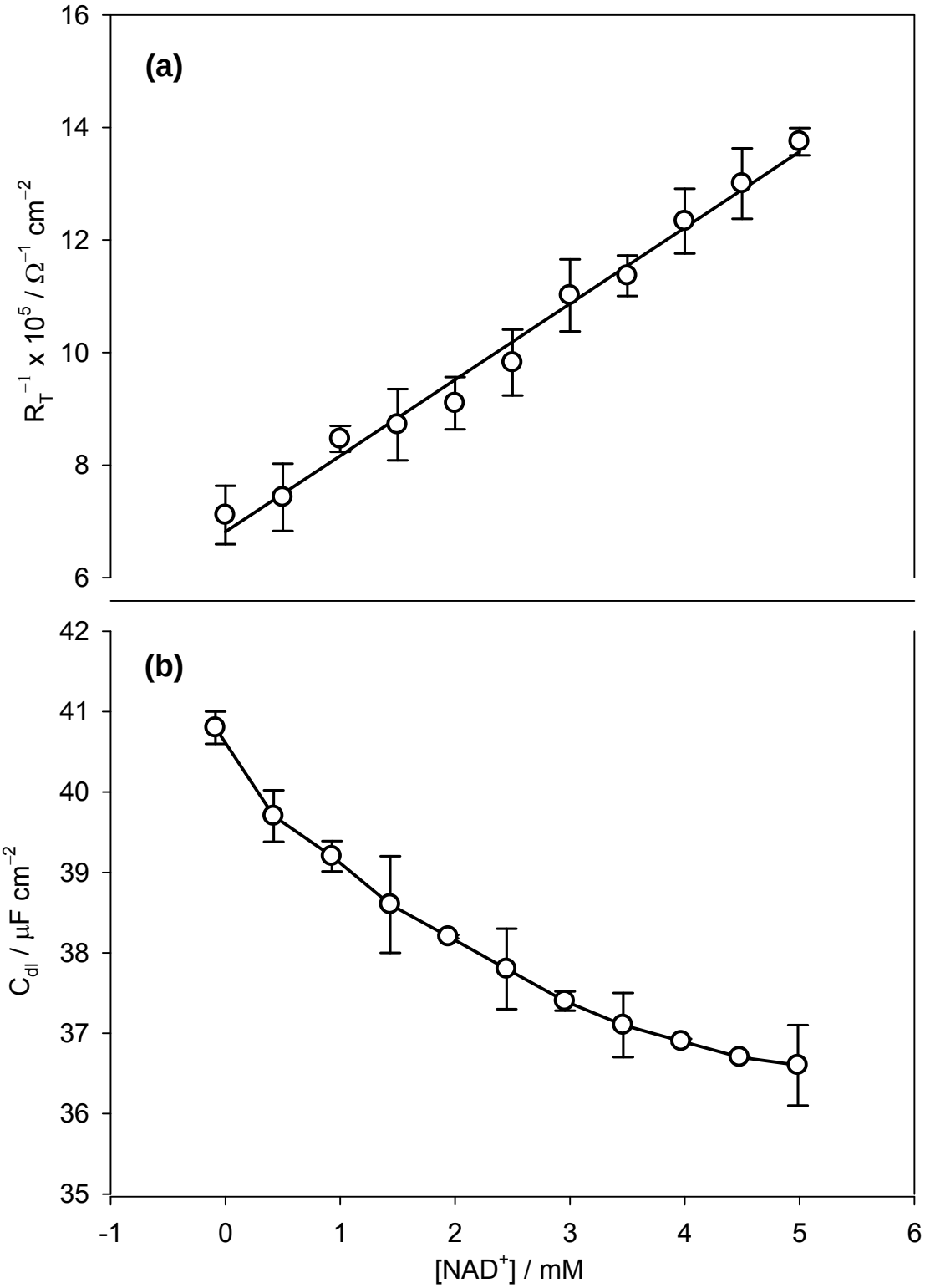

Figure 5.13: Dependence of the (a) inverse of total resistance and (b) double-layer capacitance on the NAD^+ concentration obtained by fitting the EIS spectra in Fig. 5.12.

The spectra in Fig. 5.12 clearly show the appearance of two semicircles confirming the presence of two time constants, namely the high-frequency (HF) time constant, τ_1, and the low frequency (LF) time constant, τ_2 (Fig. 5.9), which could be explained in the same manner as those in the previous section of the thesis (Section 5.1.4.1). As the concentration of NAD^+ in solution increases, the total resistance (R_T) to the NAD^+ reduction reaction decreases, while the corresponding inverse value, R_T^{-1}, increases linearly, as shown in Fig. 5.13a.

Knowing that current is proportional to inverse resistance ($I \alpha R^{-1}$); the linear trend in Fig. 5.13a indicates that the NAD^+ reduction reaction is of pseudo-first order with respect to NAD^+. Although the EIS measurements in Fig. 5.13 were preformed potentiostatically, the trend is very similar to that obtained from linear polarization measurements presented in Fig. 5.4a, *i.e.* in both cases the reaction was found to be of pseudo-first order with respect to NAD^+.

Further, it would also be of interest to examine the behavior of the electrochemical double-layer capacitor, CPE_1 (*i.e.* C_{dl}) with NAD^+ concentration. For this purpose, C_{dl} values were calculated at each NAD^+ concentration using Eq. (5.10), and the resulting values are presented in Fig. 5.13b. The trend in the Fig. 5.13b demonstrates that with an increase in NAD^+ concentration in the bulk solution, the double-layer capacitance decreases. This indicates that the electrode surface coverage by adsorbed NAD^+ (and/or NADH and/or NAD_2) increases with NAD^+ concentration in the bulk solution, displaying an adsorption-type behavior. In fact, if the inverse of the values in Fig. 5.13b is plotted, the obtained trend would be very similar to that of a classical adsorption isotherm (Fig. 5.14).

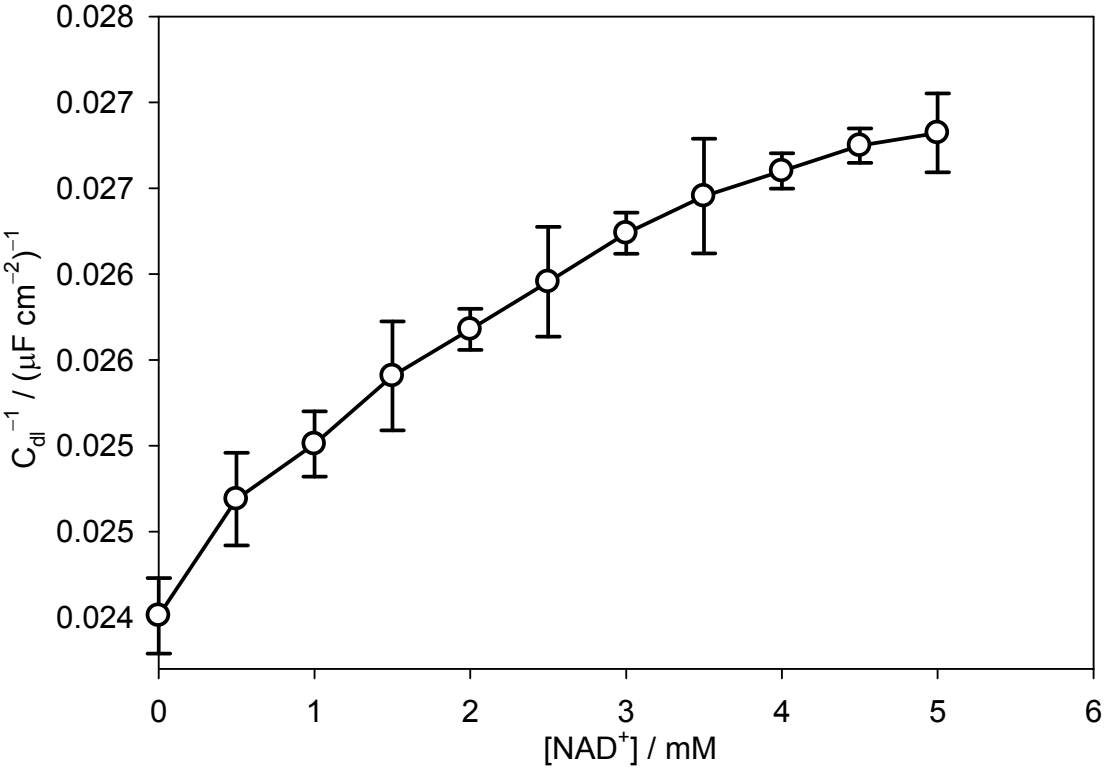

Figure 5.14: Inverse of double-layer capacitance on the NAD^+ concentration obtained by fitting the EIS spectra in Fig. 5.12.

In conclusion, LV, DPV and EIS measurements were used to evaluate the kinetics of NAD^+ reduction reaction on a GC electrode. A very good agreement among results produced by the three techniques was demonstrated. It was found that that under the experimental conditions employed, the NAD^+ reduction reaction is under diffusion control, is irreversible (requires overpotential of more than -550 mV), and is of pseudo-first order with respect to NAD^+. The kinetics of reduction of NAD^+ on GC at a *formal* potential of the NAD^+/NADH couple (-0.885 V) was found to be rather slow, and only moderately temperature dependent.

5.2 Adsorption of NAD^+ on a GC electrode surface

In Section (5.1), the kinetics of NAD^+ reduction on a GC electrode surface was discussed. It was concluded that the NAD^+ reduction reaction is irreversible within the potential region of interest, it occurs at high overpotential, and it is under mass-transport control. As already mentioned in the Chapter 2, the 1,4-NADH regeneration reaction is a heterogeneous reaction, involving several basic steps: mass-transport of NAD^+ from the bulk solution to the electrode surface, adsorption of NAD^+ to the electrode surface, its reduction (Scheme 1), and finally the desorption of the products (NADH, NAD_2) from the electrode surface and their mass transport into the bulk electrolyte.

Since the NAD^+ reduction process is a heterogeneous electrocatalytic reaction, it is very important to obtain information on the adsorptive interaction of NAD^+ with an electrode surface. However, the corresponding literature information is scarce [31, 32, 40, 52, 54, 112, 56, 34, 111, 113-117, 116, 118]. Therefore, this PhD project also focused on the investigation of adsorption of NAD^+ on a GC electrode surface to build the fundamental knowledge required for the design of better 1,4-NADH regeneration electrodes. These results were obtained using differential capacitance (DC) and ATR-FTIR techniques. The focus of the research was to investigate the influence of electrode potential on the kinetics and thermodynamics of NAD^+ adsorption on GC.

In order to avoid the influence of NAD^+ reduction kinetics (electron transfer) on the NAD^+ adsorption step, it was first necessary to determine the electrochemical double-layer (DL) region of the GC electrode in the NAD^+-containing solution. For this purpose, linear polarization voltammograms were recorded in the absence (control) and presence of NAD^+ in the electrolyte, Fig. 5.15. Although the plot looks similar to that one previously shown (e.g. Fig. 5.1), it should be noted that the anodic limit was significantly extended to positive potentials, 0.6 V.

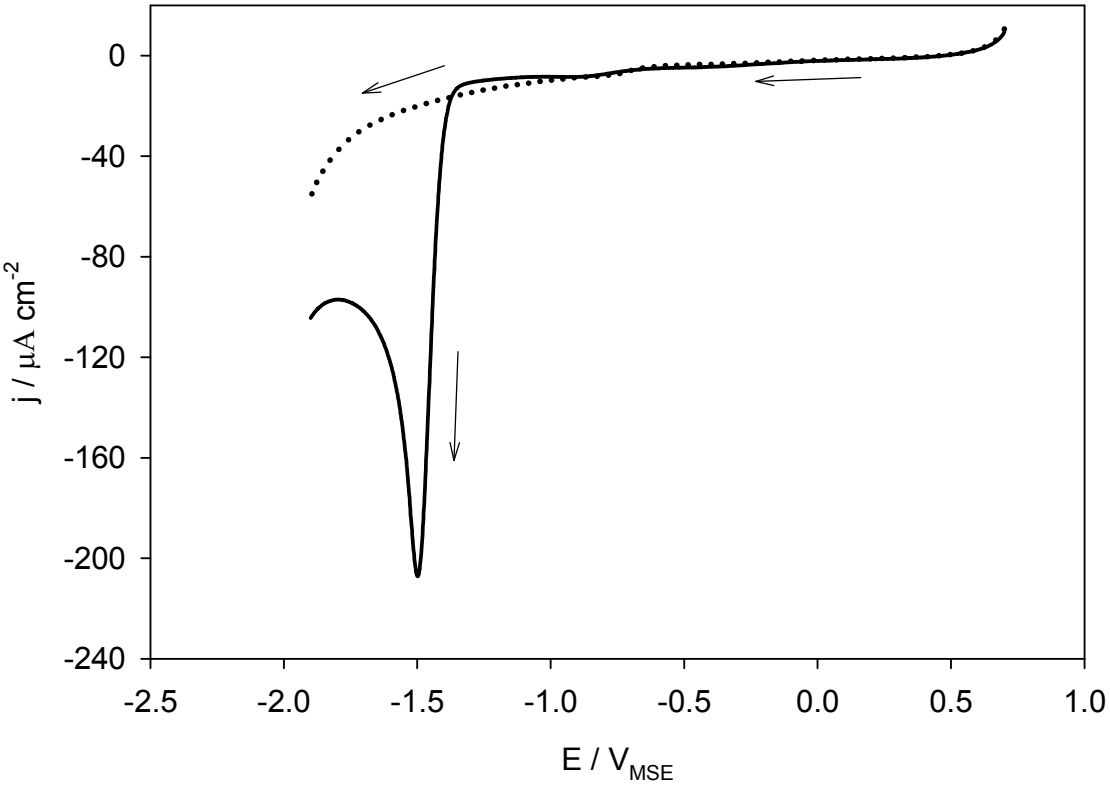

Figure 5.15: Linear polarization voltammograms of a GC electrode recorded in the supporting electrolyte (dotted line) and supporting electrolyte containing 4 mM NAD^+ (solid line). Scan rate, sr = 100 mV s^{-1}. Temperature, T = 295 K.

The trend of the curves can be explained in the same way as the trend in Fig. 5.1, and will thus not be presented here in detail. Briefly; the plot in Fig. 5.15 can be divided into two major potential regions. The region negative of ca. –1.3 V is the NAD^+ reduction reaction region, as evidenced by the well-pronounced NAD^+ reduction peak at –1.5 V. Since NAD^+ reduction involves electron transfer, this potential region is not convenient for studying the interactive adsorption behavior of NAD^+. However, Fig. 5.15 shows that positive of –1.3 V, the two LVs overlap, and that there is no evidence of any redox reaction occurring on the GC surface. Therefore, this potential region is suitable for investigating the adsorption of NAD^+ on the GC surface since adsorption measurements are influenced by electron-transfer reactions. The electrode is ideal "polarizable" in this potential region, which is commonly called "the electrochemical double-layer (DL)

region" of the GC electrode. Thus, adsorption measurements preformed in this PhD project were made within this DL region, at electrode potentials of 0.5, 0.05 and –0.8 V. These potentials correspond to the GC surface that is respectively, positively charge, neutral, and negatively charge. Hence, the study allowed us to investigate the influence of surface charge on the interactive behavior of NAD^+ with the GC electrode surface.

First, results on the thermodynamic NAD^+ behavior will be presented (*i.e.* equilibrium adsorption results), followed by results on the kinetics of NAD^+ adsorption.

5.2.1 NAD^+ Adsorption Thermodynamics

In order to investigate the adsorption of NAD^+ on a GC electrode surface under equilibrium conditions, differential capacitance measurements were carried out at different concentrations of NAD^+ in the bulk electrolyte (0.1 M $NaClO_4$). Fig. 5.16 shows a set of selected differential capacitance curves recorded at a potential of 0.05 V. It was expected that if NAD^+ adsorbed on the GC electrode surface, the capacitance would decrease due to the blockage of electrode surface by adsorbed NAD^+ molecules. This is in accordance with the electrochemical double-layer theory. Namely, NAD^+ (and most of organic molecules) has a significantly lower relative permittivity than water (ca. 2-3 vs. 80, respectively). Hence, by replacing water molecules at the electrode/electrolyte interface during adsorption, the double-layer capacitance decreases.

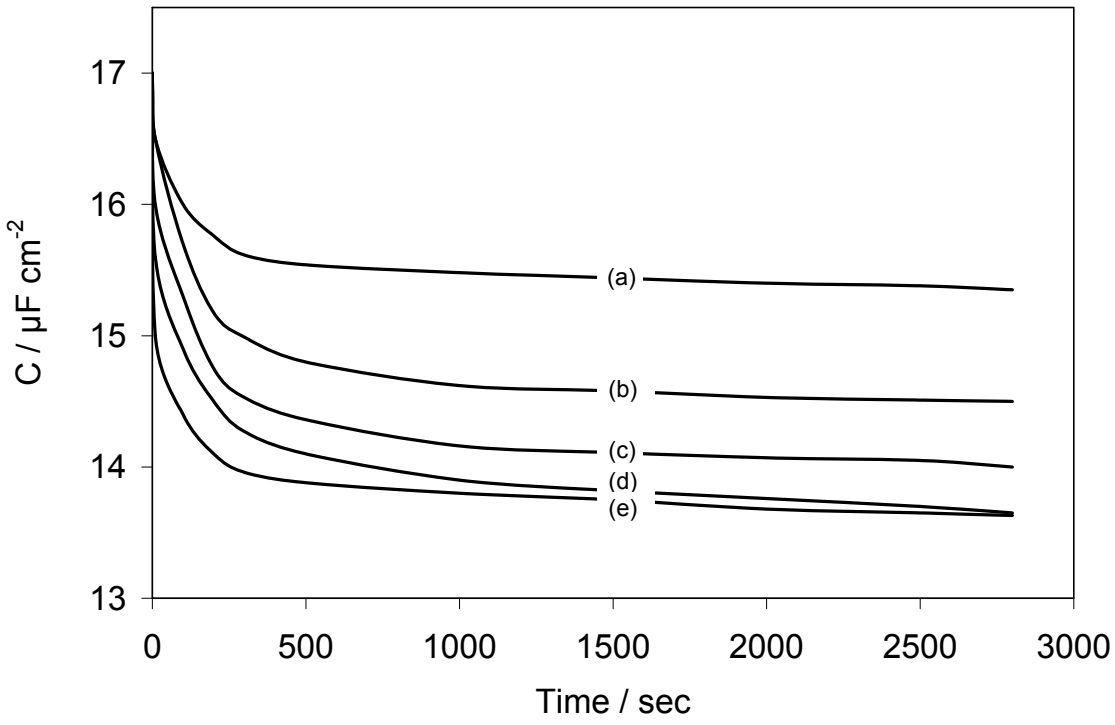

Figure 5.16: Differential capacitance curves of a GC electrode recorded at 0.05 V in 0.1 M $NaClO_4$ containing selected concentrations of NAD^+ (a) 0.01, (b) 0.1, (c) 0.3, (d) 1, and (e) 3 mM. Frequency f = 25 Hz; and *ac* amplitude = ± 5 mV. Temperature, T = 295 K.

Fig. 5.16 clearly demonstrates that the addition of NAD^+ in the supporting electrolyte indeed results in a decrease in differential capacitance, as the result of adsorption of NAD^+ on the GC surface. The differential capacitance reaches a quasi-constant (plateau) value at longer times evidencing the attainment of quasi-equilibrium. In addition, with an increase in NAD^+ bulk solution concentration, the values of the differential capacitance at the plateau decrease, indicating an increase in surface concentration (or surface coverage) of NAD^+ (Fig. 5.16, curves b-e). Thus, these measurements directly confirmed that NAD^+ indeed adsorbs on the GC electrode surface at the electrode potential studied.

From DC measurements in Fig. 5.16, the apparent GC electrode surface coverage by NAD^+ was calculated [103]:

$$\theta_i = \frac{C_{DL}^{o} - C_{DL}^{i}}{C_{DL}^{o} - C_{DL}^{\min}} \tag{5.11}$$

where θ_i is the apparent NAD^+ surface coverage, C_{DL}^{o} (F cm^{-2}) is the electrochemical double-layer capacitance in a NAD^+-free solution, C_{DL}^{i} is the electrochemical double-layer capacitance at a specific equilibrium concentration of NAD^+ in the bulk solution, $C_{DL}^{\min}$ is the electrochemical double-layer capacitance at a maximum (saturated) NAD^+ surface converge. Fig. 5.17a shows the corresponding dependence of the NAD^+ surface coverage at 0.05 V obtained from *ac* voltammograms in Fig. 5.16 using Eq. (5.11).

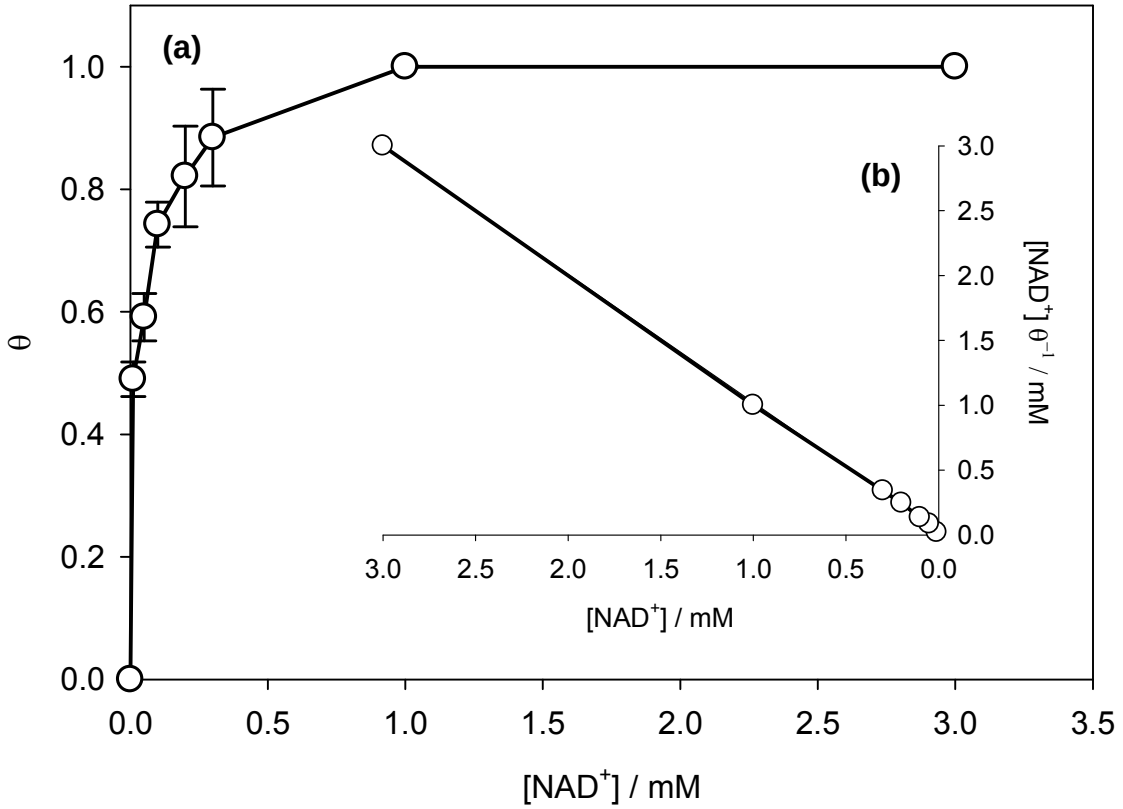

Figure 5.17: (a) Dependence of NAD^+ surface coverage on NAD^+ bulk solution concentration. The data were obtained from *ac* voltammograms recorded in 0.1 M $NaClO_4$ containing various concentrations of NAD^+ (Fig. 5.16), and at electrode potential 0.05 V. (b) The data from plot (a) presented in a form of a linearized Langmuir adsorption isotherm. Symbols represent experimental data while the line represents the Langmuir isotherm model. Temperature, T = 295 K.

The trend in Fig. 5.17a demonstrate that the NAD^+ surface coverage rapidly increases with an increase in bulk NAD^+ concentration and then reaches a plateau at a NAD^+ concentration of 1 mM. The latter indicates fully saturated NAD^+ coverage on GC electrode surface. In order to easier compare the influence of electrode potential on the NAD^+ adsorption equilibrium, the NAD^+ adsorption data are presented together in Fig. 5.18 for all three electrode potentials studied. It should be noted that an assumption was made that the saturated (100%) surface coverage by NAD^+ was reached at each potential, according to Eq. (5.11).

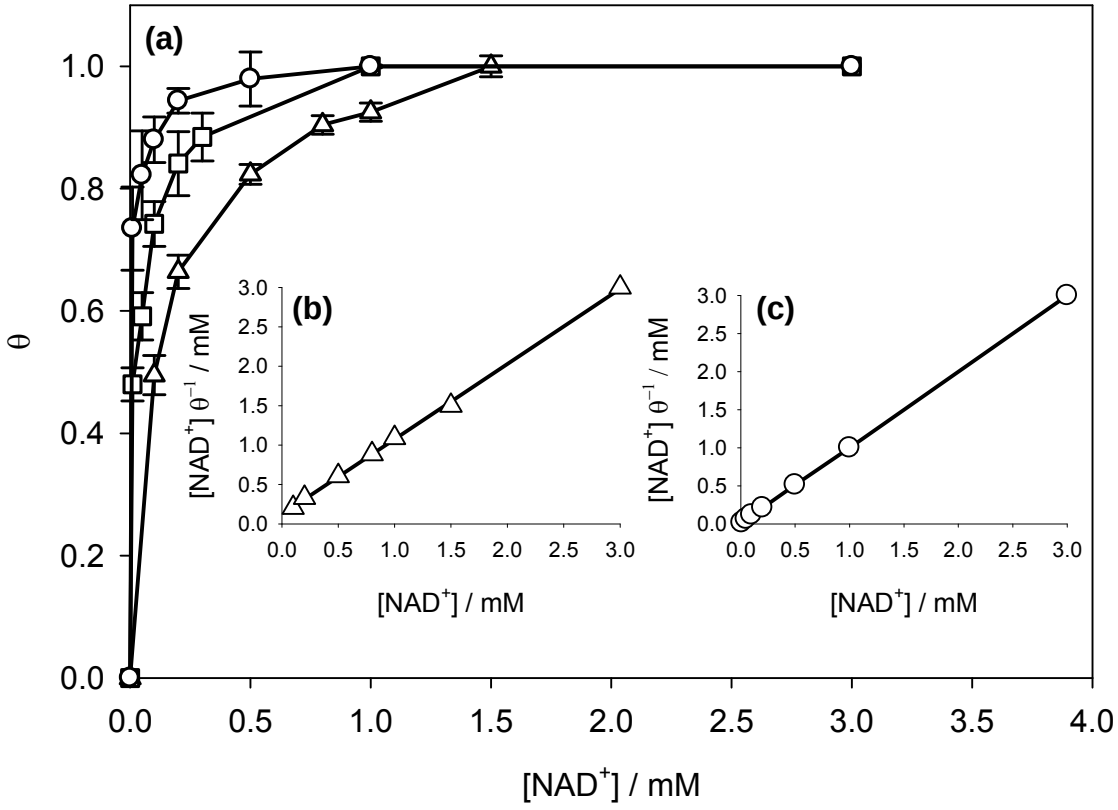

Figure 5.18: (a) Dependence of NAD^+ surface coverage on NAD^+ bulk solution concentration. The data were obtained from *ac* voltammograms recorded in 0.1 M $NaClO_4$ containing various concentrations of NAD^+, and at electrode potentials of (O) 0.5 V, (□) 0.05 V, and (Δ) –0.8 V. (b) and (c) The data from plot (a) for (b, Δ) –0.8 V and (c, O) 0.5 V presented in a form of a linearized Langmuir adsorption isotherm. Symbols represent experimental data while the line represents the Langmuir isotherm model. Temperature, T = 295 K.

Fig. 5.18a demonstrates that as the electrode becomes more positive, the adsorption plateau is reached "faster", *i.e.* at relatively lower NAD^+ concentration in the bulk solution. This indicates that the adsorption process is possibly driven by electrostatic interactions between the NAD^+ molecule and the GC electrode surface. The total charge of the NAD^+ molecule in aqueous solutions at pH of the adsorption experiments (5.8) is negative [45, 46]. Thus, when the electrode is positively charged, the adsorptive interactions of the negatively-charged NAD^+ molecule with the positive electrode surface are stronger, as indeed evidenced in Fig. 5.18. However, the question that might be asked is "Why then the negatively-charged NAD^+ molecule adsorbs on the negatively-charged GC electrode surface (at –0.8 V)?" One should bear in mind that the adsorption of organic molecules on solid surfaces in an aqueous environment is governed by a range of different interactions, including not only the electrostatic interactions, but also entropy and enthalpy change, van der Waals forces, hydrogen bonding, etc. In the case of adsorption of NAD^+ at –0.8 V, despite the same charge of the molecule and the electrode substrate, the result demonstrate that one or more of the other factors outlined above contributes to the driving force for adsorption. In aqueous solutions, this usually represents an increase in entropy of the system, due to the replacement of water molecules in the double-layer region (by the adsorbent) and due to conformational changes of the adsorbent [103-105].

In order to obtain thermodynamic data on the NAD^+ adsorption at different electrode potentials, the adsorption process was modeled by a suitable adsorption isotherm. Although the adsorption curves in Figs 5.17 and 5.18 display a typical Langmurian-type shape, several other isotherms were also tested. However, the Langmuir isotherm gave the best agreement between the experimental and modeled data [103, 104, 106, 107]:

$$\theta_i = \frac{B_{ads}[NAD^+]}{1 + B_{ads}[NAD^+]} \tag{5.12a}$$

or in a linearized form:

$$\frac{[NAD^+]}{\theta} = \frac{1}{B_{ads}} + [NAD^+] \tag{5.12b}$$

where B_{ads} is known as the adsorption affinity constant ($dm^3\ mol^{-1}$), which is related to the affinity of NAD^+ molecule towards surface adsorption sites at constant temperature. Thus, if the Langmuir isotherm represents the thermodynamic description of the adsorption process, in this case that of NAD^+, a plot of $[NAD^+]\times\theta^{-1}$ versus $[NAD^+]$ should yield a straight line of a slope equal to unity, and intercept B_{ads}^{-1}. Indeed, Figs. 5.17b, 5.18b and 5.18c demonstrate a linear trend (an average correlation coefficient for the three plots, $R^2 = 0.9997 \pm 0.0001$). In addition, the slope of the lines is very close to one (an average slope for the three plots is 0.985 ± 0.007), which agrees with Eq. (5.12b). The corresponding adsorption affinity constant values are listed in Table 5.2.

Apparent Gibbs free energy values (ΔG_{ads}) of adsorption of NAD^+ on the GC electrode surface were further calculated at the three electrode potentials [103, 104, 106, 107]:

$$B_{ads} = \frac{1}{[solvent]} \exp\left(\frac{-\Delta G_{ads}}{RT}\right) \tag{5.13}$$

where R ($J\ mol^{-1}\ K^{-1}$) is the gas constant, T (K) is the temperature, and [*solvent*] is the molar concentration of the solvent, which in this case is water ($[H_2O] = 55.5\ mol\ dm^{-3}$). The corresponding apparent Gibbs free energy of adsorption values calculated at the three different potentials are presented in Table 5.2.

Table 5.2: Adsorption affinity constant and apparent Gibbs free energy of adsorption of NAD^+ on a GC electrode surface at various electrode potentials.

E / V	$B_{ads} \times 10^{-3}$ / $dm^3\ mol^{-1}$	ΔG / $kJ\ mol^{-1}$
–0.80	10.35	–32.80±0.25
0.05	31.45	–35.61±0.86
0.50	83.33	–38.02±0.40

Analysis of the data in the Table 5.2 shows that the adsorption affinity constant, and thus also the apparent Gibbs free energy of NAD^+ adsorption, is highly surface-charge dependent. Namely, by polarizing the electrode to more positive (anodic) potentials the value of adsorption affinity constant increases, indicating an increase in tendency of NAD^+ to adsorb on the more positive surface. The origin of this behavior was already discussed in relation to Fig. 5.18, and is related to the electrostatic interactions between NAD^+ and the GC electrode surface.

The values of apparent Gibbs free energy of adsorption in Table 5.2 evidence spontaneous and relatively strong adsorption of NAD^+ on the GC electrode surface, *i.e.* that the equilibrium for the adsorption process lies well in favor of adsorption of NAD^+ on the GC surface. Close values were previously obtained in our laboratory for the adsorption of NAD^+ on a gold surface (– 43 kJ $mol^{-1}$and –39 kJ mol^{-1}on a positively and negatively charged surface, respectively) [103]. Takamura *et al.* [33] reported a close value, –31 kJ mol^{-1}, but for the adsorption of nicotinamide (NA) on gold.

In conclusion, equilibrium adsorption measurements confirm that NAD^+ spontaneously and strongly adsorbs on the GC electrode surface, and that the adsorption process (from the thermodynamic point of view) is surface charge dependent.

5.2.1 NAD^+ adsorption kinetics

Fig. 5.16 gives information on the NAD^+ adsorption equilibrium at long adsorption times (differential capacitance plateau). However, the results in the Fig. 5.16 also provide information on the NAD^+ adsorption kinetics. For example, if we take a curve recorded at a specific concentration and monitor its trend, we can see that the differential capacitance decreases with time, first sharply due to an increase in electrode surface coverage by NAD^+, then gradually approaches an equilibrium plateau. The time-dependant change in differential capacitance in Fig. 5.16 can thus be directly related to the NAD^+ adsorption kinetics.

In order to further analyze the differential capacitance data in terms of the adsorption kinetics, the differential capacitance values were converted into NAD^+ surface

coverage values, θ, using Eq. (5.11), and selected curves are presented in Fig. 5.19 for the three electrode potentials investigated in this work.

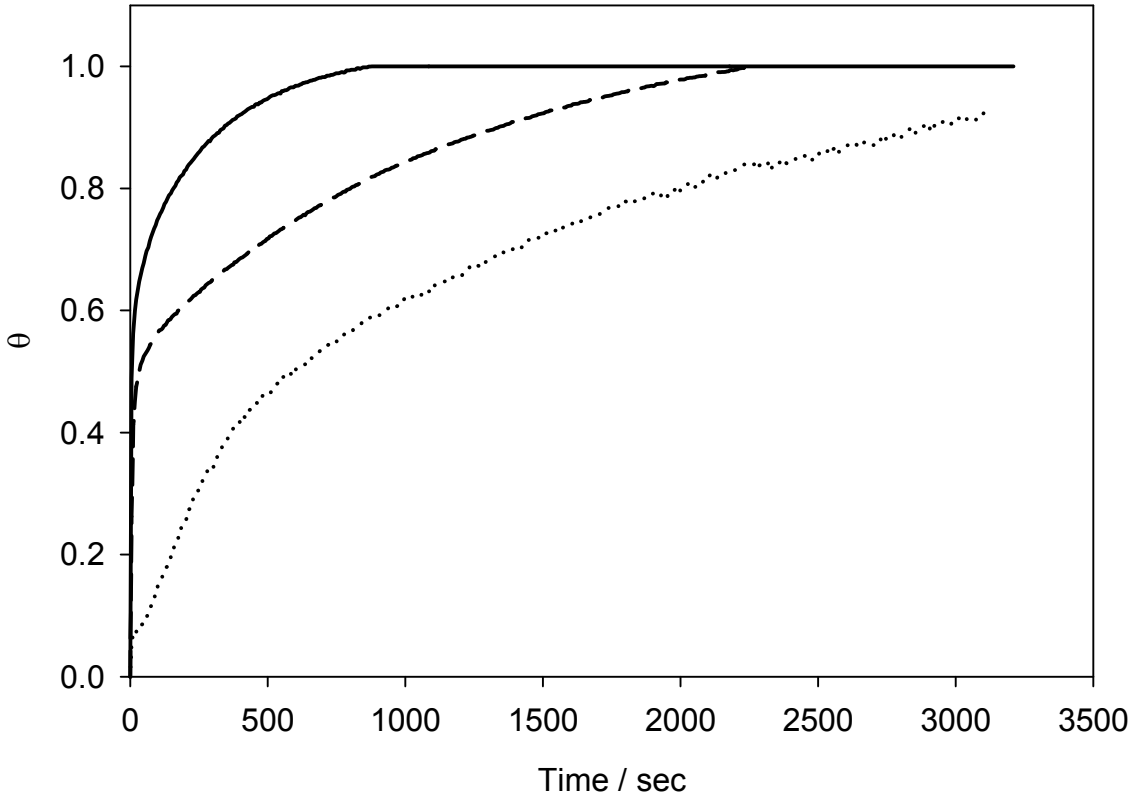

Figure 5.19: Time dependence of the NAD^+ relative surface coverage recorded at 0.5 V (solid line), 0.05 V (dashed line), and –0.8 V (dotted line) in 0.1 M $NaClO_4$ + 1 mM NAD^+. The data were obtained from differential capacitance measurements and using Eq. (5.11). Temperature, T = 295 K.

Fig. 5.19 clearly shows that the kinetics of NAD^+ adsorption on a GC electrode surface changes significantly by changing the electrode potential. Namely, when the electrode is positively charge (0.5 V), the surface coverage increases sharply and reaches an equilibrium plateau (equilibrium) in ca. 880 seconds (Fig. 5.19, solid line). On the other hand, when the electrode is negatively charged (–0.8 V), the coverage increases slowly and do not reach an equilibrium within the time frame of the experiment (Fig. 5.19, dotted line). Hence, similarly to the results in Figs. 5.17 and 5.18, the origin of the potential-dependant behavior in Fig. 5.19 could be described in the same way, *i.e.* by the influence of electrostatic interactions between NAD^+ and the GC electrode surface.

Thus, it appears that these interactions do not only influence the interactive behavior of NAD^+ at the GC surface at equilibrium conditions (*i.e.* the adsorption "bond" strength), but also they govern the NAD^+ adsorption kinetics. Previous work from our laboratory reports similar results in the case of NAD^+ adsorption on a gold electrode surface [103].

In order to model the experimental data, a two-step kinetic model was used. An attempt to use a simpler kinetic model was made, but the agreement between the experimental data and the model was rather poor. The two-step model is schematically presented in Fig. 5.20.

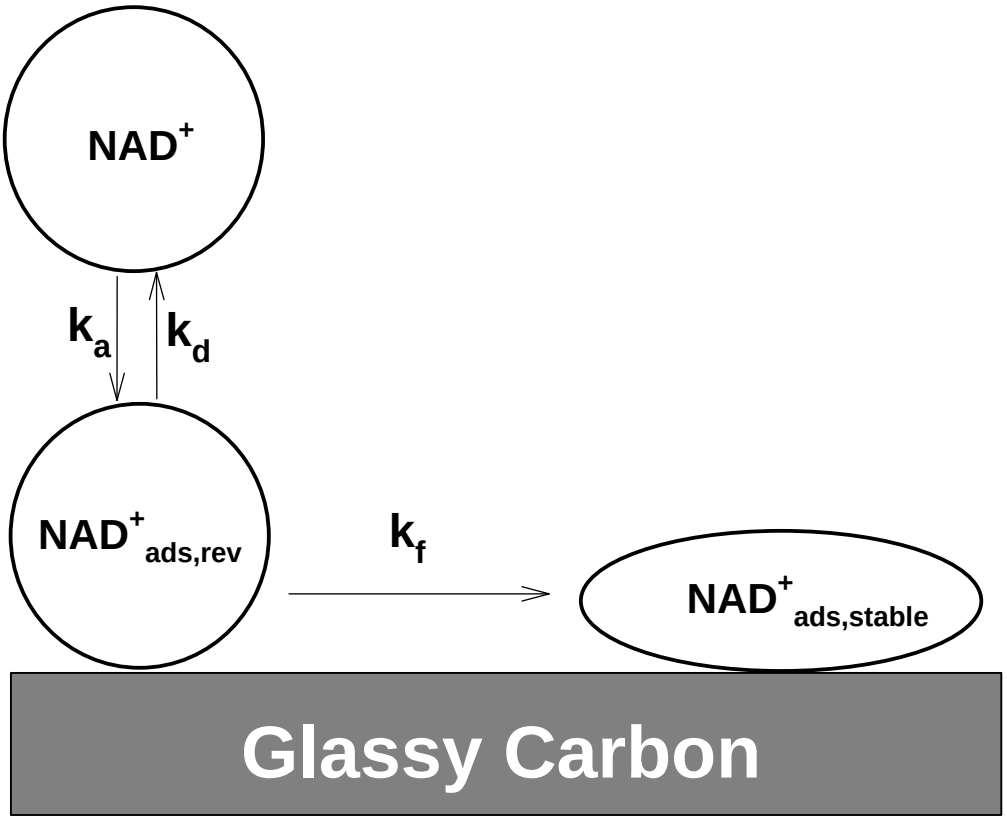

Figure 5.20: Schematic of NAD^+ adsorption kinetics model.

In the first step, NAD^+ initially adsorbs on a GC surface in a reversible manner. However, this $NAD^+_{ads,rev}$ is not thermodynamically stable on the GC surface, and may either revert back to NAD^+ in the solution (desorb), or transform into a more thermodynamically-stable surface conformation of the molecule, $NAD^+_{ads,stable}$, The latter

process is assumed to be irreversible. This adsorption kinetics model can be described by the following kinetic equations [108, 109]:

$$\frac{d\theta_1}{dt} = k_a c(1-\theta_1-\theta_2) - (k_d + k_f)\theta_1 \tag{5.14}$$

$$\frac{d\theta_2}{dt} = k_f \theta_1 \tag{5.15}$$

$$\frac{d\theta}{dt} = \frac{d\theta_1}{dt} + \frac{d\theta_2}{dt} = k_a c(1-\theta) - k_d \theta_1 \tag{5.16}$$

where $\theta = \theta_1 + \theta_2$ and $0 \le \theta \le 1$ is the fraction of surface covered by NAD^+ in both reversible and irreversible configurations, θ_1 is the fraction of the surface covered by the thermodynamically unstable $NAD^+_{ads,rev}$ configuration (reversibly bound NAD^+) while θ_2 is the fraction of surface covered by thermodynamically stable $NAD^+_{ads,stable}$ configuration (irreversibly bound NAD^+), k_a ($dm^3\ mol^{-1}\ s^{-1}$) is the adsorption kinetic constant, k_d (sec^{-1}) is the desorption kinetic constant, and k_f (sec^{-1}) is the transformation (surface rearrangement) constant.

In order to fit the experimental data to the kinetics model, the parameter k_a, k_d and k_f were systematically varied using the Solver function in Excel so that the sum of the squares of errors between the simulated and the experimental data was minimized. Fig. 5.21 shows an example of the fit.

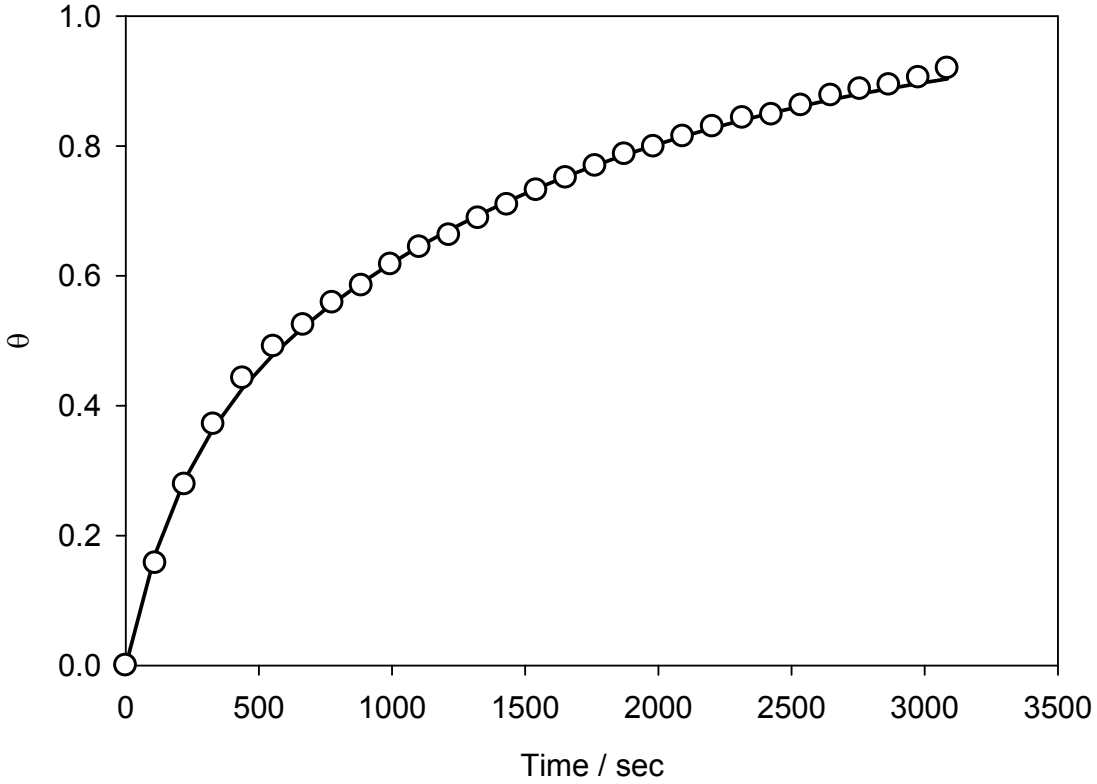

Figure 5.21: Dependence of NAD^+ surface coverage on time calculated from differential capacitance measurements preformed at electrode potentials of –0.8 V. Symbols represent experimental data, whereas the line represents simulated data following the adsorption kinetics model in Fig. 5.20. $[NAD^+]$ = 1 mM.

It can be seen from Fig. 5.21 that the proposed kinetics model yields an excellent agreement between the experimental (circles) and simulated data (line), thus justifying its application. Kinetic parameters obtained by the fitting procedure are presented in Table 5.3.

Table 5.3: Parameters of the NAD^+ adsorption kinetics as a function of GC electrode potential. The data were obtained by fitting the experimental data from Fig. 5.19 using the proposed two-step kinetic model presented in Fig. 5.20, $[NAD^+]$ = 1 mM.

E / V	$k_a \times 10^{-2}$ / dm^3 mol^{-1} s^{-1}	$k_d \times 10^2$ / s^{-1}	$k_f \times 10^2$ / s^{-1}
–0.80	11.00	12.50	10.40
0.05	78.05	29.30	22.20
0.50	352.80	40.00	24.10

Table 5.3 shows the effect of surface charge (electrode potential) on the adsorption kinetics of NAD^+ on GC electrode surface in term of adsorption, desorption and transformation rate constants. Namely, increasing the potential to more positive (anodic) values, k_a, k_d and k_f increase. Nevertheless, only the two latter constants could be relatively compared, since they have the same unit. The table shows that the desorption constant is slightly higher than the transformation constant. However, the rate of the formation of the two surface forms of NAD^+ (thermodynamically unstable and stable) is next analyzed. Further, the results in the table show that the change in electrode potential has a much greater influence on the adsorption rate constant, k_a, than on the other two constants. This indicates that the surface potential predominantly influences the forward adsorption step.

In order to get more detailed mechanism of NAD^+ adsorption on a GC electrode surface θ, θ_1 and θ_2 were calculated using the proposed kinetic model and plotted as a function of time as shown in Fig. 5.22.

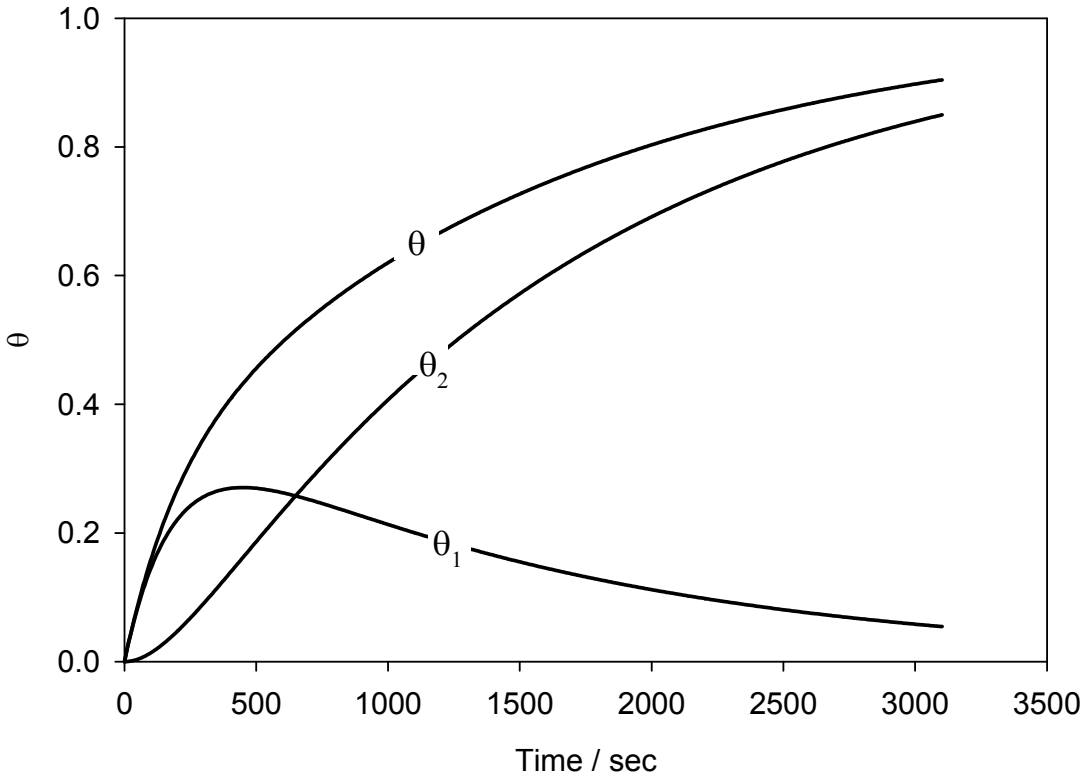

Figure 5.22: Time dependence of total NAD^+ surface coverage (θ), surface coverage with reversibly (θ_1) and irreversibly (θ_2) attached NAD^+ obtained by modeling the data in Fig. 5.21 using Eqs. (5.14) – (5.16).

Fig. 5.22 shows that within the first ca. 300 seconds of adsorption, an initial increase in total NAD^+ surface coverage (θ) is mostly due to the adsorption of NAD^+ on the GC electrode surface to form the thermodynamically unstable $NAD^+_{ads,rev}$, θ_1. A maximum in surface coverage with this form of NAD^+ was obtained at 445 seconds, and it is 27.5%. After the maximum, θ_1 gradually decreases and does not reach a constant value within the time frame of the experiment. On the other hand, the surface coverage with a thermodynamically stable form of $NAD^+_{ads,stable}$ gradually increases in the entire time interval studied, and starts becoming predominant after 700 sec. The result in Fig. 5.22 indicates that at long adsorption times, the predominant form of NAD^+ on the GC electrode surface is thermodynamically stable $NAD^+_{ads,stable}$.

It would now be interesting to compare the influence of surface potential on the kinetics of formation of $NAD^+_{ads,rev}$ and $NAD^+_{ads,stable}$, separately. For this reason, a time behavior of θ_1 and θ_2 was plotted on two separate graphs, Fig. 5.23 and Fig. 5.24 respectively.

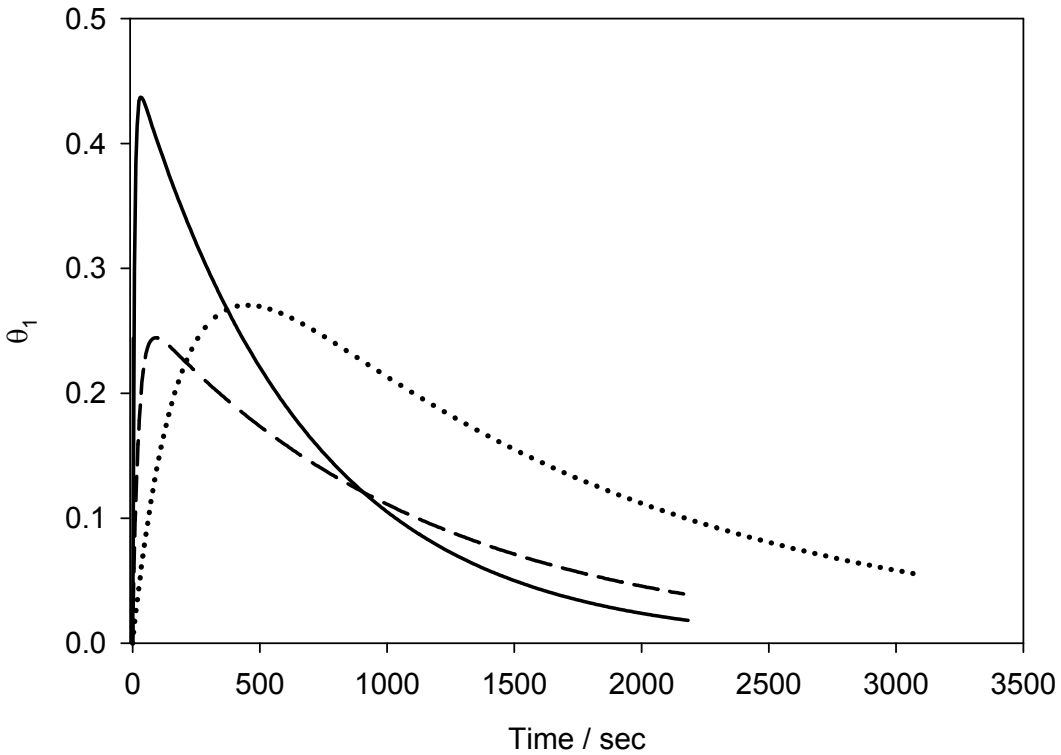

Figure 5.23: Time dependence of GC surface coverage by thermodynamically unstable $NAD^+_{ads,rev}$ (θ_1) obtained by modeling the data in Fig. 5.19 using Eqs. (5.14) – (5.16). GC electrode potentials were: 0.5 V (solid line), 0.05 V (dashed line) and –0.8 V (dotted line).

Three major behaviors could be noted from Fig. 5.23. First, with an increase in electrode potential to more positive values, a maximum in GC surface coverage by thermodynamically unstable form of NAD^+ ($NAD^+_{ads,rev}$) is reached at shorter times. Second, the slope of the rising part of the curve (very short adsorption times) increases with an increase in electrode potential (Table 5.4). Third, at longer adsorption times, the surface coverage by $NAD^+_{ads,rev}$ decreases with an increase in electrode potential. Thus, the kinetics of both the formation, but also the 'disappearance' (which induces desorption and transformation of $NAD^+_{ads,rev}$) is faster at positive potentials.

Table 5.4: Initial rate of $NAD^+_{ads,rev}$ formation on the GC electrode surface at different electrode potentials. $[NAD^+] = 1$ mM.

E / V	$d\theta_1/dt \times 10^4 (s^{-1})$
–0.80	11.00
0.05	78.00
0.50	353.00

Similarly, Fig. 5.24 shows the effect of electrode potential on the formation of a thermodynamically stable form of adsorbed NAD^+ on GC electrode surface ($NAD^+_{ads,stable}$).

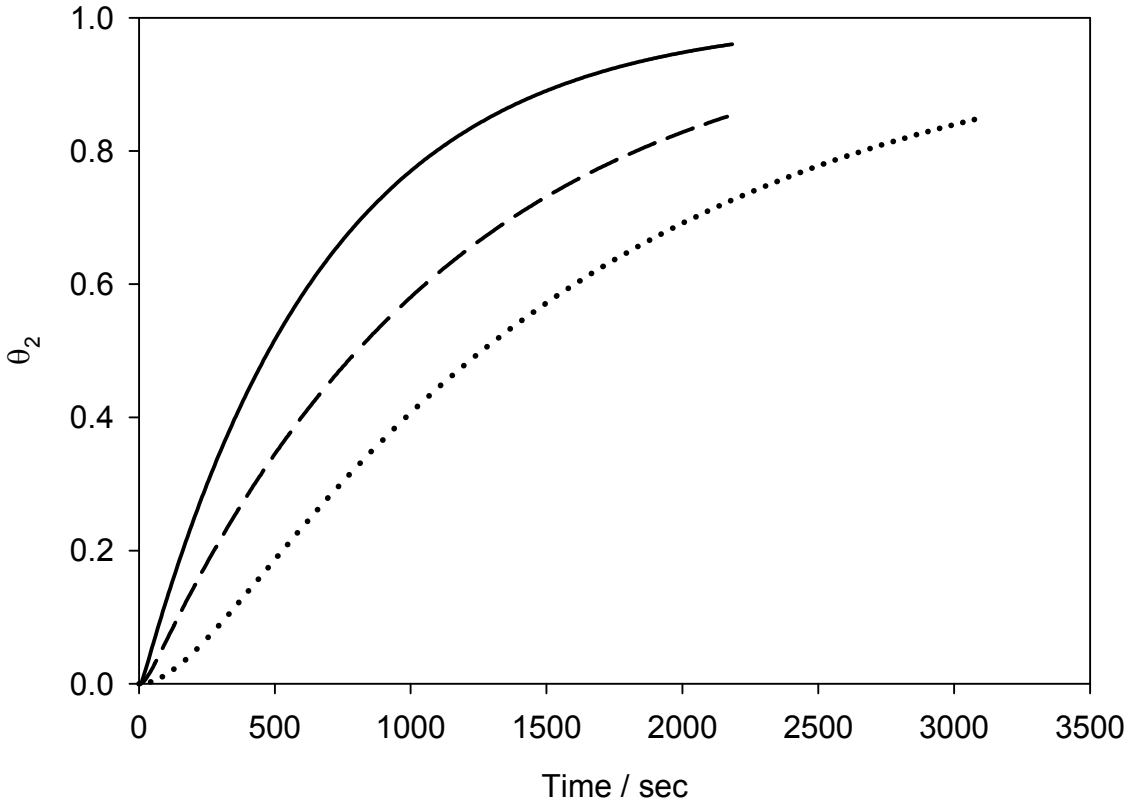

Figure 5.24: Time dependence of GC surface coverage by thermodynamically stable $NAD^+_{ads,stable}$ (θ_2) obtained by modeling the data in Fig. 5.19 using Eqs. (5.14) – (5.16). GC electrode potentials were: 0.5 V (solid line), 0.05 V (dashed line) and –0.8 V (dotted line).

Fig. 5.24 shows that (i) the initial rate of formation of $NAD^+_{ads,stable}$ (θ_2) increases with an increase in electrode potential, and (ii) that at a constant time, the surface coverage by $NAD^+_{ads,stable}$ also increases in the same manner.

It was shown in this section of the thesis that the kinetics of NAD^+ adsorption is highly dependant on the GC electrode surface potential (charge), and it increases with an increase in surface potential to positive values. The adsorption process involves the formation of two forms of NAD^+ on the surface; the thermodynamically unstable ($NAD^+_{ads,rev}$) and stable ($NAD^+_{ads,stable}$) form.

5.2.3 ATR-FTIR measurements

The previous two Sections (5.2.1 and 5.2.2) demonstrated that, under the experimental conditions performed, NAD^+ adsorbs on the GC surface regardless of the surface charge, although the surface charge was found to play a major role on the thermodynamics and kinetics of NAD^+ adsorption. In order to get a 'fingerprint' of the NAD^+ adsorption surface layer, infrared analysis was further performed.

First, NAD^+ was adsorbed on a GC electrode surface from a 1 mM NAD^+ solution and at a constant potential, during a period of 3 hours. Referring to Fig. 5.17, one can see that this concentration results in a saturated (maximum) GC surface coverage by NAD^+. Next, such a prepared surface was characterized by attenuated total reflection Fourier transform infrared spectroscopy (ATR-FTIR), and the resulting spectrum is presented in Fig. 5.25.

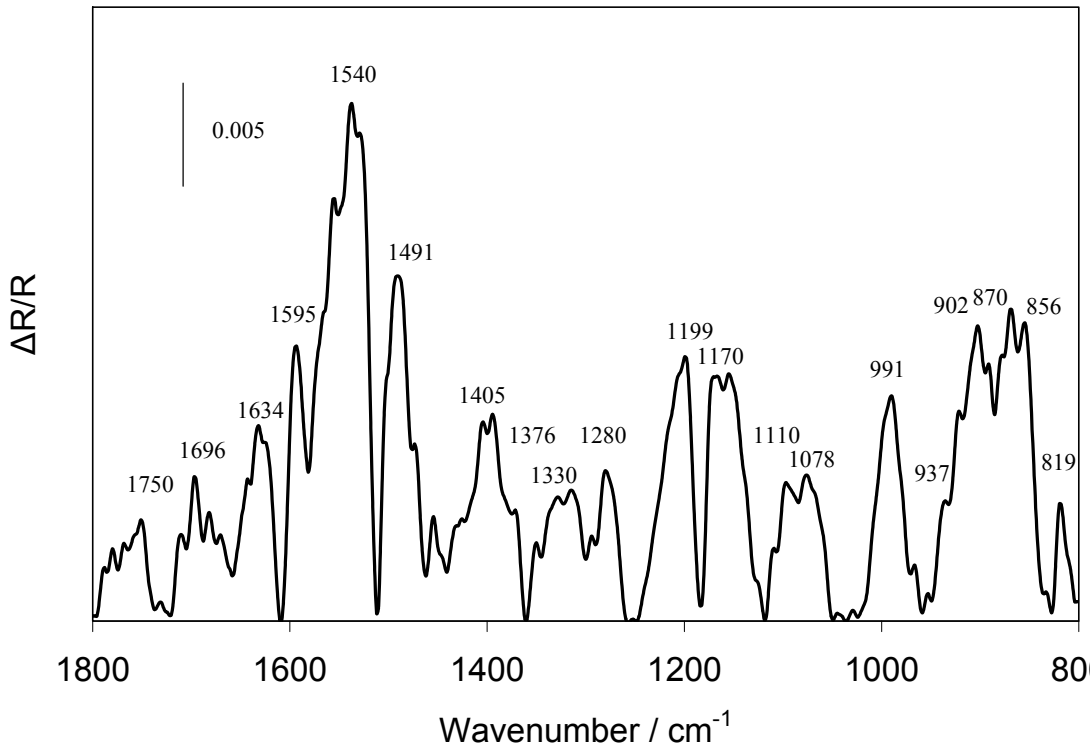

Figure 5.25: ATR-FTIR spectrum of NAD^+ adsorbed on a GC electrode surface from 0.1 M $NaClO_4$ solution containing 1 mM NAD^+ at electrode potential of 0.05 V.

Several characteristics peaks of NAD^+ are visible on the spectrum. The corresponding band assignments are listed in Table 5.5.

Table 5.5: Band assignments of NAD^+ adsorbed on a GC surface obtained using ATR-FTIR spectroscopy presented in Fig. 5.25.

ATR-FTIR wavenumber / cm^{-1}	Assignment	ATR-FTIR wavenumber / cm^{-1}	Assignment
1750 w	C=O Stretch (N)	1199 s	R_2 / N (R near N)
1696 w	C=O Stretch (N)	1170 s	R
1634 m	NH_2 bend (A)	1110 w	R
1595 m	C_5–C_6 stretch (A)	1078 w	P=O symmetric stretch
1540 vs, br	C–N stretch	991 s	Ring stretch Py
1491 s	A	937 vw, sh	C–NH_2 stretching
1405 m	N	902 m	P
1376 vw, sh	A	870 m	P
1330 w	A	856 m	R_1 / P (R near A)
1280 w	P=O asymmetric stretch	819 w	R

Abbreviations: vs, very strong; s, strong; m, medium; w, weak; vw, very weak; sh, shoulder; br, broad; N, nicotinamide; A, adenine; P, phosphate; R, ribose; R_1 ribose near A and R_2 ribose near N.

It is well known that ribose does not absorb in the 1800-1200 cm^{-1} region of the IR spectrum. Thus, in Fig. 5.25, the major bands above 1200 cm^{-1} are associated with the adenine ring system, while all the major bands below 1200 cm^{-1} correspond to the ribose moiety. The weak peaks at 1750 and 1696 cm^{-1} can be assigned to the carboxamide carbonyle (C═O) stretch of the nicotinamide ring [110-112] while the peak at 1634 cm^{-1} is the bending of NH_2 in the adenine moiety [110, 113, 114]. Further, the peak at 1595 cm^{-1} represents C_5-C_6 stretching [110, 114] while the very strong and broad peak at 1540 cm^{-1} represents the C-N stretching vibration in the nicotinamide moiety [110, 115]. The strong peak at 1491 cm^{-1} and two weak shoulders at 1376 and 1330 cm^{-1} represent adenine, while the peak at 1405 cm^{-1} can be assigned to nicotinamide [115]. The weak

peaks at 1078 and 1280 cm^{-1} can be assigned to the asymmetric P═O stretch of the pyrophosphate bridge that links the nicotinamide and adenosine moieties [116-119]. On the other hand, the two strong peaks at 1199, 1170 and two weak peaks at 1110 and 819 cm^{-1} correspond to the ribose moiety [110, 113, 120], while the peak at 856 cm^{-1} represents the ribose moiety near adenine [113]. The strong peak at 991 cm^{-1} corresponds to ring stretching of pyridine [111], while a very weak shoulder at 937 cm^{-1} represents C-NH_2 stretching [121]. Finally, the peaks at 902 and 870 cm^{-1} represent the phosphate groups [113, 120].

In general, the vibrations visible in the spectrum in Fig. 5.25 agree with those reported in the literature. Thus, the ATR-FTIR measurements further confirmed that NAD^+ indeed adsorbs on the GC electrode surface. In conclusion, the results presented in this entire section of the thesis indicate that reduction of NAD^+ indeed involves NAD^+ adsorption on the GC electrode surface, as one of the reaction steps.

5.3 Direct electrochemical regeneration of enzymatically-active 1,4-NADH

This thesis section focuses more on the applied part of the project. The section is divided into two major sub-sections.

- Section 5.3.1 presents results on 1,4-NADH regeneration on *non-modified* (bare) electrodes. The influence of electrode potential on the purity of enzymatically-active 1,4-NADH regenerated from NAD^+ is discussed.
- Section 5.3.2 concentrates on the development of *bi-functional nano-patterned* electrodes and their performance in regenerating 1,4-NADH from NAD^+.

All the 1,4-NADH regeneration experiments presented in Section 5.3 were done in a batch electrochemical reactor.

5.3.1 Electrochemical regeneration of 1,4-NADH on *non-modified* electrodes

Non-modified (bare) metal electrodes would be best candidates for electrochemical application, and consequently 1,4-NADH regeneration. However, as already mentioned, many research groups concluded that these electrodes are not capable of regenerating 1,4-NADH at high-purity, and the major product is NAD_2 (Step 2b, Scheme 1). This is due to the slow NAD-radical protonation (Step 2a, Scheme 1). However, one can see that the kinetics of Step 2a (Scheme 1) depends on the concentration of H^+ at the reaction site. This H^+ can react with the adsorbed NAD-radical, according to the Eley-Rideal mechanism, or it can be first adsorbed on the electrode surface as $M\text{-}H_{ads}$ and then react with the neighboring NAD-radical, following the Langmuir-Hinshelwood mechanism [122]. If the reaction follows the latter mechanism, then the kinetics of the reaction, and thus the amount of enzymatically-active 1,4-NADH produced (relative to NAD_2), would be dependent on the hydrogen surface coverage. The latter, in turn, depends on both the electrode material and electrode potential. However, these two effects have not been investigated by other laboratories in relation to the 1,4-NADH regeneration reaction, and the aim of this section of the thesis is to provide information that would fill this gap. It will be shown that the 1,4-NADH regeneration

kinetics indeed depends on the 1,4-NADH regeneration potential and electrode material, both predominantly controlling the H_{ads} surface coverage and the M-H_{ads} bond strength. Electrode potential was conveniently controlled externally (using a potentiostat), while the strength of the M-H_{ads} bond was varied by choosing different electrode materials (M = Ti, Cd, Co, Ni).

First, the effect of electrode potential on the 1,4-NADH regeneration kinetics will be discussed. A glassy-carbon (GC) electrode was initially used in these experiments, due to its corrosion/dissolution inertness and the possibility of comparing the results to those previously discussed in the thesis (Sections 5.1.1 and 5.1.2).

5.3.1.1 Glassy carbon electrode

It was reported in Sections 5.1.1 and 5.1.2 that the number of electrons exchanged in the NAD^+ reduction reaction is equal to 1.6 (Table 5.1). This indicates that the reduction of NAD^+ on GC proceeds through the formation of both 1,4-NADH (60 mol%) and NAD_2 (40 mol%). However, it should be noted that this conclusion is restricted only to the experimental conditions used in the analysis, most notably to the electrode potential region of NAD^+ reduction peaks in potentiodynamic experiments (ca. –1.5 V) and to the type of electrode polarization method, which was potentiodynamic. However, in an industrial setting, 1,4-NADH regeneration would not be performed under potentiodynamic conditions, but rather potentiostatic. Now, the question is – what would be corresponding regeneration potential that would ensure the highest recovery (purity) of enzymatically active 1,4-NADH?

In order to answer this question, regeneration of 1,4-NADH from NAD^+ was performed in a batch electrochemical reactor using a GC electrode polarized at various potentials. The 1,4-NADH potential region of interest was defined on the basis of potentiodynamic experiments presented in Fig. 5.26. The important features of the curves were already discussed in the thesis in relation to Figs. 5.1, 5.4 and 5.15, and thus will not be repeated here. Briefly; the curves in Fig. 5.26 demonstrate that NAD^+ is being reduced at potentials negative of ca. –1.3 V. Consequently, the potential region of interest for potentiostatic 1,4-NADH regeneration was chosen to be from –1.4 V to -2.3 V. Potentials

positive of –1.4 V were not chosen due to the fact that the 1,4-NADH regeneration reaction would be too slow, as evident from the difference in currents between the two curves in Fig. 5.26. On the other hand, the cathodic potential limit was extended beyond that in Fig. 5.26. This is because of the high overpotential of the hydrogen evolution reaction (HER) on the GC electrode, as evidenced by curve (1) in Fig. 5.26. Hence, to ensure high surface coverage of GC by H_{ads}, the regeneration potential region was extended to –2.3 V.

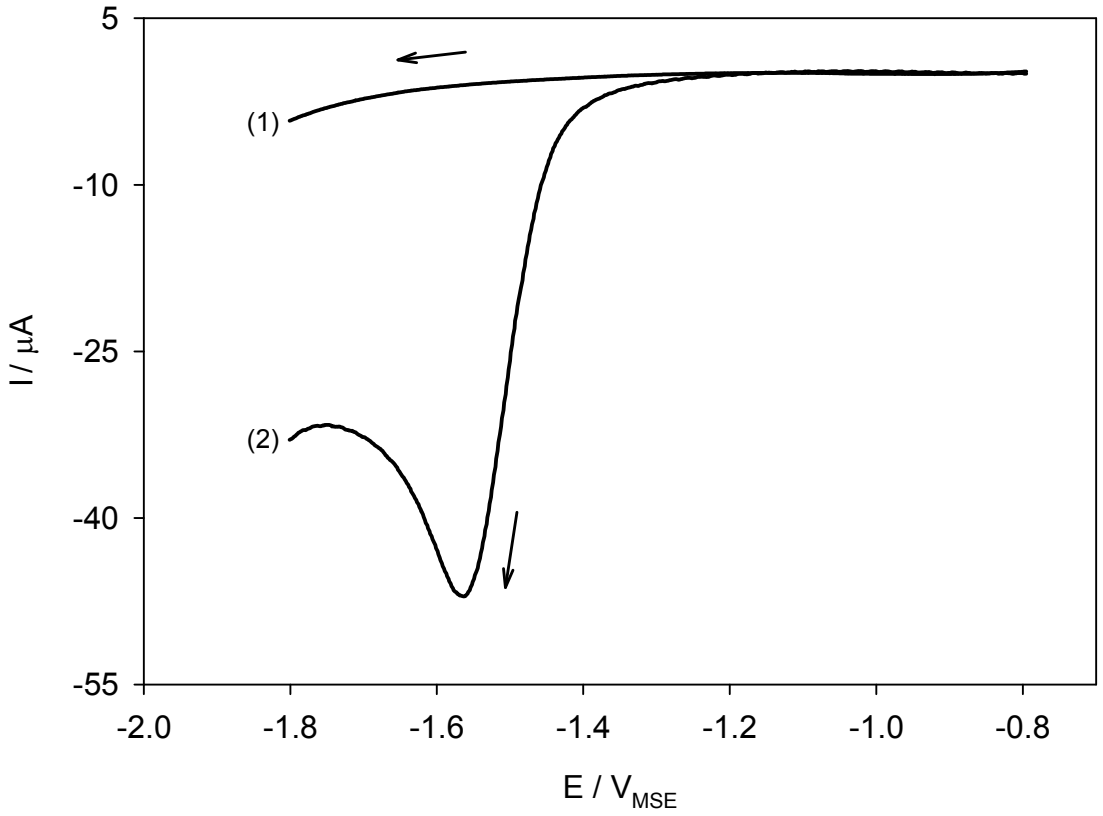

Figure 5.26: Linear polarization voltammograms of GC electrode recorded in (1) the supporting electrolyte, and (2) in the supporting electrolyte containing 4 mM NAD^+. Scan rate, sr = 100 mV s^{-1}.

The electrolysis of NAD^+ was then performed at several selected electrode potentials, from –1.4 V to –2.3 V. During the electrolysis, the absorbance of the solution was measured using an UV/Vis spectrophotometer set up at 340 nm, in order to monitor the NAD^+ conversion (Fig. 5.27). After reaching semi-equilibrium at a particular electrode potential, the percentage of 1,4-NADH recovered from NAD^+ was then determined by the enzymatic assay described in the experimental part of the thesis

(Section 4.7). It should be noted that the absorbance at 340 nm corresponds to various NADH isomers, including enzymatically-active 1,4-NADH and NAD_2, and thus cannot be used to determine the actual amount of 1,4-NADH.

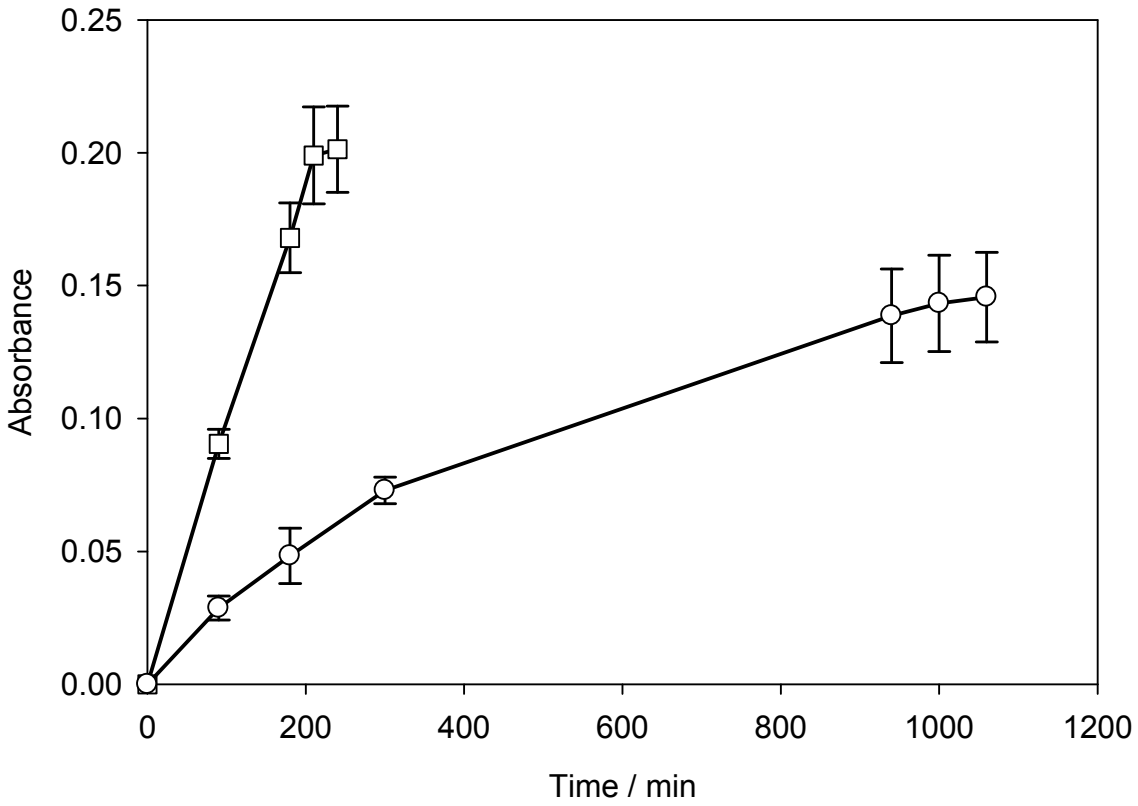

Figure 5.27: Time dependence of absorbance at 340 nm recorded during electrolysis of 1 mM NAD^+ in a batch electrochemical reactor operated at (O) –1.5 V and (□)–2.3 V.

Fig. 5.27 shows the time evolution of absorbance at 340 nm. At low NAD^+ reduction potential (circles), the conversion of NAD^+ (to NAD_2 and 1,4-NADH, Scheme 1) is rather slow. On the other hand, at a high reduction potential (squares), the NAD^+ reduction reaction rate is much faster, and an absorbance plateau is reached after ca. 240 minutes of electrolysis. Further, the final absorbance value at this potential, and thus the final (equilibrium) NAD_2 and 1,4-NADH concentration produced, is higher than at -1.4 V, which is in accordance with conditions of electrochemical equilibrium.

Since both NAD_2 and 1,4-NADH absorb at 340 nm, to distinguish between the two species, an activity assay was performed, following the procedure described in

Section 4.7. Briefly, the assay is based on the conversion of DL-lipoamide to dihydrolipoamide in the presence of lipoamide dehydrogenase [123]. This reaction requires a stoichiometric quantity of 1,4-NADH:

$$1,4-\text{NADH} + \text{DL-lipoamide} \xrightarrow{\text{lipoamide dehydrogenase}} \text{NAD}^+ + \text{dihydrolipoamide} \quad (5.17)$$

Hence, one can expect to see a decrease in absorbance at 340 nm during the occurrence of reaction (5.17) due to the oxidation of 1,4-NADH to NAD^+. The relative ratio of absorbance at 340 measured before reaction (5.17) starts, and after its completion, gives the percentage of enzymatically-active 1,4-NADH, in the 1,4-NADH/NAD_2 mixture. The assay was first calibrated using commercially available NADH that contains 98% of enzymatically-active 1,4-NADH.

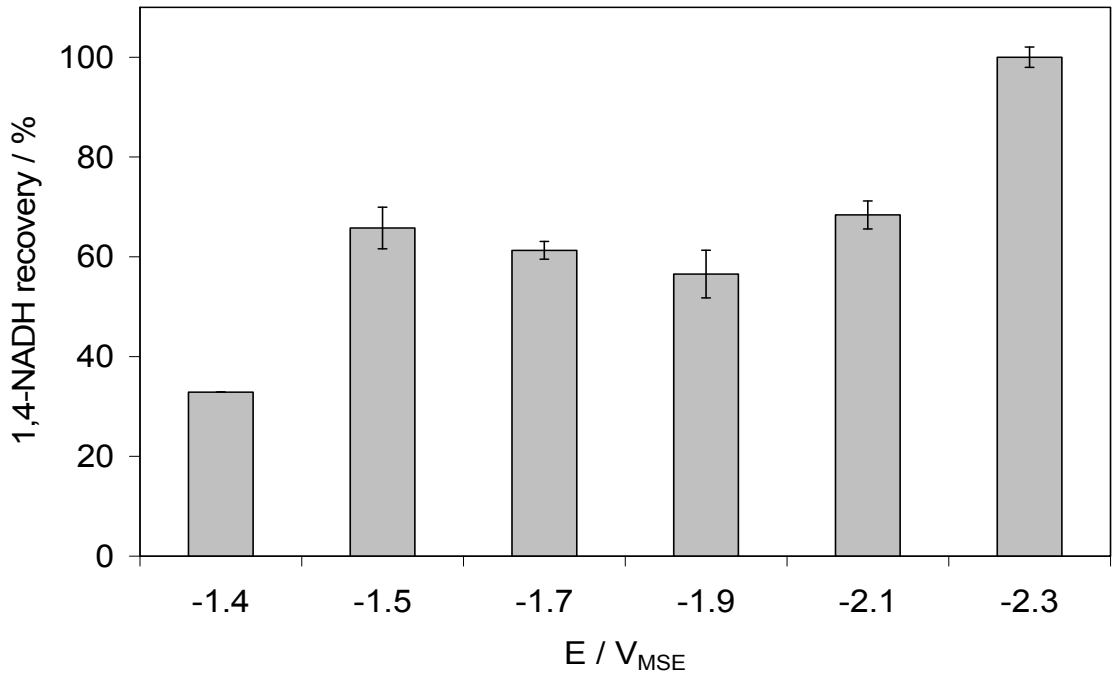

Figure 5.28: The percentage of enzymatically-active 1,4-NADH recovered on a GC electrode, obtained by reduction of 1 mM NAD^+ in a batch electrochemical reactor operating at different electrode potentials.

Fig. 5.28 shows the relative recovery percentage of enzymatically-active 1,4-NADH produced by electrolysis of 1 mM NAD^+ in a batch electrochemical reactor operated at various potentials (note that the percentage refers to the relative fraction of 1,4-NADH in the product mixture, and not to the degree of conversion of NAD^+ to

1,4-NADH). At the lowest electrolysis potential, –1.4 V, the 1,4-NADH recovery percentage is low (ca. 32%). However, it sharply increases to ca. 66 % at –1.5 V, and it then remains statistically relatively constant to –1.9 V. The corresponding statistical analysis confirmed that there is a significant statistical difference in the recovery of 1,4-NADH produce at –1.4 V and –1.5 V (p = 0.002). On the other hand, although the trend in the percentage of 1,4-NADH recovered going from –1.5 to –1.9 V is generally negative, p values between two neighboring points in this potential region are p = 0.16 and 0.09, respectively, and for all three points it is p = 0.06, confirming that there is, actually, no statistical difference among the values. However, increasing the electrode potential from –1.9 V to –2.1 V and then to –2.3 V, results in a statistically significant increase in the percentage of 1,4-NADH recovered (p = 0.019 and 0.025, respectively), yielding a surprising 100% recovery of 1,4-NADH at –2.3 V.

The behavior in Fig. 5.28 is quite puzzling; especially the fact that such a high recovery of enzymatically-active 1,4-NADH (100%) can be achieved on a bare electrode surface polarized at high cathodic potentials. Possible justification / explanation for the behavior in Fig. 5.28 could be explained on the basis of Scheme 1, which shows that the rate of NAD-radical protonation, and thus the rate and recovery of 1,4-NADH production, depends on both the rate of second electron transfer and the rate of protonation (Step 2a). By increasing the electrode potential to more negative (cathodic) values (Fig. 5.28), the electron-transfer rate increases, as well as the amount of H_{ads} adsorbed on the GC surface. Both of these should contribute to an increase in NADH production rate from NAD-radical, and thus to an increased recovery of enzymatically-active 1,4-NADH, as indeed observed in Fig. 5.28. The existence of a ‘plateau’ between –1.5 and –2.1 V can be explained on the basis of competition between the NAD-radical protonation rate (Step 2a, Scheme 1) and the molecular hydrogen evolution rate which both depends on the amount of H_{ads} on the GC surface. In addition, the influence of electrode surface potential on the surface orientation of a NAD^+ and/or NAD-radical molecule, and thus on the proximity of the electron/hydrogen acceptor site on the molecule to the electrode surface, should play a role [103]. To the best of the author's knowledge, no such high recovery (100%, Fig. 5.28) of 1,4-NADH has been previously reported on bare (non-modified) electrodes.

Knowing the composition of the final product mixture formed at –2.3 V (which is 100% 1,4-NADH), and referring to the UV/Vis calibration curve presented in the experimental part of the thesis, Fig. 4.3, it is possible to calculate the conversion of NAD^+ to enzymatically-active 1,4-NADH, and this value is 23%. Although, the percentage of 1,4-NADH recovered from NAD_2 is 100% at –2.3 V, the corresponding conversion is relatively low, making the use of a two-dimensional GC electrode in a real regeneration reactor, questionable. However, it should be noted that the NAD^+ conversion rate could conveniently be increased by employing an electrode of a larger surface area and by improving the hydrodynamics regime in the reactor.

One can increase the NAD^+ conversion on a GC electrode by employing a multiple electrode setup, but this would result in an increase in the electrochemical reactor volume. A solution to this problem would be to use a carbon-based surface of a very high roughness, *i.e.* very large surface-to-volume ratio. The hypothesis is that carbon nanofibers (CNFs) would fulfill this requirement, given that (i) this is a carbon-based material like GC, (ii) CNFs have a very large surface-to-volume ratio (the extrinsic factor), and (iii) CNF is a nano-sized material, thus offering a higher electrochemical activity (the intrinsic factor). Therefore, an attempt was made to use a CNF electrode to electrochemically regenerate 1,4-NADH from NAD^+, and the results are presented in the next section of the thesis.

5.3.1.2 Carbon nanofibers (CNFs)

In this work, the use of CNFs deposited on a stainless steel mesh, as a cathode in a batch electrochemical reactor for the regeneration of enzymatically-active 1,4-NADH is reported for the first time. CNFs were produced using a synthesis method developed in the Plasma Processing Laboratory of McGill University [83].

It will be shown that the NAD^+ conversion rate is significantly increased on the CNF cathode, in comparison with the GC electrode. It will also be shown that a 99% 1,4-NADH recovery from NAD^+ can be obtained when using the CNF cathode, thus making it a potential electrode candidate for large-scale applications in bioreactors.

5.3.1.2.1 Characterization of Carbon nanofibers

Fig. 5.29 shows electron micrographs of CNFs grown on the stainless steel mesh support at various magnifications. These CNFs consist of a tube-like structure, approximately 2 μm in length and 40-100 nm in diameter. Fig. 5.29c displays a transmission electron micrograph of several CNFs. It was observed that the CNFs consist of many graphene layers, some of which are parallel to the fiber axis, while others are extremely convoluted. Fig. 5.29d shows the results of the TGA analysis in air. The mass loss occurred at 848 K, which is typical for well-graphitized carbon [124]. No mass loss attributed to amorphous carbon (<773 K) was detected, evidencing that the CNFs produced were of high purity. In order to verify the stability of the CNF cathode, SEM images were taken before and after the NADH regeneration (Figs. 5.29a, e and Figs. 5.29b, f, respectively). The results demonstrate that the CNF cathode was stable; there were no significant structural, morphological, and topographical changes.

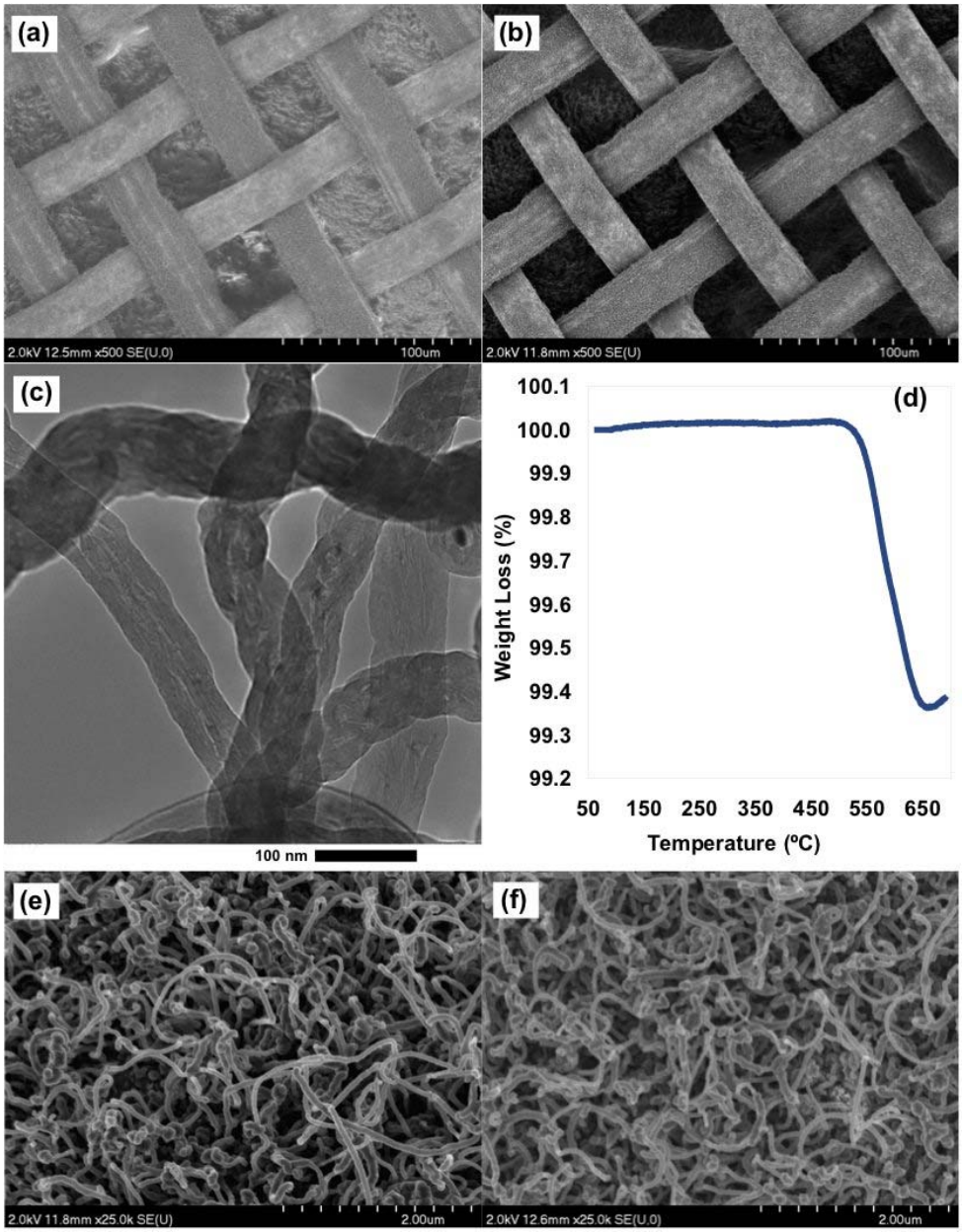

Figure 5.29: SEM micrographs of carbon nanofibers (*a* and *e*) before measurement, (*b* and *f*) after measurement, (*c*) TEM image and (*d*) TGA curve.

5.3.1.2.2 Electrochemical Regeneration of 1,4-NADH on CNFs

In order to investigate the NAD^+ reduction kinetics, and the efficiency of CNFs in producing (regenerating) enzymatically-active 1,4-NADH from NAD^+, potentiostatic (electrolysis) experiments were performed in the batch electrochemical reactor at a fixed electrode potential of –2.3 V. The rationale for performing the regeneration at this

potential is that earlier measurements on the 1,4-NADH regeneration in a batch electrochemical reactor employing a two-dimensional GC electrode showed that at this potential a 100% recovery of 1,4-NADH from NAD^+ can be obtained, without any production of non-enzymatically-active NAD_2 and NADH isomers (Fig. 5.28).

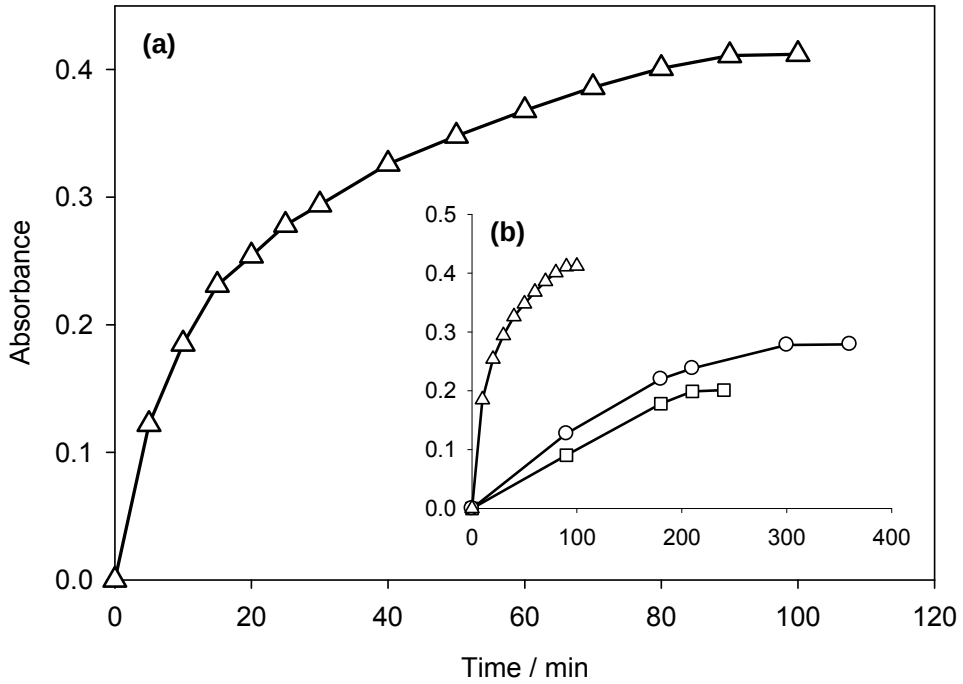

Figure 5.30: (*a*). Time dependence of absorbance at 340 nm recorded during the electrolysis of 1 mM NAD^+ in phosphate buffer in a batch electrochemical reactor operated at –2.3 V, using a CNFs cathode. (*b*) Comparison of the response of the CNFs cathode (triangles) to the response of the bare (CNFs-free) stainless steel 316 mesh (circles) and the GC electrode (squares). The axis titles are the same as in (*a*). The geometric surface area of the three electrodes was 12.5 cm^2.

Fig. 5.30a shows the time evolution of absorbance at 340 nm, during the reduction of NAD^+ on the CNFs cathode. This result can only be used to monitor the progress of NAD^+ reduction reaction, but not the progress of 1,4-NADH formation as both NAD_2 and 1,4-NADH absorb at this wavelength. The result shows that after ca. 90 minutes, a plateau was reached indicating that reaction (semi)equilibrium has been reached. Using UV/Vis calibration plot (Fig. 4.3), and taking into account that only 1,4-NADH was produced by electrolysis, from the result in Fig. 5.30a it has been determined that the NAD^+ conversion reached 48% after 90 minutes.

As it was hypothesized, a cathode made of CNFs should offer a significant increase in the rate of NAD^+ reduction kinetics in comparison to the GC electrode used in the previous section of the thesis. Fig. 5.30b shows a comparison among the kinetics of NAD^+ reduction on the CNFs cathode to that on the GC cathode and a 316 stainless steel mesh cathode (note that for all three electrodes geometric area exposed to the electrolyte was 12.5 cm^2). The 316 stainless steel mesh was used as the second control, since (i) it is not two-dimensional surface as the GC electrode, and (ii) CNFs were deposited on this mesh. The result in Fig. 5.30b proves that the hypothesis is correct. Indeed, the kinetics of NAD^+ reduction is fastest on the CNFs cathode. Only 90 minutes was required to reach a NAD^+ reduction reaction (semi)equilibrium state on the CNFs cathode, while it took 240 minutes on the GC electrode and 360 minutes on the stainless steel mesh to achieve (semi)equilibrium. In addition, the conversion of NAD^+ was also highest on the CNFs cathode (48%), while the GC and stainless steel mesh cathodes produced significantly lower levels (23 and 32%, respectively), as shown in Fig. 5.31.

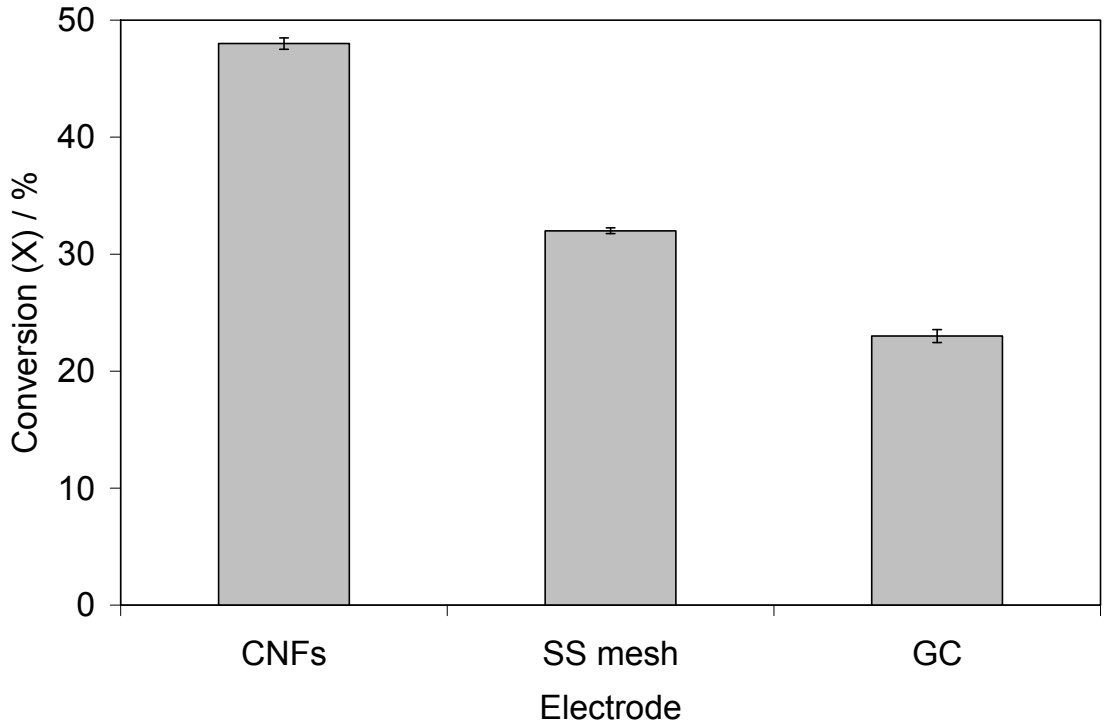

Figure 5.31: Conversion of NAD^+ to 1,4-NADH using different electrodes in a batch electrochemical reactor operated at –2.3 V. The geometric surface area of the three electrodes was 12.5 cm^2. [NAD^+] = 1 mM.

The next step in the attempt to prove the hypothesis was to determine the enzymatic activity of the product of NAD^+ reduction. The activity assay was performed in the same way as explained in Section 4.7.

The enzymatic assay performed on samples taken from the reactor that employed the CNFs cathode confirmed that 99.3 ± 0.6 % of the reduced NAD^+ was converted into enzymatically-active 1,4-NADH, while the amount converted in the reactor that employed the stainless steel mesh was only 12 %. This proves that CNFs deposited on a stainless steel mesh are highly electrocatalytically-active and selective towards conversion of NAD^+ into enzymatically-active 1,4-NADH. The fundamental origin of the increased electrocatalytic activity and selectivity of CNFs was related to the enhancement of the NAD-radical protonation kinetics (Step 2a, Scheme 1) by providing more 'active' hydrogen adsorbed on the CNFs surface, as already explained in the thesis in relation to the GC electrode.

The results presented in this and previous section demonstrated not only that the composition of the final product mixture (*i.e.* the percentage of 1,4-NADH in the product mixture) depends on the electrode potential, but also that the product mixture can contain only 1,4-NADH (100% recovery), despite the fact that bare (non-modified) GC and CNFs electrodes were used (which has not been reported in the literature). Furthermore, the CNF cathode was shown to enable fast electrochemical NAD^+ reduction kinetics (Fig. 5.30b) and high NAD^+ conversion relative to the GC and stainless steel mesh cathodes alone (Fig. 5.31).

It was then further hypothesized that the recovery of 1,4-NADH regenerated from NAD^+ is dependent not only on the electrode potential, but also on the *strength* of the metal electrode - hydrogen bond ($M\text{-}H_{ads}$). Namely, a metal that binds hydrogen more strongly (e.g. Ti) will attain a higher hydrogen surface coverage at more *positive* electrode potentials (lower NAD^+ reduction overpotentials). Consequently, the higher the hydrogen surface coverage, the faster the kinetics of Step 2a (Scheme 1), and higher the recovery of 1,4-NADH from NAD^+. In an attempt to prove the hypothesis, several selected bare (non-modified) metal electrodes (M = Ti, Ni, Co and Cd, in addition to the already investigated GC electrode) were investigated in a batch electrochemical reactor.

The respective M-H_{ads} bond strengths are 348.3, 195.9, 192.6 and 119.7 kJ mol^{-1} [125]. Hence, it was hypothesized that Ti would give a maximum 1,4-NADH recovery percentage at the most positive potentials (relative to other metals), while Cd would give it at more negative cathodic potentials. As it will be shown later in the thesis, this turned out to be the case.

5.3.1.3 Titanium electrode

In order to determine a potential region in which NAD^+ undergoes electrochemical reduction on Ti, linear voltammetry (LV) measurements were first performed using Ti as working electrode. Earlier measurements on GC electrode (Fig. 5.26) showed that a well-defined cathodic peak was observed at ca. –1.5 V in a NAD^+ containing solution, indicating that the reduction of NAD^+ occurs in this potential region. Fig. 5.32 shows the response of a Ti electrode recorded in the absence (dashed line) and presence (solid line) of NAD^+ in the electrolyte.

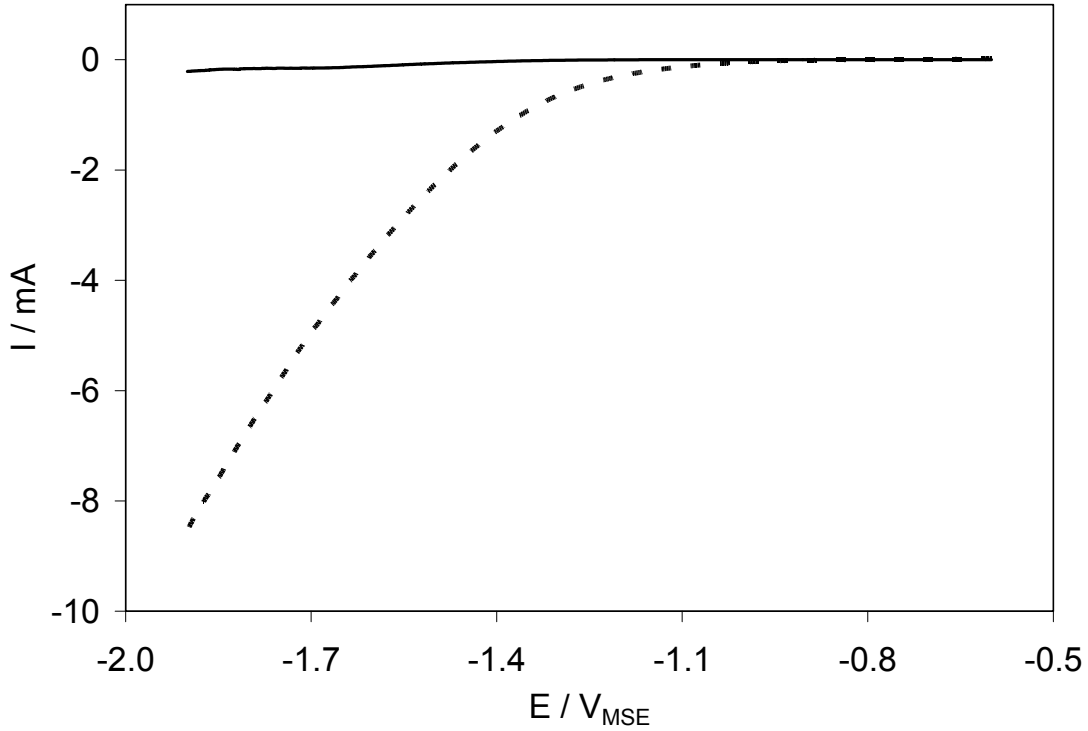

Figure 5.32: Linear voltammograms of a Ti electrode recorded in 0.1 M phosphate buffer solution in the absence of NAD^+ (dashed line) and in the presence of 4 mM NAD^+ (solid line). Scan rate: 10 mV s^{-1}. Temperature, T = 295 K.

The response of the Ti electrode in the absence of NAD^+ is as expected (dashed line); with an increase in cathodic potential past ca. –1.0 V, the resulting current also increases, which is due to the increase in the kinetics of the hydrogen evolution reaction (HER) [24, 28, 36]. Surprisingly, the response of the electrode in the NAD^+ containing solution was quite different than expected. Namely, while on GC, Au and GC-Ru electrodes a well-defined NAD^+ reduction peak can be observed at ca. –1.5 V [24, 29, 30, 36] (see Fig. 5.26 for GC), the peak is absent in Fig. 5.32. In addition, the NAD^+ reduction current/peak on the GC, Au and GC-Ru electrodes is significantly higher than the background current (in the absence of NAD^+), while the response on the Ti electrode (Fig. 5.32, solid line) is quite opposite, in which the recorded current is significantly lower than the background current (dashed line). A possible reason for the observed low current could be the adsorption of NAD^+ on the electrode surface, which blocks the HER, occuring on Ti more readily (*i.e.* at lower overpotential) than on GC, Au and GC-Ru. In fact, it is known that both GC and Au are poor HER catalysts.

To investigate if NAD^+ indeed adsorbs on the Ti electrode surface, the Ti sample that underwent linear polarization (Fig. 5.32, solid line) was characterized by polarization modulation infrared reflection absorption spectroscopy (PM-IRRAS), and the resulting spectrum is presented in Fig. 5.33.

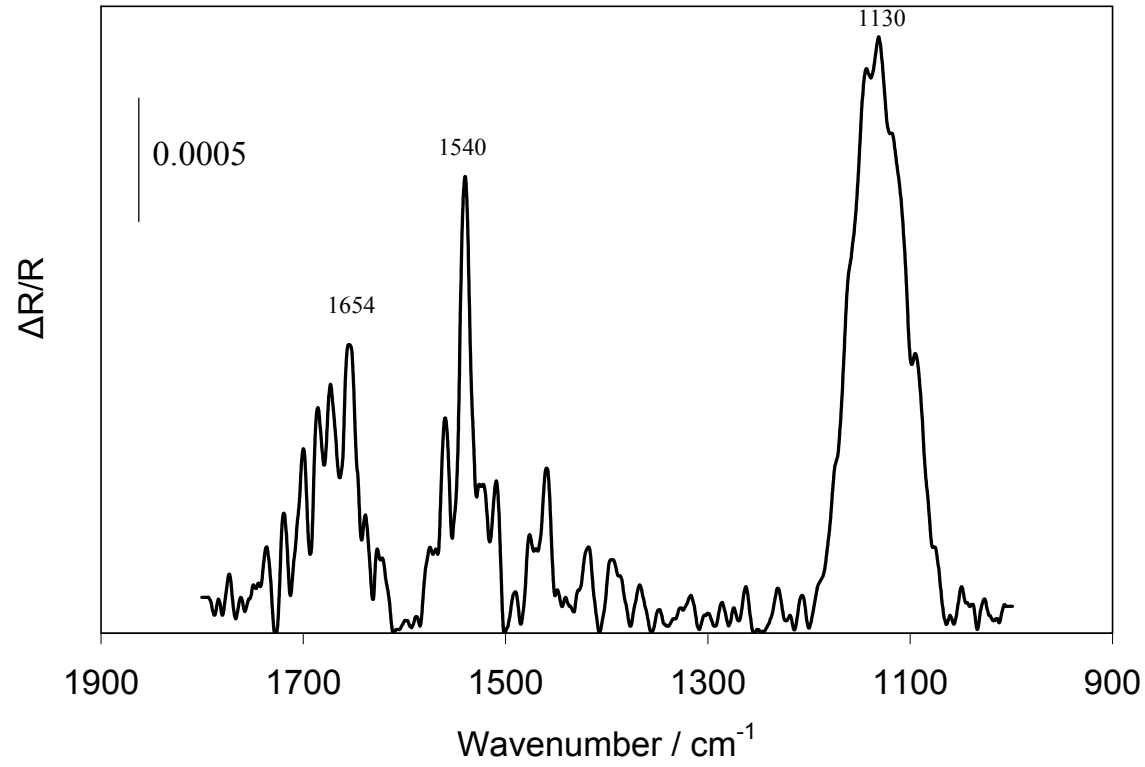

Figure 5.33: PM-IRRAS spectrum of a NAD^+ layer adsorbed on a Ti surface. The monolayer was adsorbed from 0.1 M phosphate buffer solution containing 4 mM NAD^+ solution by linear potentiodynamic polarization between –0.6 V and –1.9 V at scan rate of 10 mV s^{-1}. Temperature, T = 295 K.

The spectrum could be analyzed similarly to that presented earlier in the thesis (Fig. 5.25); however, it should be noted that the latter was obtained by adsorption of NAD^+ on the GC surface in the double-layer region, not in the region of NAD^+ reduction, as on Ti above). The well-pronounced peak at 1130 cm^{-1} corresponds to the response of the ribose moiety of NAD^+, while the peak at 1540 cm^{-1} represents the C-N stretching vibration in the nicotinamide moiety [103]. The vibration at 1654 cm^{-1} corresponds to the bending of NH_2 in the adenine moiety. Thus, the PM-IRRAS measurements confirmed that NAD^+ indeed adsorbs on the Ti electrode surface during the linear polarization in the potential region in Fig. 5.32, confirming that the decrease in the current in Fig. 5.32 is due to the blocking of the electrode surface by adsorbed NAD^+.

In order to regenerate enzymatically-active 1,4-NADH, long-term potentiostatic (electrolysis) experiments were done at several selected potentials in the potential region of NAD^+ reduction (from –1.4 to –2.3 V) in a batch electrochemical reactor using a Ti electrode. As explained earlier, the progress of the reaction (conversion of NAD^+) was

monitored by UV/Vis through measuring the absorbance at 340 nm, and the percentage of 1,4-NADH recovered from NAD^+ was determined by the enzymatic assay outlined in the experimental part of the thesis. Fig. 5.34 shows the percentage of 1,4-NADH recovered by reduction of NAD^+ on a Ti electrode as a function of electrode potentials (again, note that the percentage refers to the relative amount of 1,4-NADH in the product mixture, which could also contain NAD_2 and other NADH isomers, not to the amount of NAD^+ converted to 1,4-NADH).

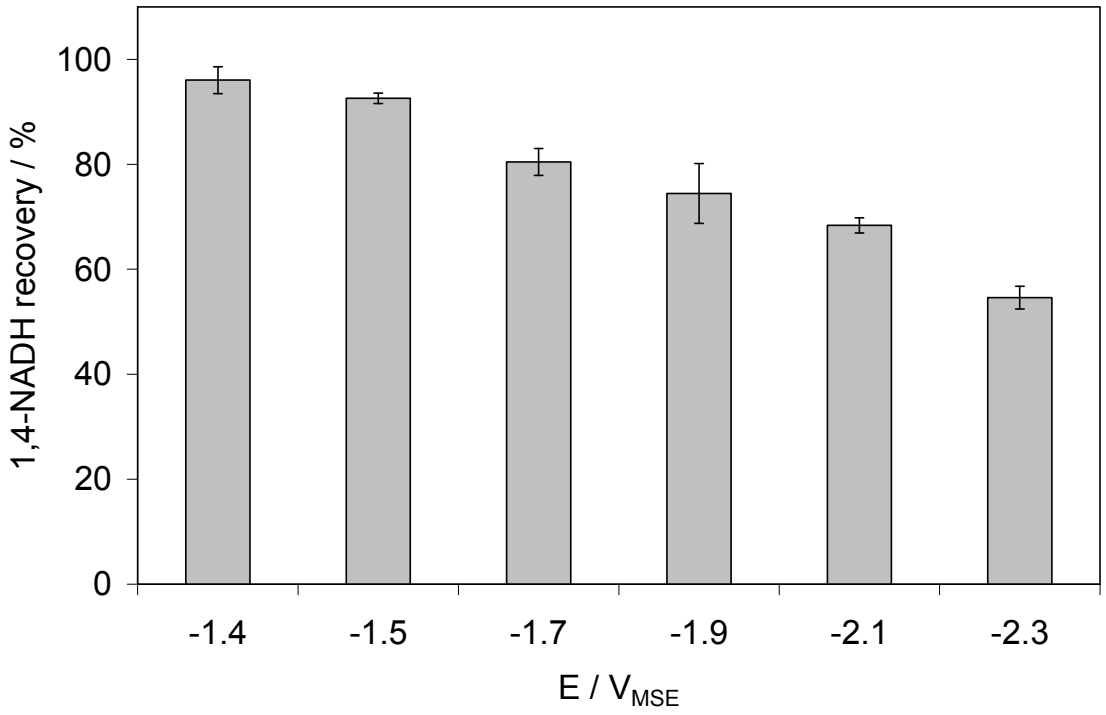

Figure 5.34: The percentage of enzymatically-active 1,4-NADH recovered on a Ti electrode, obtained by reduction of 1 mM NAD^+ in a batch electrochemical reactor operating at different electrode potentials.

Fig. 5.34 demonstrates that the percentage of recovered active 1,4-NADH is strongly dependent on the electrode potential. At the lowest cathode potential (–1.4 V), a maximum recovery (96.0 ± 2.6 %) of 1,4-NADH was obtained, and by increasing the potential to more negative values the recovery decreased gradually down to 54.0 ± 2.2 % (at –2.3 V). This behavior could be explained in the following manner; since, the electronic structure of Ti is such that the 3*d* orbital has only two unpaired electrons and

since hydrogen is an electron donor, the Ti-H_{ads} bond is strong (348.3 kJ mol^{-1}), and one can thus, expect that at low HER electrode potentials (–1.4 V here, Fig. 5.32), the surface coverage of H_{ads} on Ti is relatively high, compared to metals that form weak M-H_{ads} bonds. Since the NAD-radical protonation (Step 2a, Scheme 1) is a strong function of active hydrogen concentration, one can then expect to obtain a relatively high recovery of 1,4-NADH already at –1.4 V, as indeed demonstrated in Fig. 5.34. Then, why is there the decrease in the percentage of 1,4-NADH recovered with an increase in electrode potential to more negative values? This can be related to the competitive behavior of the NAD-protonation and H_2 evolution (HER) reactions, both starting with the formation of Ti-H_{ads} [126]:

$$T_i + H^+ + e^- \rightarrow T_i - H_{ads} \tag{5.18}$$

Due to the strong affinity of hydrogen for adsorption on titanium (because of the almost empty 3*d* orbitals in Ti), the kinetics of reaction (5.18) is fast even at low negative (cathodic) potentials in the HER region (Fig. 5.32). The second step in the HER is the formation of molecular hydrogen through one (or both) of the following reactions [126]:

$$T_i - H_{ads} + H^+ + e^- \rightarrow H_2 + T_i \tag{5.19}$$

$$2T_i - H_{ads} \rightarrow H_2 + 2T_i \tag{5.20}$$

The kinetics of the second step increases with an increase in electrode potential to more negative values and, thus, the total HER kinetics, which is evident in Fig. 5.32 (dashed line). Contrary, at more positive cathodic potentials the total HER kinetics is thus slow. Taking into account the high strength of the Ti-H_{ads} bond, this yields high surface coverage by hydrogen, Ti-H_{ads} (Eq.(5.18)), at positive potentials, and consequently the fast NAD-radical protonation kinetics (Step 2a, Scheme 1). This enables a high amount of 1,4-NADH to be recovered from NAD^+, Fig. 5.34. However, with the increase in electrode potential to more negative values, the HER kinetics increases (Fig. 5.32, dashed line) and the surface coverage of Ti-H_{ads} thus decreases. This in turns, results in a decrease in the NAD-radical protonation kinetics (Step 2a, Scheme 1) and an increase in

the NAD-radical dimerization kinetics (Step 2b, Scheme 1). As the result, there is a decrease in the percentage of 1,4-NADH recovered from NAD^+, *i.e.* an increase in the percentage of NAD_2 formed, as seen in Fig. 5.34.

5.3.1.4 Cadmium electrode

Similarly to the Ti electrode, 1,4-NADH regeneration experiments were also performed with a Cd electrode at various electrode potentials, and the corresponding results are presented in Fig. 5.35.

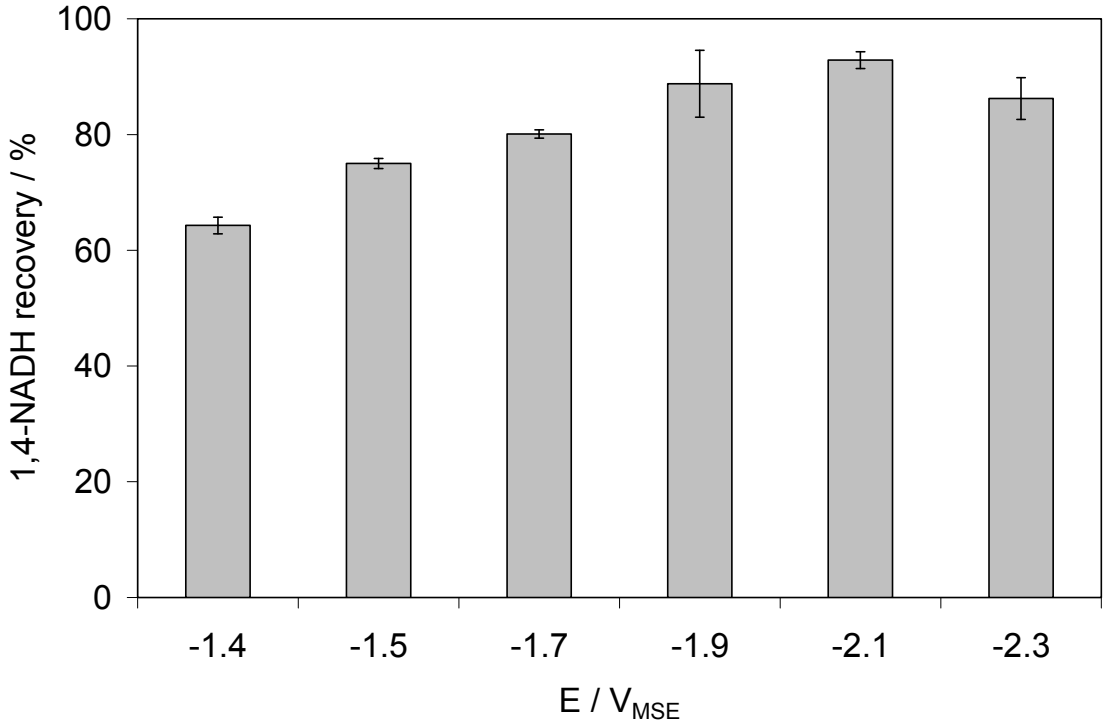

Figure 5.35: The percentage of enzymatically-active 1,4-NADH recovered on a Cd electrode, obtained by reduction of 1 mM NAD^+ in a batch electrochemical reactor operating at different electrode potentials.

The trend in Fig. 5.35 is opposite to that presented in Fig. 5.34, which was expected. Here at the lowest cathode potential (–1.4 V) a minimum percentage recovery (64.0 ± 1.4 %) of 1,4-NADH was obtained, but by increasing the potential to more negative values, the percentage recovery increased gradually, reaching a maximum of

93.0 ± 1.4% at –2.1 V, and then decreasing to 86.0 ± 3.6% at –2.3 V. As explained earlier, the percentage of 1,4-NADH regenerated from NAD^+ (relative to NAD_2) is dependent not only on the electrode potential, but also on the strength of the metal electrode - hydrogen bond (M-H_{ads}). Since, the Cd-H_{ads} bond is weak (119.7 kJ mol^{-1}), at low HER electrode potentials (–1.4 V) the Cd surface coverage by H_{ads} is, therefore, relatively low, compared to Ti that forms a strong M-H_{ads} bond. The reason for the low coverage of H_{ads} on Cd at low cathodic potentials is the weak adsorption affinity of hydrogen towards Cd, which is due to the completely filled *d* orbitals. Therefore, the kinetics of the hydrogen adsorption reaction (5.18) and, thus, the formation of the 'active' hydrogen (H_{ads}) is slow at low negative (cathodic) potentials. Consequently, the lower the hydrogen surface coverage, the slower the kinetics of Step 2a (Scheme 1), and the lower the percentage of 1,4-NADH recovered from NAD^+. On the other hand, by increasing the electrode potential to more cathodic values the surface coverage of H_{ads} on the Cd surface increases, and thus the kinetics of Step 2a (Scheme 1). This, in turn, results in an increase in recovery of 1,4-NADH, which is indeed visible in Fig. 5.35. The increase in electrode cathodic potential past –2.1 V has a negative impact on the recovery of 1,4-NADH, which is due to the increase in the kinetics of the competitive HER (Eq. 5.20).

5.3.1.4 Cobalt and nickel electrodes

The previous two sections demonstrated that when a M-H_{ads} bond is strong (such as Ti-H_{ads}) the highest recovery of 1,4-NADH is obtained at low cathodic potentials (Fig. 5.34), since at this potential, the electrode surface is already covered by H_{ads} which is a preferable species for the protonation of the NAD-radical (Step 2a, Scheme 1), as opposed to the hydrogen ion from the solution (H^+). The opposite is obtained in the case of a weak M-H_{ads} bond (such as Cd-H_{ads}, Fig. 5.35). It would now be interesting to examine if the intermediate M-H_{ads} bond strength would produce a maximum in 1,4-NADH recovery somewhere between these two cases, *i.e.* between the two extreme potentials (–1.4 and –2.3 V). For that purpose, Co and Ni electrodes were tested.

Fig. 5.36 shows the corresponding results obtained using a Co electrode. The maximum in the 1,4-NADH recovery (82.0 ± 1.9 %) was indeed obtained at a slightly more negative potentials (–1.5 V) in comparison to Ti (–1.4 V). The Co-H_{ads} bond

strength is 192.6 kJ mol^{-1}, which is weaker than the Ti-H_{ads} bond strength (348.3 kJ mol^{-1}) and stronger than that of Cd-H_{ads} (119.7 kJ mol^{-1}). Consequently, a high H_{ads} surface coverage of Co could be expected at potentials more negative than that on Ti, but more positive than that on Cd. Accordingly, the kinetics of the NAD-radical protonation reaction (Step 2a, Scheme 1) could also be expected to follow the same behavior, which is indeed shown in Fig. 5.36. A decrease in the 1,4-NADH recovery at potentials more negative than –1.5 V (Fig. 5.36) is due to the increase in the HER kinetics.

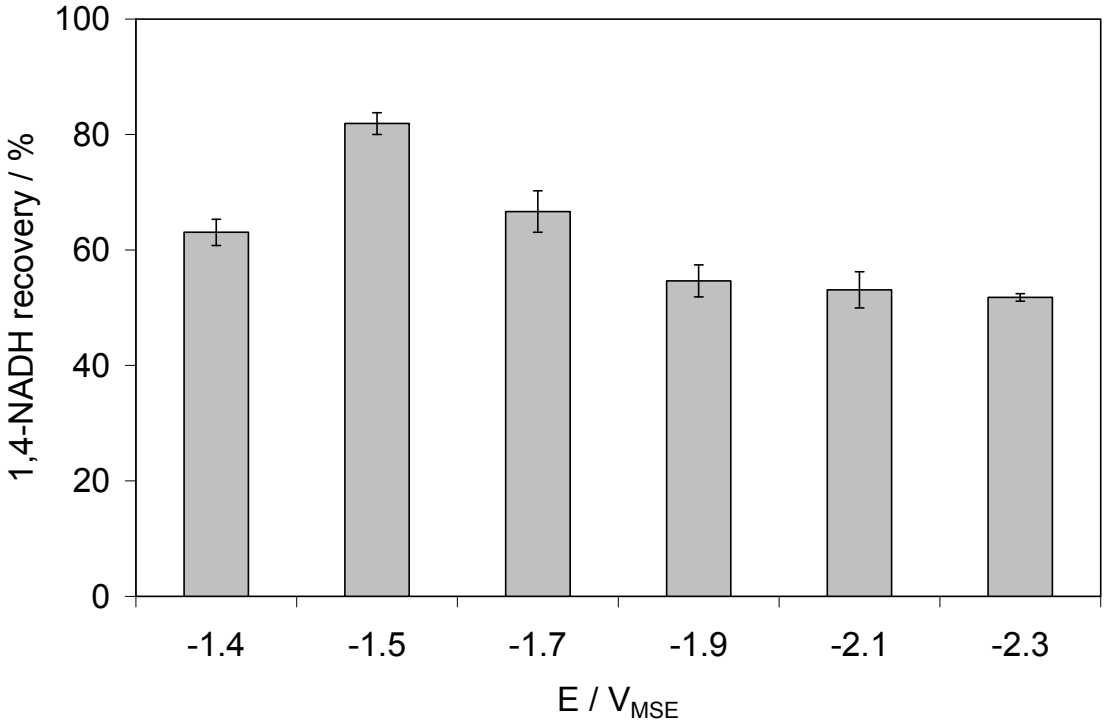

Figure 5.36: The percentage of enzymatically-active 1,4-NADH recovered on a Co electrode, obtained by reduction of 1 mM NAD^+ in a batch electrochemical reactor operating at different electrode potentials.

If we now take nickel, the Ni-H_{ads} bond strength is 195.94 kJ mol^{-1}, which is very close to the Co-H_{ads} bond strength, and thus, one can expect to see a maximum in 1,4-NADH recovery somewhere between -1.4 V and –2.3 V, as well (as actually seen in Fig. 5.37). The maximum value obtained was 92.0 ± 1.4 %. The trend in Fig. 5.37 could

be described in the same manner as those in Figs. 5.34 to 5.36, and will thus not be repeated here.

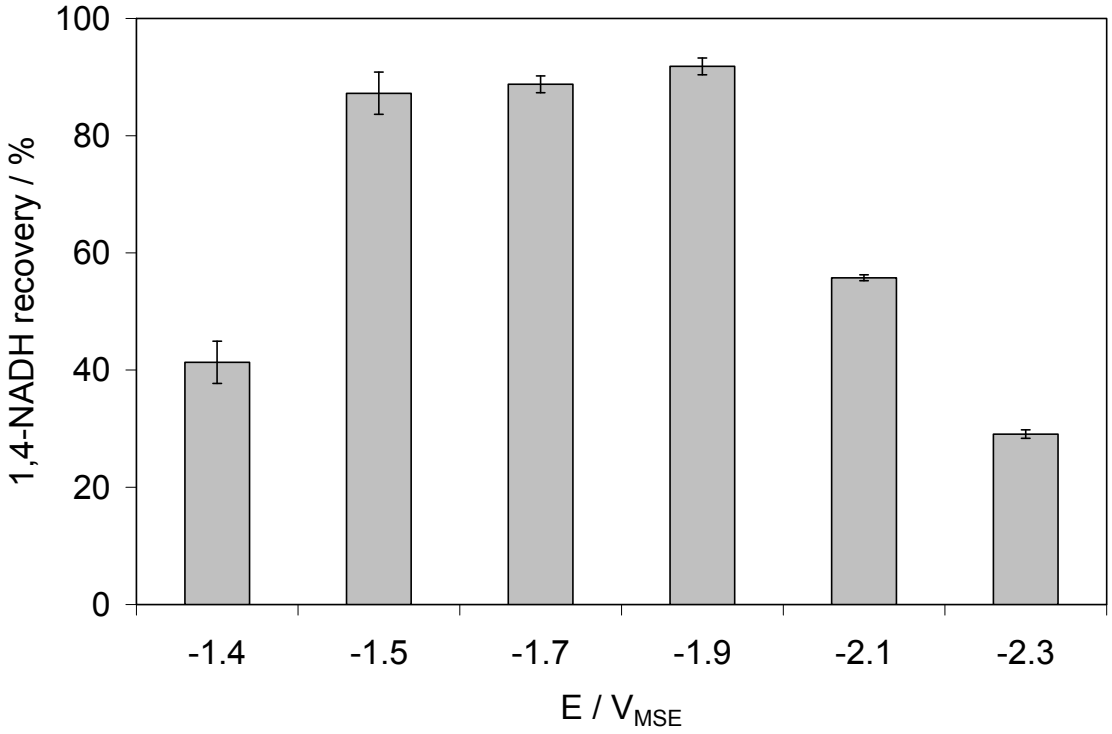

Figure 5.37: The percentage of enzymatically-active 1,4-NADH recovered on a Ni electrode, obtained by reduction of 1 mM NAD^+ in a batch electrochemical reactor operating at different electrode potentials.

The most important feature of the work presented in this thesis Section (5.3.1) is that it was demonstrated by our laboratory that a high recovery of active 1,4-NADH could be obtained on non-modified electrodes, which has not yet been reported in the literature. In addition, the effect of regeneration potential on the percentage of 1,4-NADH that can be recovered from NAD^+ was demonstrated, and the fundamental origin of the behavior observed was explained. It was shown that all electrode surfaces employed recovered more than 80% 1,4-NADH, reaching even 100% on some surfaces. No such higher recovery of 1,4-NADH has been reported on bare (non-modified) electrodes. However, since there is no published research except [28] on the influence of electrode potential on the percentage recovery of 1,4-NADH produced by electrolysis of NAD^+,

direct comparison of the data presented in this thesis, to the literature data is not quite possible. Nevertheless, some general comparison still can be made. Thus, our previous work on regeneration of 1,4-NADH on Au and Cu electrodes [28] showed that at very low cathodic potentials (–1.4 V_{MSE}), the two electrodes can produce 75 and 71% pure 1,4-NADH, respectively. On the other hand, at higher electrolysis potentials (–1.8 V_{MSE}), only 28% and 52% of 1,4-NADH was produced on Au and Cu, respectively. Other works [24] showed that when a ruthenium-modified GC electrode was used at –1.5 V_{MSE}, the product mixture contained 65% pure 1,4-NADH. At slightly higher cathodic potentials, –1.60 and –1.65 V_{MSE}, the recovery of 1,4-NADH increased to 98% and 94%, respectively, and then with the further increase in cathodic potential to –1.7 and –1.8 V_{MSE}, the percentage significantly decreased to 42% and 14%, thus giving a 'volcano-type' potential-dependant trend.

The literature survey further shows that the amount of 1,4-NADH regenerated on a platinum electrode ranges from 30 to 50% [45, 51, 127]. On mercury, it ranges from 10 to 76% [34, 38-42], a tin oxide electrode produced 10% 1,4-NADH [1], and on a reticulated vitreous carbon electrode the amount of 1,4-NADH regenerated was only 0.6% [37], while on gold-amalgam it was 10% [45]. However, the reader should note that, unfortunately, some research groups have reported amount of 1,4-NADH regenerated electrochemically, on the basis of only considering the 340 nm peak in the UV/Vis [47, 128], instead of testing the purity by the enzymatic assays. However, this peak corresponds not only to the amount of 1,4-NADH produced, but also to the presence of produced NADH isomers and the dimer, NAD_2, the latter two being enzymatically-inactive. Thus, these values cannot be trusted.

5.3.2 Electrochemical regeneration of 1,4-NADH on *modified* electrodes

It is clear from Section 5.3.1 that bare (non-modified) metal electrodes are good candidates for electrochemical regeneration of enzymatically-active 1,4-NADH. However, only GC and CNF electrodes were capable of producing the highest 1,4-NADH purity (99-100%), but at very high cathodic potentials. It would be much more economical to produce a high-purity of 1,4-NADH at lower potentials, and although the

Ti electrode was capable of producing 96% pure 1,4-NADH, for some applications of the co-enzyme, this purity is still not high enough.

Taking into account that high-purity 1,4-NADH was produced on GC and CNF electrodes only at high cathodic potentials (–2.3 V), which is due to the fact that the surface is covered with H_{ads} only at these potentials, one can hypothesize that if the GC surface is 'nano-patterned' with nano-particles (nano-islands) of a material capable of adsorbing H_{ads} easily at low cathodic potentials, the highly pure 1,4-NADH could then be produced at these low potentials. In addition, the nano-islands would serve as a physical barrier between the two neighboring NAD-radicals, and would thus minimize the probability for their dimerization. This hypothesis was already described in Chapter 3 of the thesis - see Scheme 2.

In order to test the hypothesis, a GC electrode was used as a substrate, and it was then patterned with nano-particles (NPs) of a good hydrogen evolution catalyst (Pt or Ni). As just postulated above, the role of NPs would be to adsorb hydrogen ($M\text{-}H_{ads}$) in the lower potential region of NAD^+ reduction, and this 'activated' hydrogen would then readily react with a NAD-radical adsorbed on the adjacent GC site (Scheme 2), thus minimizing the probability of the dimer formation.

In this section, results on the development and application of bi-functional GC-Pt and GC-Ni electrodes for electrocatalytic regeneration of enzymatically-active 1,4-NADH are discussed. It will be shown that when the GC electrode was patterned with Pt and Ni NPs, a 100% purity (*i.e.* recovery) of 1,4-NADH was achieved at much lower overpotential compared to GC and CNF electrodes, proving the hypothesis presented in Scheme 2. It will also be shown that the purity of 1,4-NADH recovered is dependent on the NPs surface coverage and electrode potential.

5.3.2.1 Characterization of a GC-Pt electrode

A SEM micrograph of Pt nanoparticles (NPs) deposited on a GC surface is presented in Fig. 5.38a.

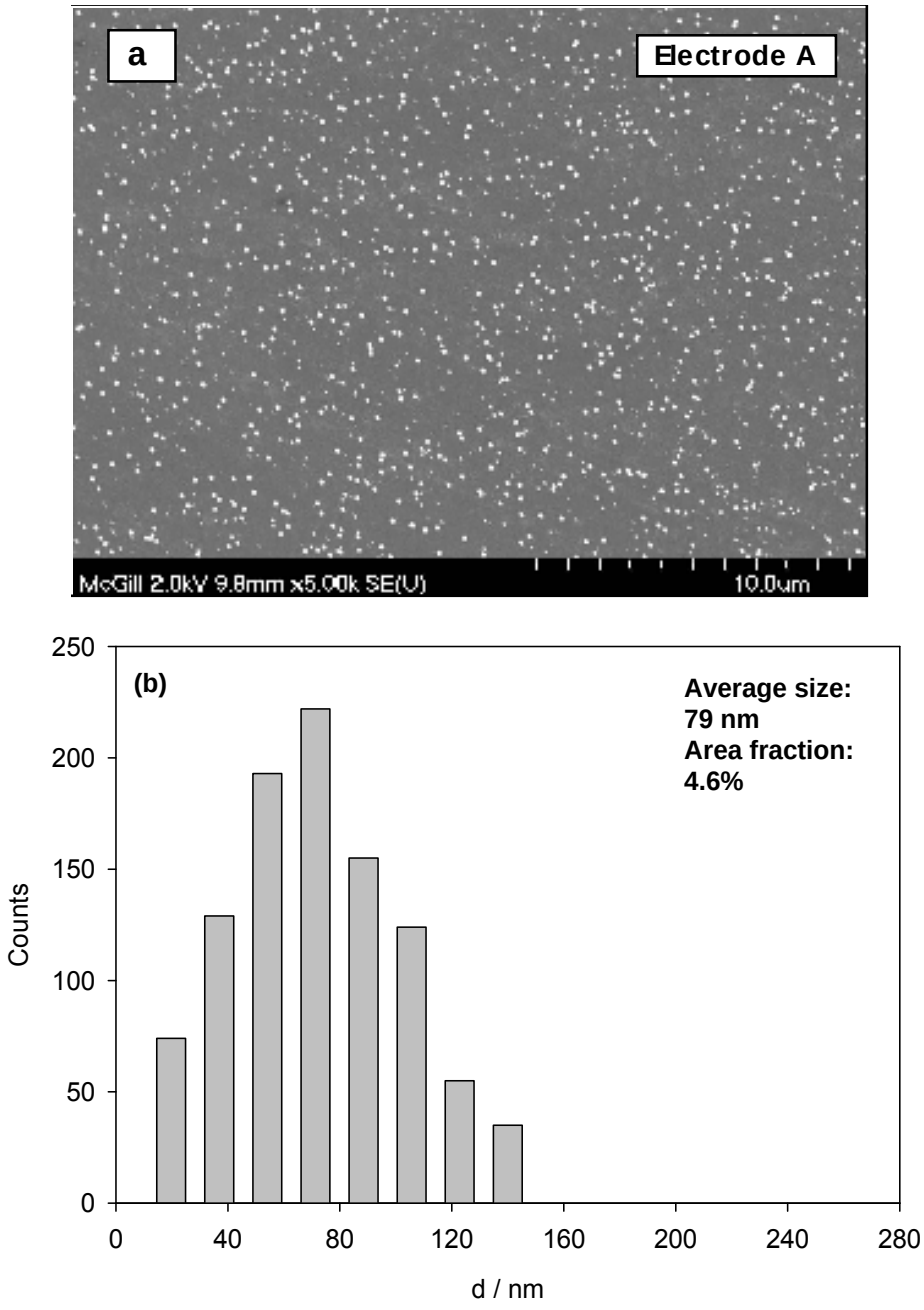

Figure 5.38: (a) A SEM micrograph of Pt NPs deposited on a freshly prepared and electrochemically activated GC electrode surface. Pt NPs were electrodeposited on the GC surface from 0.5 M H_2SO_4 containing 1 mM $H_2PtCl_6 \times 6H_2O$ by cycling the electrode from -0.6 to 0.1 V at a scan rate of 50 mV s^{-1} for 5 scans. (b) Pt NP size distribution. This electrode is termed "Electrode A", in the thesis.

The micrograph shows that the surface distribution of Pt NPs on the GC surface is uniform (EDX analysis confirmed that the NPs are indeed platinum, Fig. A. 3 in Appendix A). Only negligible agglomeration of NPs is present. The mean Pt NP size is 79 nm, and the size distribution is relatively narrow (Fig. 5.38b). It was determined that 4.6% of the GC surface is covered by Pt NPs. This electrode is termed "Electrode A", further in the thesis. Small (*i.e.* nano) Pt particle size, good physical separation and uniform surface distribution of the NPs, could lead to a highly electrocatalytically active electrode surface capable of efficiently reducing NAD^+ to 1,4-NADH, which will indeed be evidenced later in the text.

In order to characterize the electrochemical behavior of GC-Pt Electrode A, a cyclic voltammogram (CV) was recorded in 0.5 M H_2SO_4 solution in a wide potential region, between hydrogen and oxygen evolution, and presented together with the CVs of bare GC and bare Pt, in Fig. 5.39.

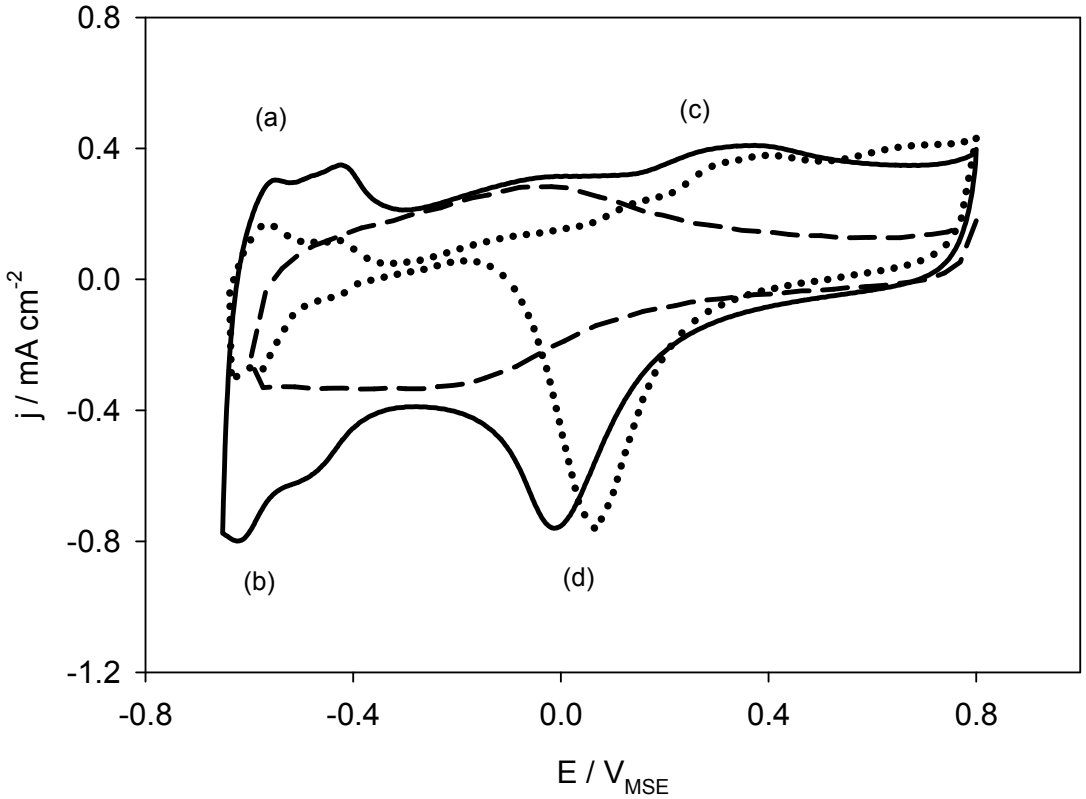

Figure 5.39: Cyclic voltammograms of the bare GC (dashed lines), bare Pt (dotted lines) and GC-Pt (solid lines) electrode recorded in 0.5 M H_2SO_4, at scan rate 100 mV s^{-1}.

The CV of the bare GC electrode (dashed lines) does not show any redox peaks in the potential region investigated, demonstrating its electrochemical inertness. On the other hand, the CV of the bare Pt electrode (dotted line) shows characteristic peaks related to hydrogen desorption and adsorption, Pt-H_{ads} (potential regions *a* and *b*, respectively) and Pt oxide film formation and reduction (potential regions *c* and *d*, respectively) [104, 129-131]. The CV of GC-Pt Electrode A (solid line) is almost the superposition of the bare GC and Pt response. Namely, it shows the characteristic hydrogen adsorption and desorption peaks (regions *a* and *b*), the Pt oxide formation and reduction peaks (regions *c* and *d*), and also an anodic 'hump' in the potential region between ca. –0.35 V and 0.1 V, the latter being a response of the GC surface. Thus, Fig. 5.39 further confirms the presence and electrochemical activity of Pt on a GC electrode surface.

In order to determine the potentiodynamic behavior of GC-Pt Electrode A in the potential region of NAD^+ reduction, a linear polarization voltammogram was recorded in the presence (solid lines) and absence (dotted lines) of NAD^+ in the supporting electrolyte, Fig. 5.40a. For comparison, the behavior of bare GC electrode under the same experimental conditions is presented as an inset to the Fig. 5.40 (Fig. 5.40b - this is the same plot as in Fig. 5.26, but is again shown here for the reader's convenience).

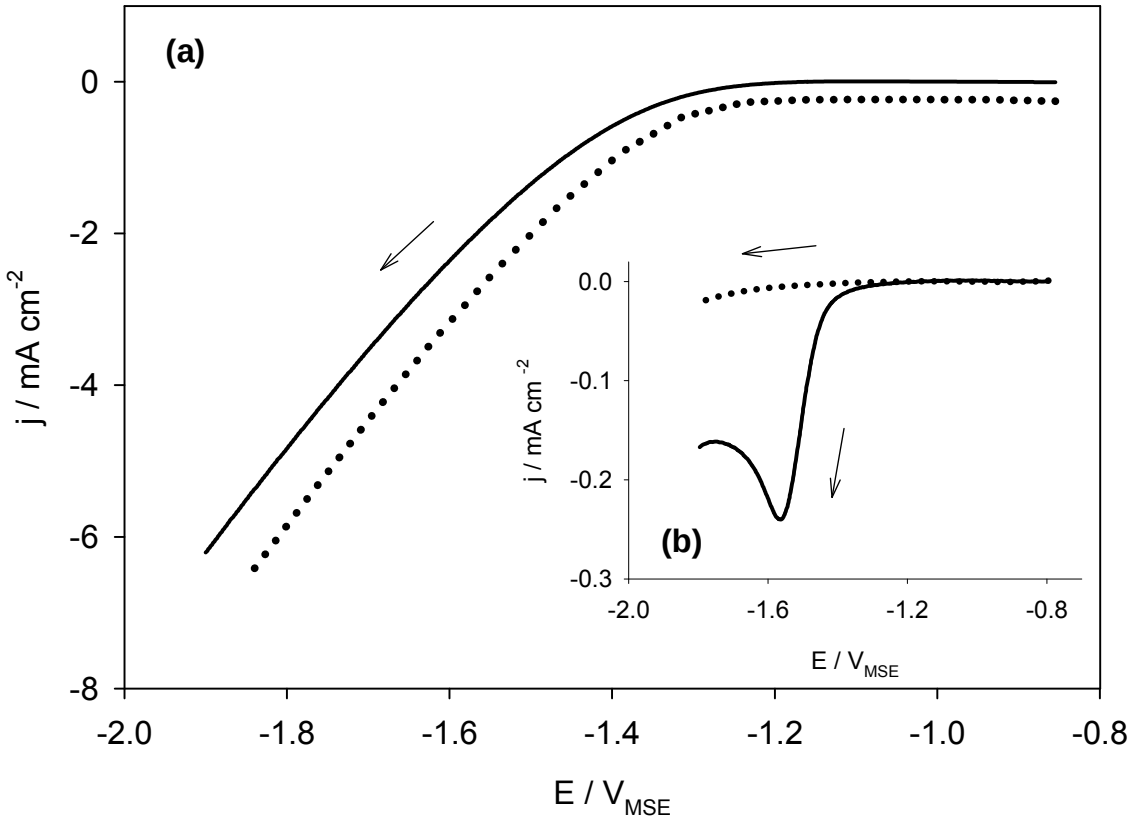

Figure 5.40: Linear polarization voltammograms of (*a*) GC-Pt and (*b*) bare GC electrode recorded in 0.1 M $NaClO_4$ (dotted line) and in 0.1 M $NaClO_4$ + 4 mM NAD^+ (solid line).

The linear polarization voltammogram of the bare GC electrode recorded in the NAD^+-containing solution (Fig. 5.40b, solid line) shows a well-defined cathodic current peak at potential ca. –1.5 V, corresponding to the reduction of NAD^+ [1, 24, 29, 38, 45, 47, 56], whereas the peak is absent in the background electrolyte (dotted line). On the other hand, no NAD^+ reduction peak was recorded on the GC-Pt electrode, and the current in the NAD^+-containing solution was lower than that in the background electrolyte (Fig. 5.40a). This was to expect since Pt is the best hydrogen evolution catalyst, and the current recorded in the potential region of NAD^+ reduction in Fig. 5.40a is the sum of the NAD^+ reduction and hydrogen evolution reaction (HER) current. The decrease in the current in the NAD^+-containing solution is due to the blockage of the electrode surface (towards the HER) by adsorbed NAD^+, and possibly also produced 1,4-NADH and NAD_2 molecules, similarly to the result on Ti (Fig. 5.33). FTIR-ATR

measurements confirmed the presence of these species on electrode surfaces, after electrolysis.

5.3.2.2 Electrochemical regeneration of 1,4- NADH on GC-Pt electrode

The first set of measurements on 1,4-NADH regeneration by GC-Pt Electrode A focused on the investigation of the influence of electrode potential on the purity of 1,4-NADH, *i.e.* the percentage of 1,4-NADH in the product mixture *recovered* from NAD^+.

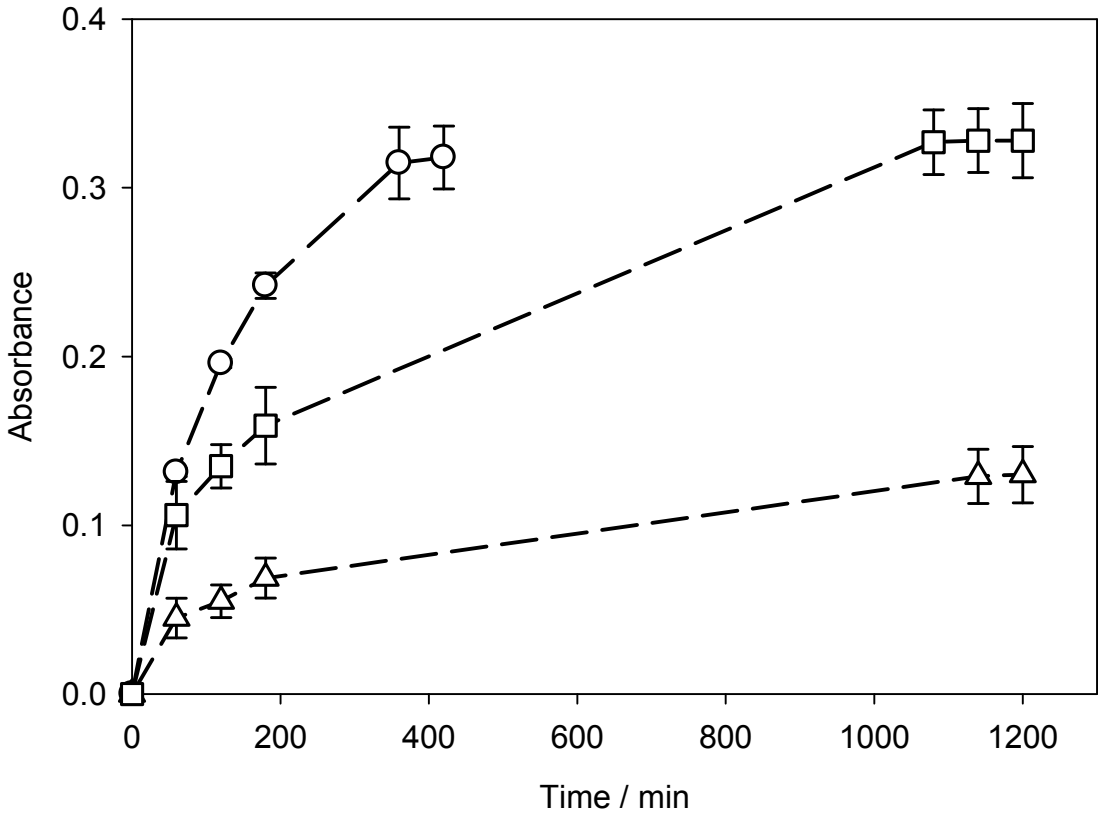

Figure 5.41: Time dependence of absorbance at 340 nm recorded during electrolysis of 1 mM NAD^+ in a batch electrochemical reactor employing GC-Pt Electrode A operated at (Δ)–1.4 V, (□)–1.5 V and (O) –1.6 V.

Fig. 5.41 shows the time evolution of absorbance at 340 nm at selected electrode potentials. At a low NAD^+ reduction potential, –1.4 V (triangles), the conversion of NAD^+ (to NAD_2 and/or 1,4-NADH, Scheme 1) is rather slow and an absorbance plateau

is reached after ca. 20 h of electrolysis. However, with an increase in potential from –1.4 to –1.5 V (squares) and to –1.6 V (circles), the rate of NAD^+ reduction also increases and a plateau is reached after ca. 18 h and 6 h, respectively. Also, the final absorbance values at the latter two potentials, and thus the final (equilibrium) NAD_2 and 1,4-NADH concentrations produced, are higher than at –1.4 V, which is in accordance with conditions of electrochemical equilibrium [36]. Based on these results it could be concluded that the kinetics of the NAD^+ reduction reaction increases with an increase in electrode potential to more negative values, similarly to the results on GC (Fig. 5.27).

As mentioned before in the thesis that the absorption peak at 340 nm corresponds to the response of NAD_2 and various NADH isomers. Thus, to determine the percentage of enzymatically-active 1,4-NADH in the product mixture, it was necessary to perform the activity assay, as explained in Section 4.7 [123].

At an electrolysis potential of –1.4 V, the percentage of enzymatically-active 1,4-NADH recovered from NAD^+ on GC-Pt Electrode A was found to be 65.0 ± 1.9%. In comparison, only 32.0 ± 0.02% of enzymatically-active 1,4-NADH was recovered on bare GC electrode under the same experimental conditions (Fig. 5.28) [36]. Thus, the patterning of a GC surface by Pt NPs (Fig. 5.38(a)) resulted doubling the purity of 1,4-NADH regenerated in comparison to the bare GC electrode surface.

It was shown in Section 5.3.1 that the percentage of enzymatically-active 1,4-NADH recovered by reduction of NAD^+ strongly depends on electrode potential. To investigate the effect of electrode potential on the recovery of 1,4-NADH using GC-Pt Electrode A, electrolysis experiments were also performed at potentials negative of –1.4 V, and the corresponding results are presented in Fig. 5.42.

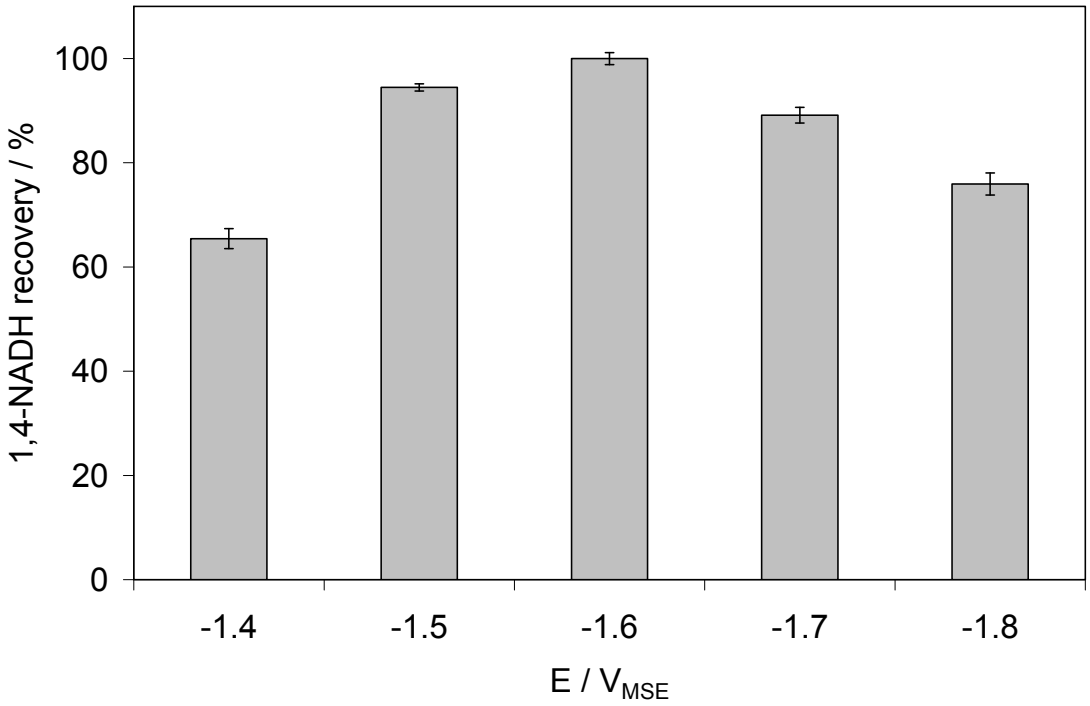

Figure 5.42: The percentage recovery of enzymatically-active 1,4-NADH from NAD^+ on GC-Pt Electrode A (Fig. 5.38), obtained by reduction of 1 mM NAD^+ in a batch electrochemical reactor operating at different electrode potentials.

The results demonstrate that by increasing the electrode potential from –1.4 V to –1.5 V, a significant increase in the percentage of recovered 1,4-NADH was obtained, from 65.0 ± 1.9 % to 95.0 ± 0.7 %, respectively. A further, increase in electrode potential to –1.6 V resulted in even further increase in the 1,4-NADH recovery to 100 %. These experiments prove the hypothesis on the role of Pt NPs on the GC surface as the hydrogen protonation (adsorption, Pt-H_{ads}) sites, as outlined in the objective section (Scheme 2).

However, a further increase in electrode potential from –1.6 V to –1.7 V and then to –1.8 V resulted in a decrease in the percentage of active 1,4-NADH recovered, to 89.0 ± 1.5 % and 76.0 ± 2.1 %, respectively, Fig. 5.42. The trend in Fig. 5.42, *i.e.* the presence of a 1,4-NADH recovery maximum, could be explained by considering both the mechanism of NAD^+ reduction reaction (Scheme 1) and the activity of Pt in the hydrogen evolution reaction (HER, Eq. 5.20). As explained earlier, protonation of a NAD-radical is considered to be kinetically slower than the dimerization of two neighboring radicals

(Scheme 1), resulting in the production of an enzymatically-inactive NAD_2 dimer. Hence, to increase the kinetics of the protonation (Step 2a, Scheme 1), it is preferable to provide (adsorb) hydrogen very close to the site of NAD-radical formation (Scheme 2). The higher the hydrogen (H_{ads}) surface coverage, the higher the probability the surface-adsorbed NAD-radical will be protonated, thus producing enzymatically-active 1,4-NADH. For example on GC electrode surface, with an increase in electrode potential to more negative values, the electrode surface coverage by adsorbed hydrogen also increases [36]. In addition, the increase in electrode potential to more negative values also enhances the rate of electron transfer to both NAD^+ and NAD-radical (Scheme 1). Consequently, one could expect to also see an increase in the recovery of 1,4-NADH formed, which was indeed observed on a bare GC electrode (Fig. 5.28) [36]. However, Fig. 5.42 does not follow this trend, but shows a presence of a maximum at –1.6 V, obviously caused by the presence of Pt NPs on the GC surface. It is well known that Pt is the best hydrogen evolution catalyst, which form a Pt-H_{ads} bond of an *intermediate* strength, 251.2 kJ mol^{-1} (which lays between that of Ti and of Cd) [125]. Taking this into account and the explanation for the behavior of Ti and Cd electrodes outlined in Section 5.3.1.3 and 5.3.1.4, respectively, one can easily deduce the origin of the behavior of the GC-Pt electrode presented in Fig. 5.42.

Hence, with an increase in electrode potential from –1.4 V to –1.6 V (Fig. 5.42) the coverage of Pt NPs by adsorbed hydrogen (Pt-H_{ads}) increases (Eq. 5.18), while the second HER step, the production of molecular hydrogen (Eqs. 5.19 and/or 5.20), is still a slow step on Pt NPs at these low cathodic potentials (relative to the kinetics of the first step). Thus, in accordance with Scheme 1, the kinetics of the NAD-radical protonation (Step 2a, Scheme 1) also improves with an increase in the surface coverage of H_{ads}, producing an increase in the percentage of enzymatically-active 1,4-NADH recovered from NAD^+, as opposed to the percentage of enzymatically-inactive dimer NAD_2 (Fig. 5.42). However, the further increase in electrode potential from –1.6 V to –1.8 V favors the kinetics of the second HER step, corresponding to the production of molecular hydrogen from Pt-H_{ads} (Eqs. 5.19 and/or 5.20) [125], thus diminishing the amount of H_{ads} available for the NAD-radical protonation reaction. Consequently, the recovery of 1,4-NADH decreases (Fig. 5.42).

Therefore, –1.6 V appears to be an optimum electrode potential for the regeneration of enzymatically-active 1,4-NADH from NAD^+ under the experimental conditions employed, giving a 100% recovery. For comparison, literature shows that reduction of NAD^+ on a gold-amalgam unmodified electrode gave only ca. 10% enzymatically-active 1,4-NADH, a bare gold electrode gave 30% of active 1,4-NADH [29], while the amount of active 1,4-NADH increased to 50% and 75% when an unmodified platinum and a cholesterol-modified gold-amalgam electrode were used [45]. When a GC electrode was modified by Au, the conversion of NAD^+ to active 1,4-NADH was 67% [47]. Furthermore, our laboratory's previous results show that when a GC electrode was modified with Ru NPs, the recovery of 1,4-NADH achieved was 98% [24]. Thus, it appears that the Pt-nano-patterned GC electrode offers so far the highest electrocatalytic activity in the conversion of NAD^+ to 1,4-NADH at low cathodic potentials, effectively enabling a 100% recovery.

5.3.2.3 Influence of Pt NPs surface coverage and size

To investigate the influence of Pt NPs surface coverage and size on the percentage recovery of 1,4-NADH, three different GC-Pt electrodes were produced, Fig. 5.38 (Electrode A) and Fig. 5.43 (Electrodes B and C).

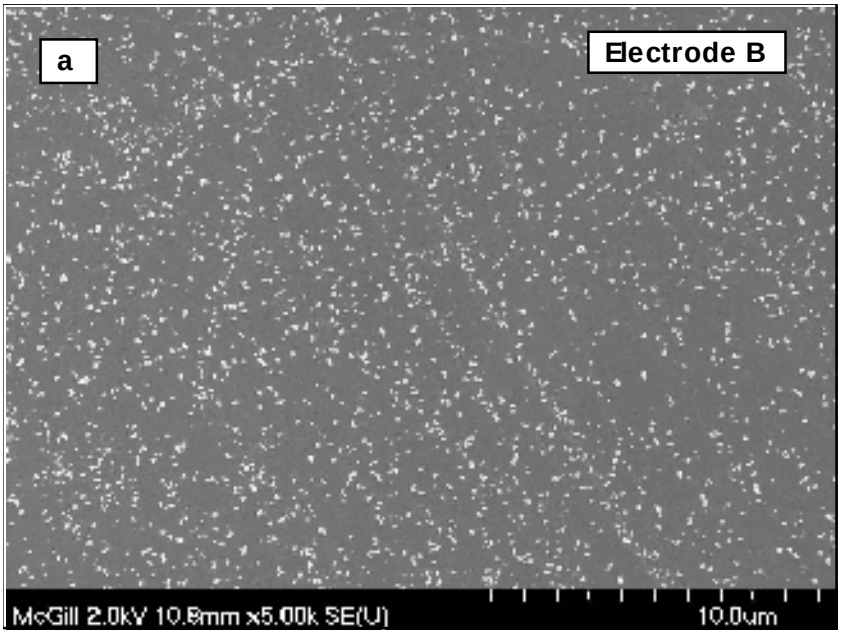

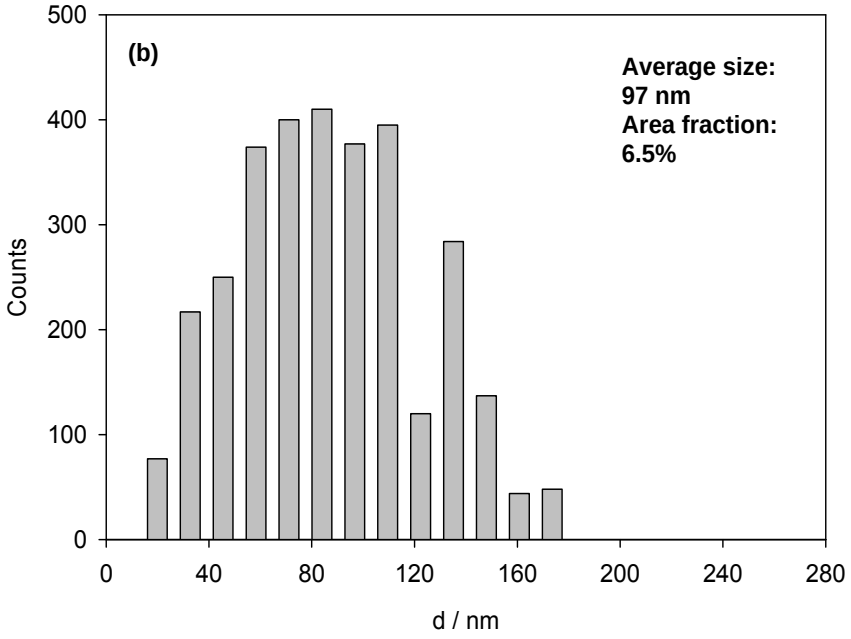
(b)
Average size:
97 nm
Area fraction:
6.5%
Counts
d / nm
0
100
200
300
400
500
0
40
80
120
160
200
240
280

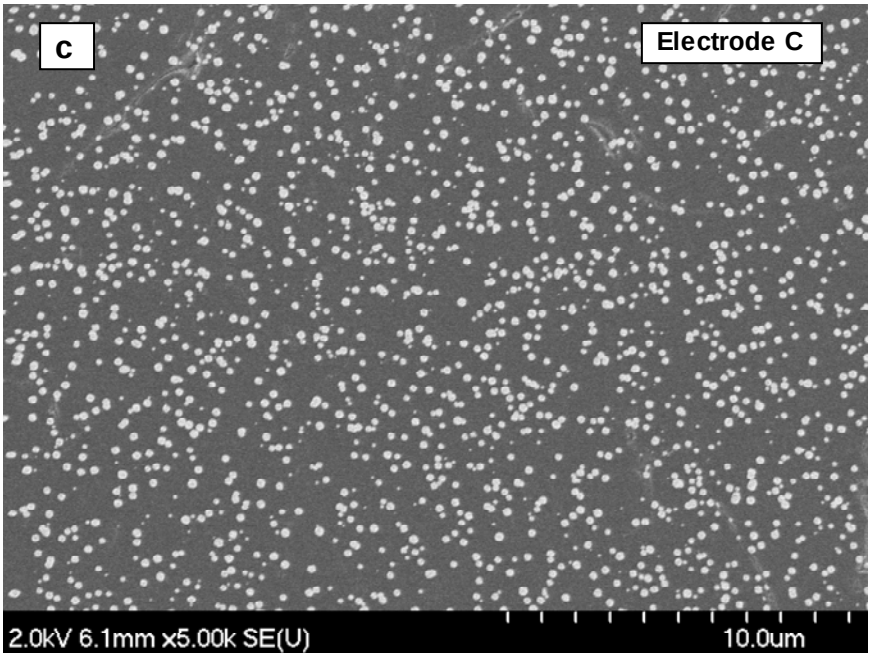
C
Electrode C
2.0kV 6.1mm x5.00k SE(U)
10.0um

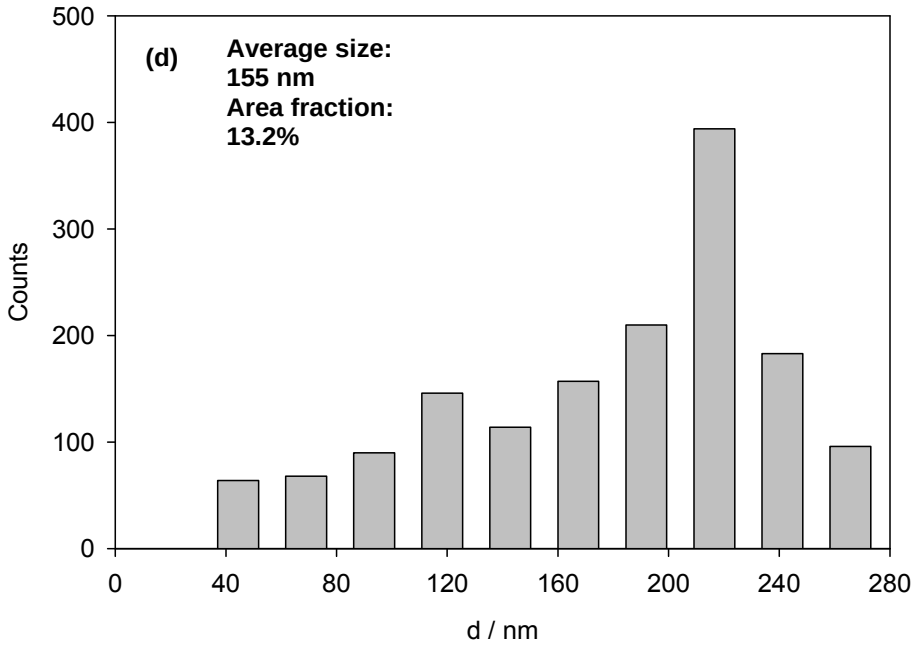

Figure 5.43: (*a,c*) SEM micrographs of GC electrodes patterned with Pt NPs of different size and surface coverage. Pt NPs were electrodeposited on the GC surface from 0.5 M H_2SO_4 containing 1 mM $PtHCl_6$ by cycling the electrode in a potential range from –0.6 to 0.1 V at a scan rate of 50 mV s^{-1} for 10 scans (Electrode B) and 20 scans (Electrode C). Plots (*b*) and (*d*) show the corresponding Pt NPs size distribution, respectively.

The micrograph and Pt NPs size distribution for Electrode A (Fig. 5.38), which was prepared by employing 5 potential polarization cycles. However, doubling the number of potential polarization cycles, from 5 to 10, resulted in the formation of bigger Pt NPs, characterized by a mean particle size of 97 nm and higher Pt surface coverage, 6.5%, as shown in Figs. 5.43a and 5.43b, respectively (Electrode B). Here, NPs are not spherical in shape, but rather represent agglomerates of a few smaller NPs. In addition, the NP size distribution is wider than on the surface of Electrode A (Fig. 5.38b). A further increase in number of potential polarization cycles from 10 to 20 resulted in a further increase in the Pt NPs size and surface coverage, yielding a mean NP size of 155 nm and a 13.2% surface coverage, Figs. 5.43c and 5.43d, respectively (Electrode C). Also, the NP size distribution has further widened in comparison to Electrode A (Fig. 5.38b) and Electrode B (Fig. 5.43b), especially in the lower NP diameter range, suggesting a significant degree of NP agglomeration.

As documented earlier, the highest recovery (100%) of enzymatically-active 1,4-NADH with Electrode A was obtained at an electrode potential of –1.6 V, Fig. 5.42. Therefore, the electrocatalytic activities of Electrodes B and C in 1,4-NADH regeneration, were tested at the same electrode potential and the results are presented in Fig. 5.44.

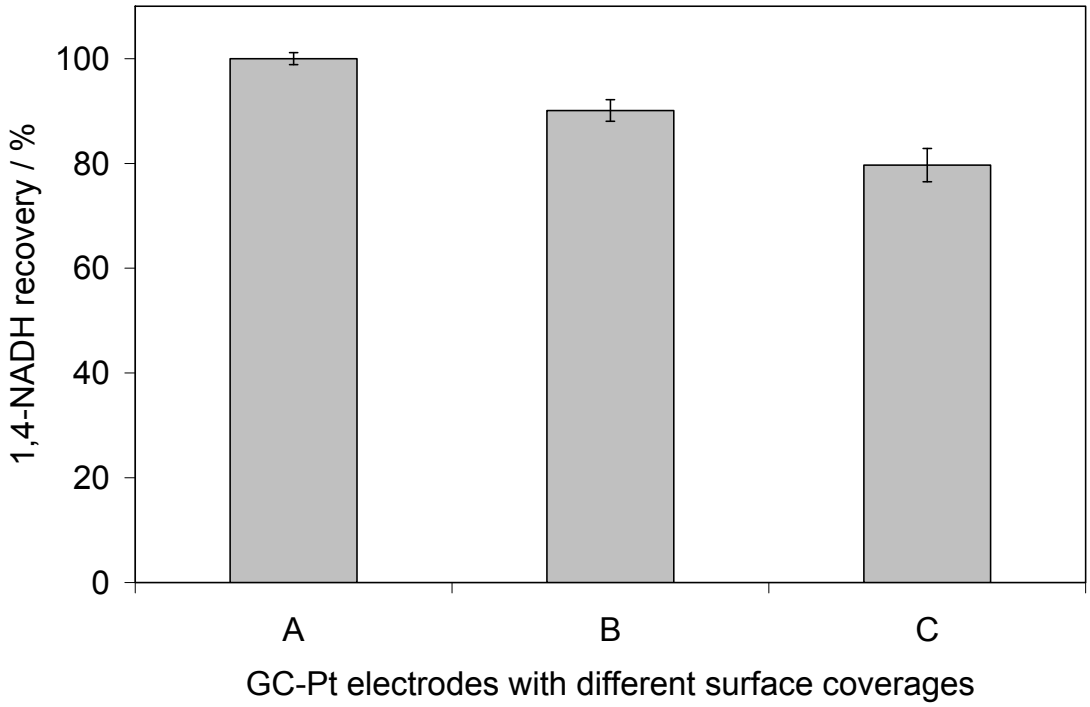

Figure 5.44: The percentage (purity) of enzymatically-active 1,4-NADH recovered from NAD^+ on GC-Pt electrodes with different Pt NP size and surface coverage (Figs 5.38 and 5.43), by reduction of 1 mM NAD^+ in a batch electrochemical reactor at a potential of –1.6 V.

It is clear from the Fig. 5.44 that Electrode A shows the highest catalytic activity towards regeneration of enzymatically-active 1,4-NADH, producing a 100% pure 1,4-NADH. On the other hand, Electrodes B and C enabled the formation of the product mixture (*i.e.* the recovery) containing 90% and 80% of 1,4-NADH, respectively. A possible reason for the higher recovery of enzymatically-active 1,4-NADH on Electrode A is a smaller size and narrower size distribution of Pt NPs on the GC surface (Fig. 5.38). Namely, with an increase in Pt NP size, the probability that the hydrogen adsorbed on the Pt surface, far from the Pt/GC interface, is used for protonation of the NAD-radical

decreases, while the probability for production of molecular hydrogen increases. Thus, with the increase in distance from the Pt/GC interface to the Pt NP center, the ratio of hydrogen (H_{ads}) used for NAD-radical protonation decreases, and thus the percentage of 1,4-NADH recovered from NAD^+ decreases.

Although the very high cost of 1,4-NADH can justify the use of expensive Pt at the surface coverage relevant to that on Electrode A (Fig. 5.38), it would be beneficial if Pt was replaced by a less expensive metal, while still achieving the high (preferably 100%) 1,4-NADH recovery. Considering the hypothesis postulated in the objective of the thesis (Scheme 2), *i.e.* the idea of providing "active" (*i.e.* electrode-adsorbed) hydrogen, M-H_{ads}, for the NAD-radical protonation by nano-patterning a GC surface with a good hydrogen evolution catalyst, an attempt of replacing Pt by Ni was made. The rationale for choosing Ni is that, (i) this metal form the Ni-H_{ads} bond of intermediate strength, 195.9 kJ mol^{-1}, which is close to that of Pt-H_{ads}, (ii) it thus has the highest hydrogen evolution electrocatalytic activity among non-noble metals [125], (iii) it is considerably cheaper than Pt, (iv) it is much more abundant, and (v) it is stable in a neutral media in the potential region of 1,4-NADH regeneration.

5.3.2.4 Characterization of GC-Ni electrode

Patterning of a GC surface by Ni NPs was done by cyclic voltammetry, as described in the experimental part of the thesis, and an example of the GC-Ni electrode surface is presented in Fig. 5.45, together with the Ni NP size distribution.

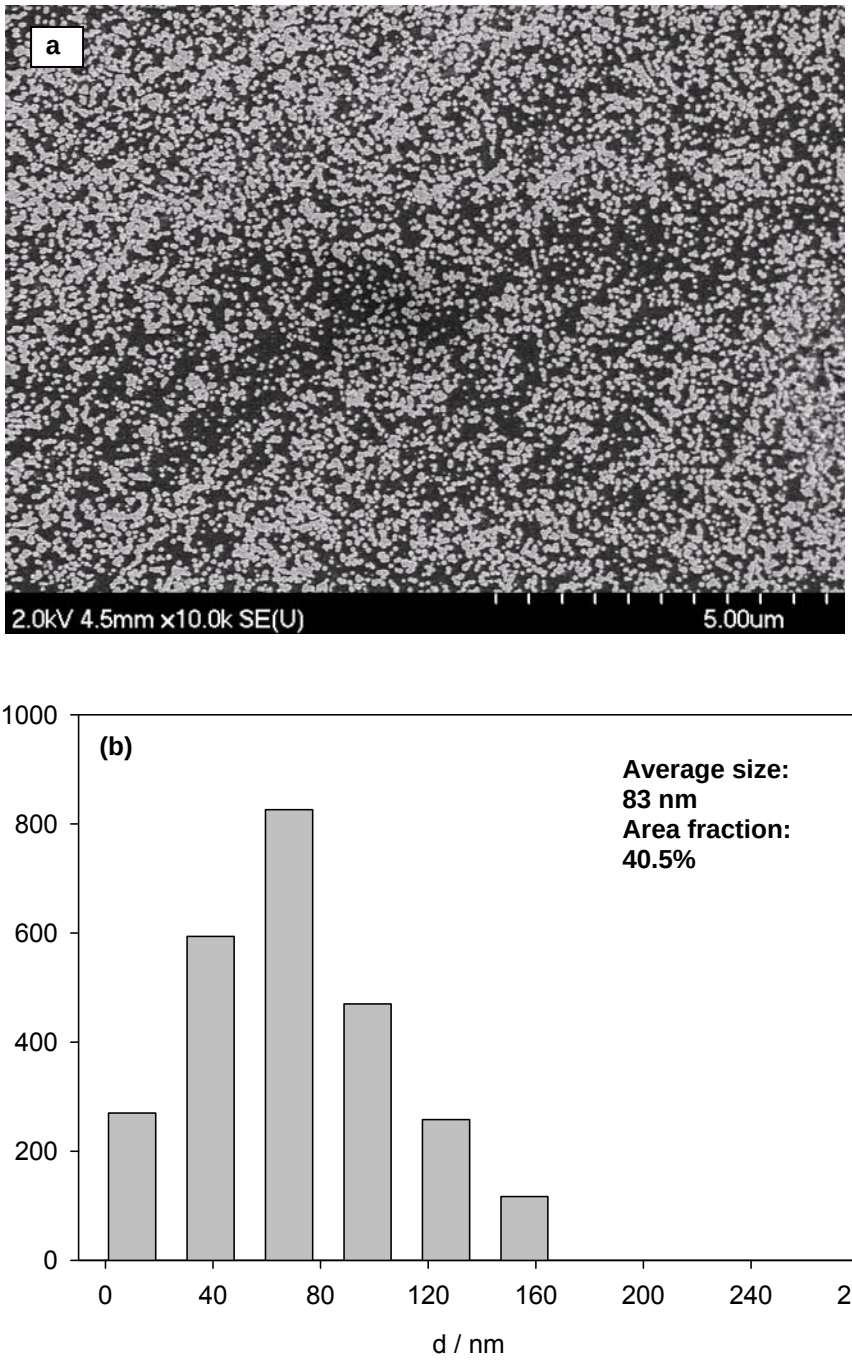

Figure 5.45: (a) A SEM micrograph of Ni NPs deposited on a freshly prepared and electrochemically activated GC electrode surface. Ni NPs were electrodeposited on the GC surface from 2 mM nickel (II) nitrate hexahydrate in acetate buffer pH 4, by cycling the electrode in the potential range from –0.8 V to 0 V, at a scan rate of 50 mV s^{-1}, for 10 cycles. (b) Ni NP size distribution.

The micrograph demonstrates that a good Ni NPs surface coverage and uniform NP distribution was achieved. The mean particle size is 83 nm and the size distribution is

relatively narrow, while the achieved surface coverage is 40.5%. Despite the large Ni NP surface coverage, it will be demonstrated further in the text that the GC-Ni electrode shown in Fig. 5.45 is an extremely efficient 1,4-NADH regeneration electrode. Furthermore, to the best of the author's knowledge, the results in Fig. 5.45 represent the smallest Ni NP size, the narrowest NP size distribution, and the most uniform Ni NP electrode surface coverage reported in the literature, on the formation of Ni NP on an electrode surface by electrodeposition [82, 132-135].

5.3.2.5 Electrochemical regeneration of 1,4- NADH on GC-Ni electrode

Electrocatalytic activity of the GC-Ni electrode in 1,4-NADH regeneration from NAD^+ was investigated as a function of electrode potential in a batch electrochemical reactor, under the same experimental conditions used in Fig. 5.42 with GC-Pt Electrode A, and the results are presented in Fig. 5.46.

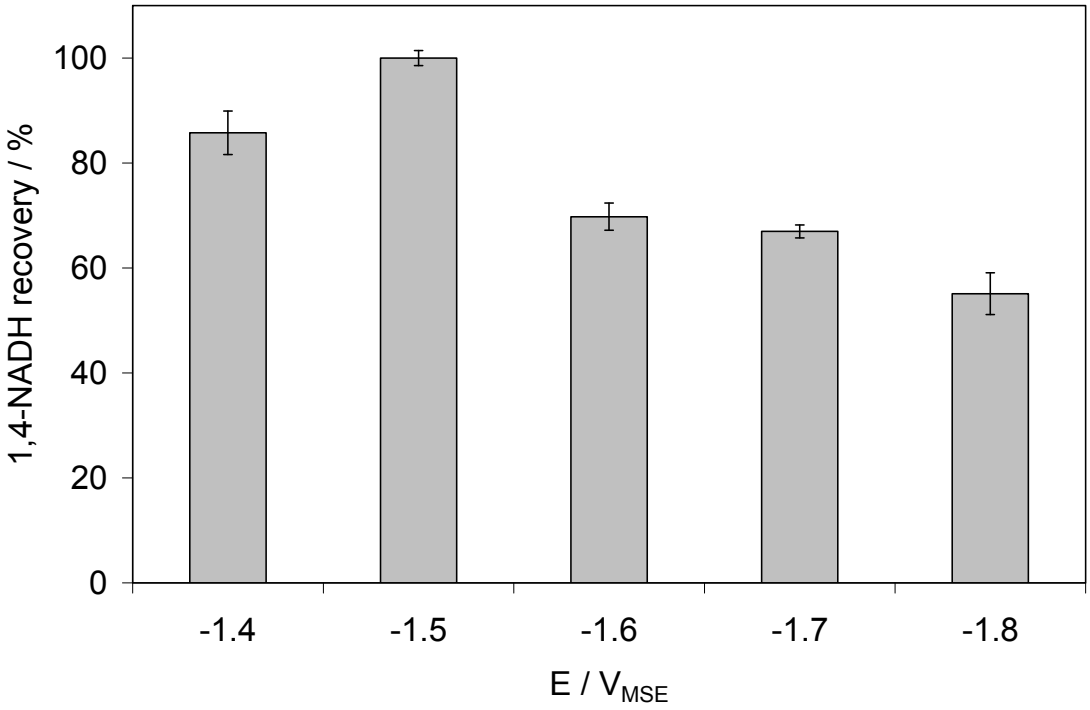

Figure 5.46: The percentage recovery of enzymatically-active 1,4-NADH from NAD^+ on a GC-Ni electrode from Fig. 5.45, by reduction of 1 mM NAD^+ in a batch electrochemical reactor operating at different electrode potentials.

The trend in the Fig. 5.46 is very similar to that one in Fig. 5.42, characterized first by an increase in the percentage of recovered 1,4-NADH with an increase in electrode potential, followed by a decrease in the former. Given that the mechanism of hydrogen reduction on Ni is similar to that on Pt, the trend in Fig. 5.46 can be explained in the same way as that one in Fig. 5.42. However, the surprising discovery was that the GC-Ni electrode was capable of enabling a 100% recovery of 1,4-NADH, and this was possible at an even more positive potential (–1.5 V) than on GC-Pt Electrode A (Fig. 5.42).

In conclusion, considering the energy input (which here is the electrode potential), the cost of the electrode, and the percentage of recovery of 1,4-NADH, the GC-Ni electrode (Fig. 5.46) appears to be the electrode of choice for 1,4-NADH regeneration among all electrodes presented here (GC, CNF, Ti, Co, Cd, Ni, GC-Pt and GC-Ni). In fact, the author of the thesis hypothesize that the CNF electrode 'decorated' by Ni NPs would be the best choice, since this electrode would also offer a much higher electrochemically active surface area than the two-dimensional GC-Ni electrode, thus enabling much faster 1,4-NADH regeneration kinetics. However, this hypothesis is left to be tested for future work on the project.

CHAPTER 6: CONCLUSIONS

6. CONCLUSIONS

This PhD project focused on the development of electrodes for the *direct* (non-mediated) electrocatalytic regeneration of enzymatically-active 1,4-NADH that would enable high regeneration efficiency and selectivity, be stable and cost effective. First, fundamental aspects of the mechanisms and kinetics of the NAD^+ reduction reaction and NAD^+ adsorption on a bare glassy carbon electrode were investigated. Second, the influence of electrode potential and electrode material on the purity of regenerated 1,4-NADH was investigated. And third, the influence of functionalization of a glassy carbon electrode with nano-islands (nano-particles) of Pt and Ni on the purity of 1,4-NADH regenerated was investigated.

These are the main conclusions that could be drawn from the work:

i. LV, DPV and EIS measurements were used to evaluate the kinetics of NAD^+ reduction reaction on a GC electrode. A very good agreement among results produced by the three techniques was demonstrated. It was found that the NAD^+ reduction reaction is:

(a) first order with respect to NAD^+,

(b) irreversible, and

(c) mass-transport controlled.

ii. The NAD^+ reduction on GC under the potentiodynamic polarization conditions in the potential region of LV and DPV current peaks results in the formation of both 1,4-NADH (60mol %) and NAD_2 (40mol %).

iii. The kinetics of reduction of NAD^+ on GC at a *formal* potential of the NAD^+/NADH couple (–0.885 V) is rather slow, and only moderately temperature dependent.

iv. NAD^+ adsorbs on a GC electrode surface in the electrochemical double-layer region. The adsorption process can be described by the Langmuir isotherm. The corresponding Gibbs energy of adsorption evidences that the adsorption process is highly spontaneous.

v. The regeneration of 1,4-NADH from NAD^+ in a batch electrochemical reactor employing non-modified electrodes (GC, CNFs, Ti, Ni, Co and Cd) is feasible. The purity (recovery) of 1,4-NADH regenerated on these electrodes is highly potential- and material-dependant, and it can go to 100% on GC and CNFs polarized at a high cathodic potential. The origin of the material/potential dependency can be related to the strength of the metal-hydrogen ($M\text{-}H_{ads}$) bond, and thus to the potential dependence of the H_{ads} electrode surface coverage.

vi. The purity of 1,4-NADH that can be regenerated from NAD^+ at *low* cathodic potentials can be increases to 100% by nano-patterning of a GC surface with Pt and Ni, to produce bi-functional GC-Pt and GC-Ni electrodes.

vii. Considering the energy input, the cost of the electrode, and the percentage of recovery (purity) of 1,4-NADH, the GC-Ni electrode is the electrode of choice for 1,4-NADH regeneration among all electrodes investigated.

CHAPTER 7: ORIGIONAL CONTRIBUTIONS

7. ORIGIONAL CONTRIBUTIONS

Nicotinamide adenine dinucleotide 1,4-NADH is a cofactor used in several hundred redox enzymatic reactions. However due to it's extremely high cost, it is currently used only in a limited number of processes. Hence, there is a need to develop *in-situ* 1,4-NADH regeneration methods for different possible industrial processes, biosensors and biofuel cells. For this purpose, new electrodes that enable the production of high-purity 1,4-NADH need to be developed. This was the main objective of this thesis project.

The following are the original contributions of this work:

1. Discovery of the influence of electrode potential on the mechanisms of NAD^+ reduction reaction, *i.e.* on selectivity of the electrocatalytic process in producing pure 1,4-NADH.
2. Establishment of the relationship between the strength of the metal electrode-hydrogen bond ($M\text{-}H_{ads}$) and the purity of 1,4-NADH regenerated from NAD^+.
3. Development of a CNFs cathode capable of producing 100% pure 1,4-NADH from NAD^+, at an increase reaction rate.
4. Development of bi-functional GC-M (GC = glassy carbon, M = Pt, Ni nano-particles) electrodes capable of producing 100% pure 1,4-NADH, and the establishment of the role of "M" in the NAD^+ reduction reaction.

CHAPTER 8: SUGGESTIONS FOR FUTURE WORK

8. SUGGESTIONS FOR FUTURE WORK

In this work bifunctional (nano-patterned) GC-Pt and GC-Ni electrodes were developed for the *direct* electrocatalytic regeneration of enzymatically-active 1,4-NADH. The work is of both fundamental and practical importance. The following fundamental and applied research could be done in the future:

1. Investigation of the efficiency of developed bifunctional electrodes in a real biochemical reactor for a prolonged time.
2. Deposition of Ni nanoparticles on CNFs to investigate the kinetics of NAD^+ reduction reaction and the amount of enzymatically-active 1,4-NADH produced.
3. Modification of GC electrode surface with nano island of other metals (Ir, Rh) in order to regenerate enzymatically-active 1,4-NADH.
4. Optimization of the Ni nanoparticles surface coverage for other industrially important hydrogenation reactions.

REFERENCES

REFERENCES

[1] Y.H. Kim, Y.J. Yoo, *Enzyme. Microb. Technol*., 44 (2009) 129.

[2] A. Liese, K. Seelbach, C. Wandrey, *Industrial Biotransformations*, Wiley-VCH, Weinheim (2006).

[3] B.A. Deore, M.S. Freund, *Chem. Mater,* 17 (2005) 2918.

[4] A.A. Karyakin, Y.N. Ivanova, E.E. Karyakina, *Electrochem. Commun*., 5 (2003) 677.

[5] M. Musameh, J. Wang, A. Merkoci, Y. Lin, *Electrochem. Commun.*, 4 (2002) 743.

[6] A. Schmid, J.S. Dordick, B. Hauer, A. Kiener, M. Wubbolts, B. Witholt, *Nature*, 409 (2001) 258.

[7] E.A. Magel, C. Hillinger, T. Wagner, W. Holl, *Phytochemistry*, 57 (2001) 1061.

[8] S. Mazzini, R. Mondelli, E. Ragg, L. Scaglioni, *J. Chem. Soc., Perkin Trans. 2,* (1995) 285.

[9] K. Shibata, S. Toda, *Biosci., Biotechnol., Biochem.,* 58 (1994) 1757.

[10] A.M. Klibanov, A.V. Puglisi, *Biotechnol. Lett.,* 2 (1980) 445.

[11] V. Somasundaram, L. Philip, S.M. Bhallamudi, *Chem. Eng. J.,* 171 (2011) 572.

[12] Z.H. Huang, M. Liu, B.G. Wang, Y.P. Zhang, Z.A. Cao, G. G. Xuebao, *CJPE,* 6 (2006) 1011.

[13] S.H. Lee, J. Ryu, D.H. Nam, C.B. Park, *Chem. Commun.,* 47 (2011) 4643.

[14] A.A. Sauve, *J. Pharmacol. Exp. Ther*., 324 (2008) 883.

[15] N. Pollak, C. Dolle, M. Ziegler, *Biochem. J.*, 402 (2007) 205.

[16] A.C. Pereira, M.R. Aguiar, A. Kisner, D.V. Macedo, L.T. Kubota, *Sens. Actuators*, B, 124 (2007) 269.

[17] P. Belenky, K.L. Bogan, C. Brenner, *Trends Biochem. Sci*., 32 (2007) 12.

[18] K. Delecouls-Servat, A. Bergel, R. Basseguy, *Bioprocess Biosyst. Eng*., 26 (2004) 205.

[19] A. Rongvaux, F. Andris, F. Van Gool, O. Leo, *BioEssays*, 25 (2003) 683.

[20] R.A. van Santen, P.W.N.M. van Leeuwen, J.A. Moulijn, B.A. Averill, *Catalysis: An Integrated Approach*, Elsevier, Amsterdam (1999).

[21] R. Devaux-Basseguy, A. Bergel, M. Comtat, *Enzyme. Microb. Technol*., 20 (1997) 248.

[22] F. Pariente, F. Tobalina, M. Darder, E. Lorenzo, H.D. Abruna, *Anal. Chem*., 68 (1996) 3135.

[23] H.K. Chenault, G.M. Whitesides, *Appl. Biochem. Biotechnol.,* 14 (1987) 147.

[24] A. Azem, F. Man, S. Omanovic, *J. Mol. Catal. A: Chem*., 219 (2004) 283.

[25] W. Liu, P. Wang, *Biotechnol. Adv.,* 25 (2007) 369.

[26] W.A. van der Donk, H. Zhao, *Curr. Opin. Biotechnol.,*14 (2003) 421.

[27] M.D. Leonida, *Curr. Med. Chem.,* 8 (2001) 345.

[28] A. Damian, K. Maloo, S. Omanovic, *Chem. Biochem. Eng*. Q., 21 (2007) 21.

[29] A. Damian, S. Omanovic, *J. Mol. Catal. A: Chem*., 253 (2006) 222.

[30] F. Man, S. Omanovic, *J. Electroanal. Chem*., 568 (2004) 301.

[31] J. Moiroux, S. Deycard, T. Malinski, *J. Electroanal. Chem*., 194 (1985) 99.

[32] P.J. Elving, W.T. Bresnahan, J. Moiroux, Z. Samec, *Bioelectrochem. Bioenerg*., 9 (1982) 365.

[33] K. Takamura, A. Mori, F. Kusu, *Bioelectrochem. Bioenerg*., 8 (1981) 229.

[34] H. Jaegfeldt, *Bioelectrochem. Bioenerg*., 8 (1981) 355.

[35] C.O. Schmakel, K.S.V. Santhanam, P.J. Elving, *J. Am. Chem. Soc*., 97 (1975) 5083.

[36] I. Ali, B. Soomro, S. Omanovic, *Electrochem. Commun*., 13 (2011) 562.

[37] M. Beley, J.-P. Collin, *J. Mol. Catal*., 79 (1993) 133.

[38] Y. Nakamura, S.I. Suye, J.I. Kira, H. Tera, I. Tabata, M. Senda, *Biochim. Biophys. Acta - General Subjects,* 1289 (1996) 221.

[39] E. Bojarska, B. Czochralska, *Bioelectrochem. Bioenerg*., 16 (1986) 287.

[40] C.O. Schmakel, M.A. Jensen, P.J. Elving, *Bioelectrochem. Bioenerg*., 5 (1978) 625.

[41] M. Aizawa, R.W. Coughlin, M. Charles, *Biotechnol. Bioeng*., 18 (1976) 209.

[42] J.N. Burnett, A.L. Underwood, *Biochemistry*, 4 (1965) 2060.

[43] A. Salimi, M. Izadi, R. Hallaj, S. Soltanian, H. Hadadzadeh, *J. Solid State Electrochem.,* 13 (2009) 485.

[44] E. Siu, K. Won, B.P. Chan, *Biotechnol. Prog.,* 23 (2007) 293.

[45] S.H. Baik, C. Kang, I.C. Jeon, S.E. Yun, *Biotechnol. Tech.,* 13 (1999) 1.

[46] Y.T. Long, H.Y. Chen, *J. Electroanal. Chem*., 440 (1997) 239.

[47] G. Rahman, J.Y. Lim, K.D. Jung, O.S. Joo, *Electrochem. Commun*., 12 (2010) 1371.

[48] C. Kohlmann, W. Maerkle, S. Luetz, *J. Mol. Catal. B: Enzym.,* 51 (2008) 57.

[49] F. Hollmann, A. Schmid, *Biocatal. Biotransform.,* 22 (2004) 63.

[50] O.M.S. Filipe, C.M.A. Brett, *Electroanal.,* 16 (2004) 994.

[51] M. Studnickova, H. Paulova-Klukanov, J. Turanek, J. Kovar, *J. Electroanal. Chem*., 252 (1988) 383.

[52] M.A. Jensen, W.T. Bresnahan, P.J. Elving, *Bioelectrochem. Bioenerg.,* 11 (1983) 299.

[53] H. Jaegfeldt, *J. Electroanal. Chem. Interfacial Electrochem.,* 128 (1981) 355.

[54] W.T. Bresnahan, P.J. Elving, *JACS.,* 103 (1981) 2379.

[55] W.T. Bresnahan, J. Moiroux, Z. Samec, P.J. Elving, *Bioelectrochem. Bioenerg.,* 7 (1980) 125.

[56] J. Moiroux, P.J. Elving, *J. Electroanal. Chem*., 102 (1979) 93.

[57] B. Qi, L. He, X. Bo, H. Yang, L. Guo, *Chem. Eng. J.,* 171 (2011) 340.

[58] Y. Shimizu, A. Kitani, S. Ito, K. Sasaki, *Denki Kagaku oyobi Kogyo Butsuri Kagaku,* 61 (1993) 872.

[59] K. Vuorilehto, S. Lutz, C. Wandrey, *Bioelectrochemistry,* 65 (2004) 1.

[60] Q. Wang, H. Tang, Q. Xie, L. Tan, Y. Zhang, B. Li, S. Yao, *Electrochim. Acta,* 52 (2007) 6630.

[61] S.A. Kumar, S.-M. Chen, *Sens. Actuators, B,* 123 (2007) 964.

[62] H.K. Song, S.H. Lee, K. Won, J.H. Park, J.K. Kim, H. Lee, S.J. Moon, D.K. Kim, C.B. Park, *Angew. Chem. Int. Edit.,* 47 (2008) 1749.

[63] K. Warriner, S. Higson, P. Vadgama, *Mater. Sci. Eng., C,* 5 (1997) 91.

[64] A.A. Karyakin, O.A. Bobrova, E.E. Karyakina, *J. Electroanal. Chem*., 399 (1995) 179.

[65] J. Canivet, G. Suss-Fink, P. Stepnicka, *Eur. J. Inorg. Chem.,* 2007 (2007) 4701.

[66] S.B. Sobolov, M.D. Leonida, A. Bartoszko-Malik, K.I. Voivodov, F. McKinney, J. Kim, A.J. Fry, *J. Org. Chem.,* 61 (1996) 2125.

[67] K.I. Voivodov, S.B. Sobolov, M. Draganoiu Leonida, A.J. Fry, *Bioorg. Med. Chem. Lett.,* 5 (1995) 681.

[68] A.J. Fry, S.B. Sobolov, M.D. Leonida, K.I. Voivodov, *Tetrahedron Lett.,* 35 (1994) 5607.

[69] I. Ali. B. Theoret, W. Brown and S. Omanovic, *manuscript in preparation*.

[70] K.C. Lin, S.M. Chen, *J. Electroanal. Chem*., 578 (2005) 213.

[71] K.C. Lin, S.M. Chen, *J. Electroanal. Chem*., 589 (2006) 52.

[72] K.C. Lin, S.M. Chen, *J. Electrochem. Soc.,* 153 (2006) D91.

[73] S.M. Chen, M.I. Liu, *Electrochim. Acta,* 51 (2006) 4744.

[74] X. Chen, J.M. Fenton, R.J. Fisher, R.A. Peattie, *J. Electrochem. Soc.,* 151 (2004) E56.

[75] S. Kim, S.E. Yun, C. Kang, *Electrochem. Commun*., 1 (1999) 151.

[76] S. Kim, S.E. Yun, C. Kang, *J. Electroanal. Chem*., 465 (1999) 153.

[77] M.T. Chang H C, Uchida., *Electrochem. Commun*., (1991) 281.

[78] K. Cheikhou, T. Tzedakis, *AIChE J.,* 54 (2008) 1365.

[79] H. Jaegfeldt, *J. Electroanal. Chem. Interfacial Electrochem.,* 110 (1980) 295.

[80] I. Ali, A. Gill, S. Omanovic, *Chem. Eng. J.,* 188 (2012) 173.

[81] S. Hrapovic, Y. Liu, K.B. Male, J.H.T. Luong, *Anal. Chem.,* 76 (2004) 1083.

[82] A. Salimi, E. Sharifi, A. Noorbakhsh, S. Soltanian, *Electrochem. Commun*., 8 (2006) 1499.

[83] C.E. Baddour, F. Fadlallah, D. Nasuhoglu, R. Mitra, L. Vandsburger, J.L. Meunier, *Carbon,* 47 (2009) 313.

[84] A.J. Bard, L.R. Faulkner, *Electrochemical Methods: Fundamentals and Applications*, Wiley, (2001).

[85] S. Sampath, O. Lev, *J. Electroanal. Chem*., 446 (1998) 57.

[86] S.B. Saidman, E.C. Bellocq, J.B. Bessone, *Electrochim. Acta*, 35 (1990) 329.

[87] S.E. Group, *Instrumental Methods in Electrochemistry,* Wiley, New York, (1985).

[88] R.S. Nicholson, I. Shain, *Anal. Chem.,* 36 (1964) 706.

[89] W.S. Kim, W.J. Sim, K.I. Chung, Y.E. Sung, Y.K. Choi, *J. Power Sources,* 112 (2002) 76.

[90] J. Wang, *Analytical Electrochemistry,* Wiley, VCH, Massachusetts (2000).

[91] P. Mericam, M. Astruc, X. Andrieu, *J. Electroanal. Chem*., 169 (1984) 207.

[92] T.E. Edmonds, *Anal. Chim. Acta,* 116 (1980) 323.

[93] Eco Chemie B.V., *General Purpose Electrochemical system,* Version 4.9.5.

[94] W.J. Lorenz, F. Mansfeld, *Corros. Sci.,* 21 (1981) 647.

[95] M.A. Amin, S.S. Abd El-Rehim, E.E.F. El-Sherbini, R.S. Bayoumi, *Electrochim. Acta,* 52 (2007) 3588.

[96] B.A. Boukamp, *Equivalent Circuit Users Manual, Report CT88/265/128,* University of Twente, Department of Chemical Technology, The Netherlands, 1989.

[97] H. Xiaoqiu, N. Duc, D.W. Greve, M.M. Domach, *IEEE, Sens. J.,* 4 (2004) 576.

[98] S. Omanovic, S.G. Roscoe, *J. Colloid Interface Sci.,* 227 (2000) 452.

[99] S. Omanovic, S.G. Roscoe, *Langmuir,* 15 (1999) 8315.

[100] K. Conway, *The Electrochemical Double Layer,* The Electrochemical Society, Inc, New Jersey, (1997).

[101] G.Prentice, *Electrochemical Engineering Principles,* Prentice Hall, Upper Saddle River, New Jersey, (1991).

[102] G.J. Brug, A.L.G. Van Den Eeden, M. Sluyters-Rehbach, J.H. Sluyters, *J. Electroanal. Chem*., 176 (1984) 275.

[103] A. Damian, S. Omanovic, *Langmuir*, 23 (2007) 3162.

[104] M. Farcas, N.P. Cosman, D.K. Ting, S.G. Roscoe, S. Omanovic, *J. Electroanal. Chem*., 649 (2010) 206.

[105] M.J. Desroches, N. Chaudhary, S. Omanovic, *Biomacromolecules,* 8 (2007) 2836.

[106] S. Ghareba, S. Omanovic, *Corros. Sci.,* 52 (2010) 2104.

[107] S. Ghareba, S. Omanovic, *Electrochim. Acta,* 56 (2011) 3890.

[108] H. Hennessey, N. Afara, S. Omanovic, A.L. Padjen, *Anal. Chim. Acta,* 643 (2009) 45.

[109] J. Hu, D. Yang, Q. Kang, D. Shen, *Sens. Actuators, B,* 96 (2003) 390.

[110] M. Iwaki, N.P.J. Cotton, P.G. Quirk, P.R. Rich, J.B. Jackson, *J. Am. Chem. Soc.,* 128 (2006) 2621.

[111] S. Bayari, A. Atac, S. Yurdakul, *J. Mol. Struct.,* 655 (2003) 163.

[112] E. Sahin, S. Ide, S. Yurdakul, *J. Mol. Struct.,* 616 (2002) 253.

[113] K.T. Yue, C.L. Martin, D. Chen, P. Nelson, D.L. Sloan, R. Callender, *Biochemistry*, 25 (1986) 4941.

[114] R. Savoie, J.J. Jutier, L. Prizant, A.L. Beauchamp, *Spectrochim. Acta A,* 38 (1982) 561.

[115] C. Nadolny, G. Zundel, *J. Mol. Struct.,* 385 (1996) 81.

[116] X. Bin, I. Zawisza, J.D. Goddard, J. Lipkowski, *Langmuir,* 21 (2005) 330.

[117] S.H. Brewer, S.J. Anthireya, S.E. Lappi, D.L. Drapcho, S. Franzen, *Langmuir,* 18 (2002) 4460.

[118] E. Benedetti, E. Bramanti, F. Papineschi, I. Rossi, E. Benedetti, *Appl. Spectrosc.,* 51 (1997) 792.

[119] H. Takeuchi, H. Murata, I. Harada, *J. Am. Chem. Soc.,* 110 (1988) 392.

[120] Y.J. Xiao, J.P. Markwell, *Langmuir,* 13 (1997) 7068.

[121] A. Atac, M. Karabacak, E. Kose, C. Karaca, *Spectrochim. Acta A,* 83 (2011) 250.

[122] P.Atkins, *Elements of Physical Chemistry,* W. H. Freeman, New York, (2009).

[123] V. Massey, Q.H. Gibson, C. Veeger, *Biochem. J.,* 77 (1960) 341.

[124] S. Yasuda, T. Hiraoka, D.N. Futaba, T. Yamada, M. Yumura, K. Hata, *Nano Lett.,* 9 (2009) 769.

[125] S. Trasatti, *J. Electroanal. Chem.,* 39 (1972) 163.

[126] E. Navarro-Flores, Z. Chong, S. Omanovic, *J. Mol. Catal. A: Chem.,* 226 (2005) 179.

[127] J. Cantet, A. Bergel, M. Comtat, *Bioelectrochem. Bioenerg.,* 27 (1992) 475.

[128] G. Rahman, J.Y. Lim, K.D. Jung, O.S. Joo, *Int. J. Electrochem. Sci.,* 6 (2011) 2789.

[129] T.S. Mkwizu, M.K. Mathe, I. Cukrowski, *ECS Trans*, 19 (2009) 97.

[130] S. Szabo, I. Bakos, *J. Electroanal. Chem.,* 230 (1987) 233.

[131] J.B. Raoof, R. Ojani, S.A. Esfeden, S.R. Nadimi, *Int. J. Hydrogen Energy,* 35 (2010) 3937.

[132] W. Zhu, G. Wang, X. Hong, X. Shen, D. Li, X. Xie, *Electrochim. Acta,* 55 (2009) 480.

[133] A. Mohammadi, A. Bayandori Moghaddam, M. Kazemzad, R. Dinarvand, J. Badraghi, *Mater. Sci. Eng., C,* 29 (2009) 1752.

[134] N.F. Heinig, N. Kharbanda, M.R. Pynenburg, X.J. Zhou, G.A. Schultz, K.T. Leung, *Mater. Lett.,* 62 (2008) 2285.

[135] A. Bayandori Moghaddam, M.R. Ganjali, A.A. Saboury, A.A. Moosavi-Movahedi, P. Norouzi, *J. Appl. Electrochem.,* 38 (2008) 1233.

APPENDICES

Appendix A

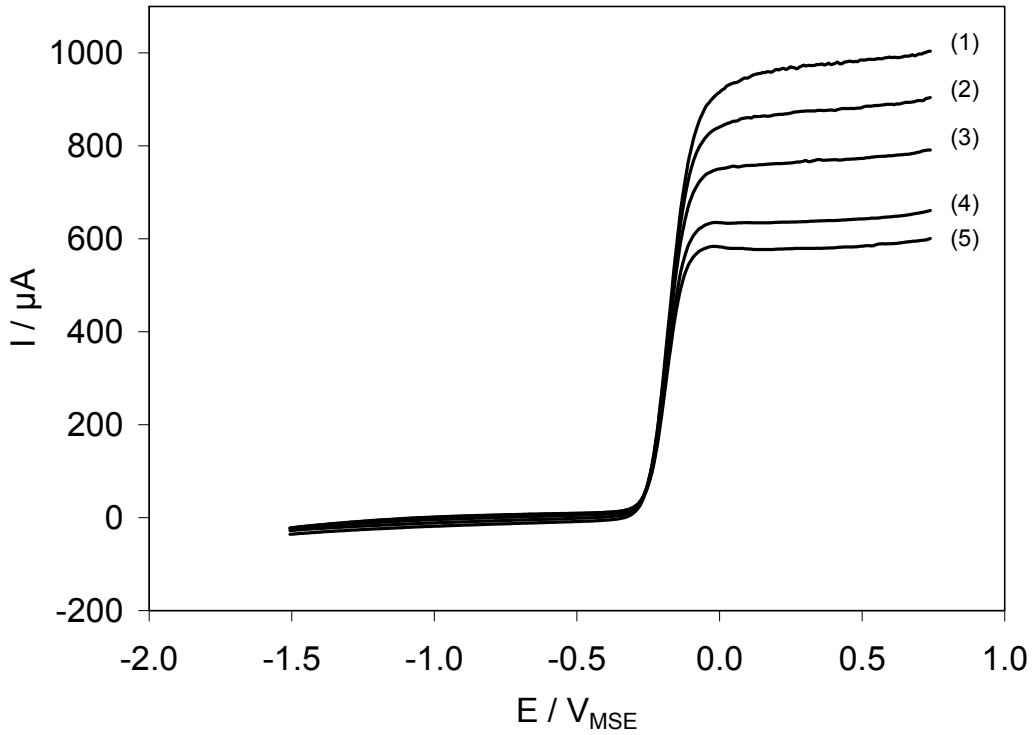

Fig. A. 1: Rotating GC-disc-electrode linear polarization voltammograms recorded in 20 mM $K_4Fe(CN)_6.3H_2O$ and 0.2 M KCl. Rotation velocities: (1) 100, (2) 120, (3) 160, (4) 240 and (5) 300 rpm. Scan rate, *sr* = 10 mV s^{-1}.

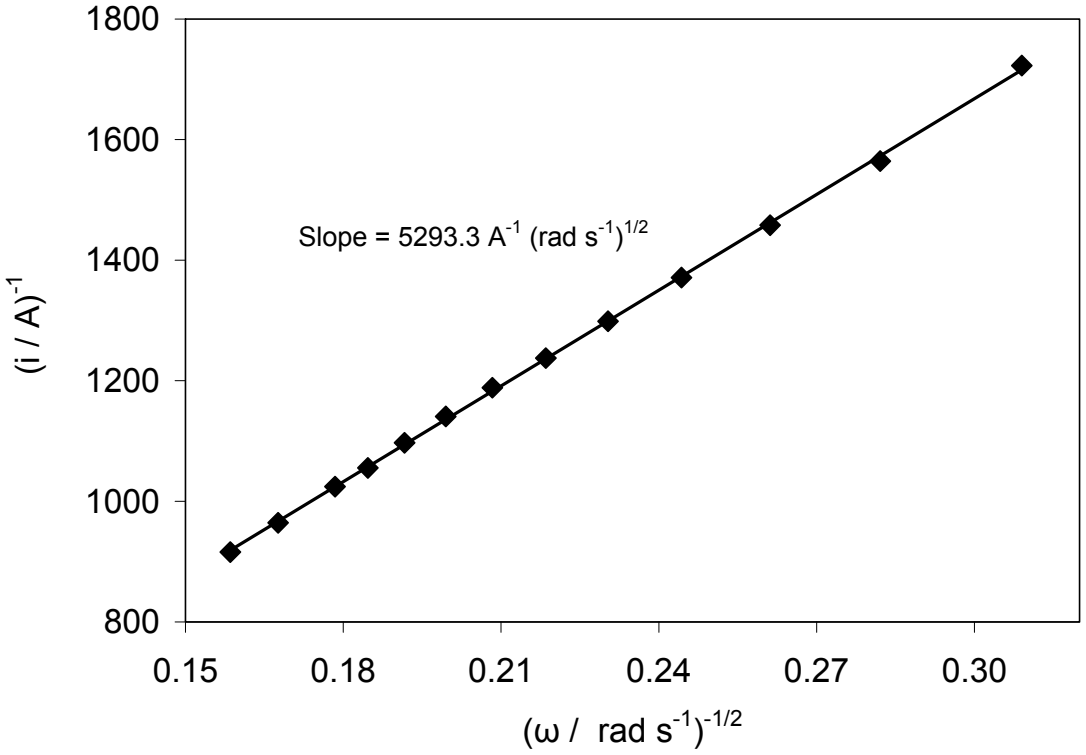

Fig. A. 2: Koutecky–Levich plot of $K_4Fe(CN)_6.3H_2O$ on a GC electrode surface obtained from the Fig. A. 1.

$$\frac{1}{I} = \frac{1}{I_e} + \frac{1}{I_d} = \frac{-1}{nAFkc} - \frac{1}{0.62nAFD^{2/3}\upsilon^{-1/6}[K_4Fe(CN)_6.3H_20]\omega^{1/2}} \qquad (A.1)$$

where $n = 1$ is the number of electrons participating in the redox reaction, $F = 96{,}485$ C mol^{-1} is Faraday constant, A is the area of the electrode (cm^2), $D = 6.70 \pm 0.02 \times 10^{-6}$ cm^2 s^{-1} is the diffusion coefficient of the molecule in solution, $[K_4Fe(CN)_6.3H_2O] = 2 \times 10^{-5}$ mol cm^{-3} is the concentration of the molecule in the bulk solution, and $v = 0.01$ cm^2 s^{-1} is the kinematic viscosity of the solution and ω is the rotation rate of electrode (rad s^{-1}).

Using the slop in Fig. A. 1 and Eq. A.1:

***A* = 0.206 cm^2**

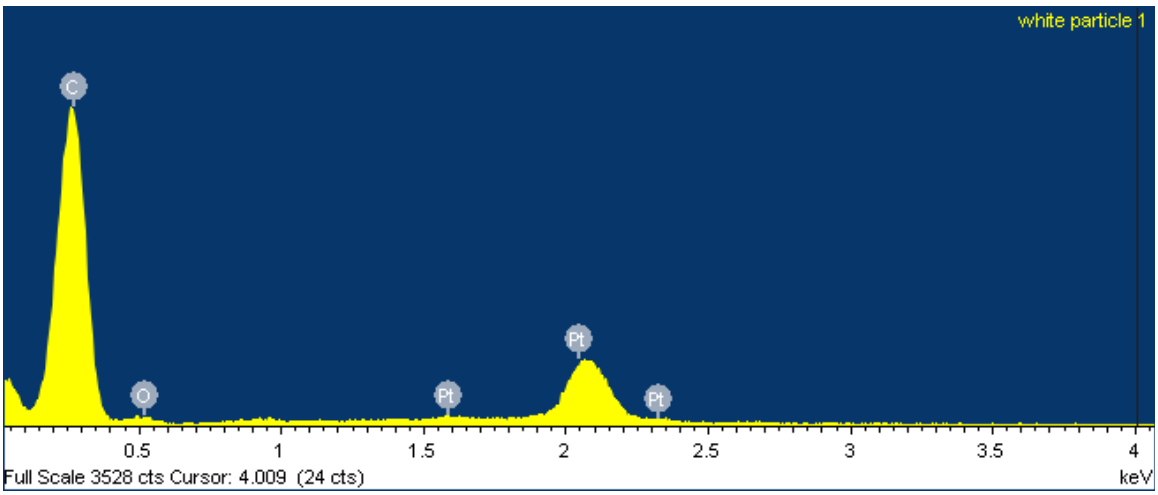

Fig. A. 3: EDX spectrum of Pt nano-island deposited on GC electrode surface.

Appendix B

Cyclic voltammetry: irreversible electrode process

Reaction Equation: $R \xrightarrow{ne^-, k_s} P$

Fitable parameters:

Log(Normalized electron trabsfer rate at E^0=0), $\log\left(\bar{k}_{fb}^{0}\right)$

(exchanged electrons)*(transfer coefficient) αn

normalized current I_{norm}($I = I_{\text{norm}*}\,\chi(bt)$)($A$)

constant background current (A)

Initial guesses available for: $E^0, \alpha n$, I_{norm}, background current

Comments: The parameter $\log\left(\bar{k}_{fb}^{0}\right)$ is a 10-base logarithm of the electron transfer rate, normalized with respect to the time scale of the experiment $\bar{k}_{fb}^{0} = k_{fb}^{0}\sqrt{RT/nFVD}$, where V is the scan rate and k_{fh}^{0} is the electron transfer rate at E=0, used in reduced Butler-Volmer equation

$$I = k_{fb}^{0} c_R \exp\left(\left(-\alpha nF/RT\right)E\right) = k_s c_R \exp\left(\left(-\alpha nF/RT\right)\left(E - E^0\right)\right)$$

According to the theory, the peak current is equal to $nFAc_{bulk}\left(\pi bD\right)^{1/2} * \chi(bt)$, where the first term is equal to the fitable parameter I_{norm} and the function $\chi(bt)$, $b = \alpha nFV/RT$, represents the shape of the voltammetric peak. The peak value of this function is equal to 0.4958 for linear sweep voltammetry, and for staircase voltammetry it depends on the electron transfer rate k_s , the transfer coefficient α , the step height, step time and the current sampling parameter α . The function $\chi(bt)$ is defined as:

$$\chi(bt) = \frac{1}{\sqrt{\pi}} \sum_{j=1}^{\infty} (-1)^{j+1} \frac{\left(\sqrt{\pi}\right)^j}{\sqrt{(j-1)!}} \times \exp\left[\left(-\frac{j\alpha n_a F}{RT}\right)\left(E - E^0 + \frac{RT}{\alpha n_a F}\ln\frac{\sqrt{\pi D_{ob}}}{k_s}\right)\right]$$

There is no need to set the number of exchanged electrons, because the term αn is fitted as a whole.

Differential pulse voltammetry: irreversible electrode process

Reaction Equation: $R \xrightarrow{ne^-, k_s} P$

Fitable parameters:

Characteristic potential E^* (V)

Log(Normalized electron transfer rate at E^0=0), $\log\left(\bar{k}^0_{fb}\right)$

(exchanged electrons)*(transfer coefficient) αn

Peak current I_p (A)

constant background current (A)

Initial guesses available for: number of exchanged electrons, E_p, $\log\left(\bar{k}^0_{fb}\right), \alpha n$, I_p , background current

Comments:

There is no need to set the number of exchanged electrons, because the term αn is fitted as a whole.

The characteristic potential E^* is defined as

$E^* = \left(RT / \alpha nF\right) \ln \bar{k}^0_{fb} = E^0 + \left(RT / \alpha nF\right) \ln \bar{k}_s$, where $\bar{k}^0_{fb} = k^0_{fb} \sqrt{t_m / D_R}$ and $\bar{k}_s = k_s \sqrt{t_m / D_R} . k_s$ and $k^0{}_{fh}$ are the electron transfer rates used in Butler-Volmer equation

$I = k^0_{fb} c_R \exp\left(\left(-\alpha nF / RT\right)E\right) = k_s c_R \exp\left(\left(-\alpha nF / RT\right)\left(E - E^0\right)\right)$

Appendix C

Table C.1: EEC parameters obtained by fitting the EIS experimental spectra recorded at different potentials in 0.1 M $NaClO_4$ + 4 mM, pH 5.8 using the EEC model presented in Fig. 5.10.

E_{appl} (V)	-1.0	-1.3	-1.4	-1.45	-1.5	-1.525	-1.55	-1.575	-1.6
$CPE_1 \times 10^5$ (Ω^{-1} cm^{-2} s^n)	7.87	8.54	8.68	8.70	9.81	9.96	10.46	10.54	10.77
± SD	0.99	0.29	0.44	0.65	1.11	0.90	1.20	0.71	0.53
n_1	0.88	0.88	0.88	0.88	0.86	0.87	0.91	0.88	0.87
± SD	0.01	0.01	0.01	0.01	0.01	0.01	0.02	0.01	0.01
R_1 (kΩ cm^2)	0.91	0.56	0.35	0.32	0.48	0.36	0.12	0.11	0.11
± SD	0.14	0.19	0.08	0.11	0.03	0.04	0.02	0	0
$CPE_2 \times 10^5$ (Ω^{-1} cm^{-2} s^n)	11.56	19.53	28.62	43.79	149.60	82.43	48.62	33.84	27.71
± SD	1.07	2.24	1.72	16.19	11.81	2.96	0.76	0.72	1.78
n_2	0.51	0.42	0.37	0.47	0.41	0.40	0.39	0.34	0.30
± SD	0.01	0.02	0.03	0.08	0.01	0.01	0.02	0.02	0.01
R_2 (kΩ cm^2)	17.45	19.61	2.42	0.60	-	-	-	-	-
± SD	2.84	5.27	0.13	0.15	-	-	-	-	-
R_i (kΩ cm^2)	18.36	20.17	2.77	0.92	0.48	0.36	0.12	0.11	0.11
± SD	3.06	5.46	0.08	0.13	0.03	0.042	0.02	0	0

Table C.2: EEC parameters obtained by fitting the EIS experimental spectra recorded at –1.5 V_{MSE} and various NAD^+ concentrations in $NaClO_4$ pH 5.8 using the EEC model presented in Fig. 5.10.

c_i (mM)	0	0.5	1	1.5	2	2.5	3	3.5	4	4.5	5
$CPE_1 \times 10^3$ (Ω^{-1} cm^{-2} s^n)	16.12	4.64	2.81	2.26	1.55	1.54	1.47	1.35	1.28	1.19	1.23
± SD	0.20	0.45	0.15	0.74	0.35	0.34	0.36	0.40	0.42	0.43	0.38
n_1	0.76	0.81	0.81	0.81	.84	0.83	0.82	0.83	0.83	0.83	0.82
± SD	0.12	0.06	0.01	0	0.01	0	0.01	0	0.01	0.01	0.01
R_1 (kΩ cm^2)	0.07	0.16	0.30	0.40	0.44	0.55	0.65	0.73	0.80	0.83	0.92
± SD	0.03	0.06	0.16	0.19	0.19	0.20	0.28	0.26	0.21	0.21	0.25
$CPE_2 \times 10^3$ (Ω^{-1} cm^{-2} s^n)	3.59	4.25	4.25	4.07	4.64	4.6	4.89	5.36	6.08	6.22	6.42
± SD	1.21	0.68	0.52	0.25	0.25	0.32	0.19	0.27	0.51	0.71	0.82
n_2	0.58	0.56	0.56	0.57	0.56	0.56	0.57	0.56	0.56	0.56	0.56
± SD	0.04	0.02	0.01	0	0	0.01	0	0.01	0	0	0.01
R_2 (kΩ cm^2)	14.04	13.75	12.16	11.51	11.17	10.09	8.88	8.40	7.54	6.95	6.39
± SD	1.14	3.22	3.87	3.20	3.64	2.87	2.82	2.36	1.94	1.24	0.82
R_i (kΩ cm^2)	14.11	13.91	12.46	11.91	11.60	10.64	9.53	9.13	8.34	7.78	7.31
± SD	1.14	3.16	3.73	3.01	3.45	2.69	2.53	2.10	1.72	1.04	0.58